Road Surface Measurement and Multi-scale Modeling of Rubber-Road Contact and Adhesion

Mohammad “Mehran” Motamedi

Dissertation submitted to the faculty of the Virginia Polytechnic Institute and State University in partial fulfillment of the requirements for the degree of

Doctor of Philosophy

in

Mechanical Engineering

Saied Taheri, Co-Chair

Corina Sandu, Co-Chair

Mehdi Ahmadian

Hans R. Dorfi

Robert L. West

August 26, 2015

Blacksburg, VA

Keywords: Tire-Road Friction, Hysteresis Friction, Adhesion, Profile Measurement, Friction Testing

Road Surface Measurement and Multi-scale Modeling of Rubber-Road Contact and Adhesion

Mohammad “Mehran” Motamedi

Abstract

A major challenge in tire, as well as in road engineering, is to understand the intricate mechanisms of friction. Pavement texture is a feature of the road surface that determines most tire-road interactions, and can be grouped into two classes: macro-texture, resulting mainly in the hysteretic component of friction, and micro-texture, resulting in adhesion. If both textures are maintained at high levels, they can help provide sufficient resistance to skidding.

The ultimate objective of this research is to develop a physics-based multiscale rubber-road friction model that can predict the effectiveness of the tire as it interacts with the vehicle and the pavement. The model is developed based on sound physics and contact mechanics theories and uses road profile measurements and data measured on various tire compounds.

To be able to predict road surface characteristics, it is proven that road surfaces are of fractal nature on given ranges of scale. It is shown that while global fractal quantities fail to classify pavement profiles, a local fractal parameter and three other texture parameters can separate road profiles that have different friction characteristics.

Through the implementation of various contact theories and by conducting simulation studies, a methodical understanding of contact mechanics and of the effect of the diverse factors that influence friction is attained. To predict the viscoelastic friction between any given tire tread compound and road, the Nanovea JR25 portable optical profilometer is used to measure the road profiles. To characterize the road profile, the one-dimensional pavement measurements are used to obtain the two-dimensional power spectrum, followed by testing and characterizing the tread compounds (this is being carried out by Bridgestone). This data is used to develop a comprehensive analytical methodology to predict friction. To validate this model, a Dynamic Friction Test apparatus is designed and built. The friction tester enables measurement of the friction between tread compound samples and arbitrary surfaces, at different slip ratios. The correlations between the simulations and both indoor and outdoor experimental results are investigated.

Acknowledgements

Foremost, I would like to express my sincere gratitude to my advisors Dr. Saied Taheri and Dr. Corina Sandu for the continuous support of my PhD study and research, for their patience, motivation, enthusiasm, and immense knowledge. Their supervision helped me in all the time of research and writing of this document.

Besides my advisors, I would like to thank the rest of my thesis committee: Dr. Mehdi Ahmadian, Dr. Hans Dorfi and Dr. Robert West, for their encouragement and insightful comments.

A very special thanks goes out to Cooper Tire and Rubber Company, and Bridgestone Americas, for offering me the internship opportunities, and chances to work on diverse and exciting projects related to this research, as well as allowing me to use a great deal of that work for my PhD thesis. I must acknowledge Dr. Patrick Majors, my manager at Cooper Tire for his priceless guidance, and Mr. Tony Beal for the useful discussions on spectral analysis of road profiles. Appreciation also goes out to Dr. Hans Dorfi and Mr. Brian Steenwyk, my manager and team leader, respectively, and Dr. Anurag Warhadpande, my colleague and mentor at Bridgestone, all of whom taught me valuable knowledge and new skills.

I thank my fellow lab-mates at CenTiRe; Chuang Su, Karan Khanse, Eric Pierce and Hongxiao Yu for their great ideas and their time in assisting me with the design and building of the Dynamic Friction Tester. I would like to especially thank Michael Craft from Center for Vehicle Systems and Safety (CVeSS) for taking time out of his busy schedule to guide us in designing the friction tester.

I would also like to thank my family for the kind support they provided me through my entire life.

In conclusion, I recognize that this research would not have been possible without the financial support of the NSF I/UCRC Center for Tire Research (CenTiRe) and the National Science Foundation (NSF) through grant #1432896 and the technical and intellectual support of the mentors of this project.

Contents

List of Figures

List of Tables

Nomenclature	
ΔE	energy dissipated during the time period t_0 $[\frac{kJ}{sec}]$
A_0	surface area $[m^2]$
σ_f	shear stress $[MPa]$
v	sliding velocity $[\frac{m}{s}]$
q	wavevector $[\frac{1}{m}]$
λ	horizontal length scale $[m]$
ζ	Magnification
λ_0	roll-off wavelength $[m]$
θ	angular parameter of the Indenters method $[deg]$
Z_s	height of the S_{th} summit $[m]$
X_s	abscissa of the S_{th} summit $[m]$
Z_e	height of the e_{th} extremum $[m]$
X_e	abscissa of the e_{th} extremum $[m]$
α	half angle at the top (Indenters method) $[deg]$
f_v	vertical force $[N]$

f_h	horizontal force $[N]$
μ	coefficient of friction
E	modulus of the rubber $[MPa]$
τ	relaxation time of the rubber $[sec]$
z_i	interpolated value for sample i in a profile $[m]$
b_1	slope of the surface profile
b_0	offset of the surface profile $[m]$
Z_i	the corrected sample signal value $[m]$
$w_{i,H}$	Hanning window
$w_{i,C}$	split cosine bell window
Z_k	Discrete Fourier Transform of the windowed profile
Δf_{sp}	Bandwidth $[1/m]$
l	evaluation length $[m]$
$Z_{PSD,k}$	power spectral density $[m^3]$
$C(q)$	surface roughness power spectrum $[m^4]$
$h(x)$	substrate height measured from the average plane $[m]$

$\langle \dots \rangle$	ensemble average
h_0	rms roughness amplitude $[m]$
a	lattice constant
L	linear size of the surface $[m]$
H	Hurst exponent
D_f	fractal dimension
H_m	two dimensional DFT of h_n $[m^4]$
A	surface area under study $[m^2]$
$C(m)$	angular average power spectrum $[m^4]$
$\tilde{\sigma}$	the root mean square fluctuations around the mean height (the variance) $[m]$
$\xi_\perp$	correlation length normal to the surface $[m]$
$\xi_{\|\|}$	largest horizontal asperity dimension $[m]$
$C_z(\lambda)$	height difference correlation function $[m^2]$
$\Gamma_z(\lambda)$	height correlation function $[m^2]$
$S(f)$	spectral power density $[m^3/sec]$
f	spatial frequency $[\frac{1}{m}]$

λ_2	transition wavelength $[m]$
C_{2D}	2D power spectrum $[m^4]$
C_{1D}	1D power spectrum $[m^3]$
β^2	mean square roughness $[m^2]$
f_c	Nyquist frequency $[\frac{1}{m}]$
σ	mean perpendicular pressure $[MPa]$
ν	Poisson ratio
G	shear modulus $[MPa]$
q_0	roll-off wavevector $\left[\frac{1}{m}\right]$
q_1	short-distance cut-off wavevector $[\frac{1}{m}]$
T	temperature [℃]
T_q	flash temperature [℃]
T_0	reference temperature [℃]
a_T	horizontal shift factor
σ_0	nominal contact stress $[MPa]$
$\langle\delta\rangle$	excited layer thickness $[m]$

$\langle z_p \rangle$	mean penetration depth of rubber $[m]$
$S(\omega)$	power spectral density $[m^3/sec]$
F_{n}	Greenwood-Williamson functions
$\langle z \rangle$	mean profile height $[m]$
$\phi(z)$	profile distribution function
n_s	summit density
A_c	real area of contact $[m^2]$
λ_{min}	minimum relevant length scale $[m]$
μ_{Adh}	contribution to friction force arising from interfacial processes
τ_S	true interfacial shear strength $[MPa]$
μ_{Hyst}	hysteresis component of friction
$S_{xx}(f)$	auto power spectrum of the profile $[m^3/sec]$
$X(f)$	Fourier transform of the signal
FN	friction number
E_a	energy at scale a
β	correlation exponent

$C(l)$	autocorrelation of the signal $[m^2]$
$DimR$	regularization dimension
α	Holder exponent
$f(\alpha)$	Holder function

1 Introduction

1.1 Motivation

An important problem in road transportation is to understand the mechanisms of friction between the rubber and the road. Although this is an old problem, there has not been too much research leading to suitable models for defining this phenomenon. This is due to the fact that modeling tire-road contact and adhesion depends on many parameters: type of rubber, type of road, speed, temperature, etc.

Unless tire-road friction is accurately described, no tire model will provide an accurate representation of tire dynamics. The main objective of this research is to generate programs and algorithms that process the data and generate the necessary information required for physics-based friction estimation. The deliverables of the modeling effort will be a thorough understanding of contact mechanics, the effect of the different factors that influence friction, and eventually the ability to accurately predict the friction between any compound and any road. This helps tire engineers design tires that offer crucial benefits to the consumers, such as enhanced traction and longer tread wear life. The most essential difficulties that one faces in this endeavor are applying the appropriate conditions for the viscoelastic testing of rubber, as well as analytically determining the effect of certain parameters on friction.

The lack of a suitable physics-based friction model that can be used for tire design, performance prediction as well as vehicle dynamic simulation has motivated this research. The empirical models, where a set of data is fitted with fully empirical equations, are the widely used methodology. However, an empirical/semi-empirical model is a short term solution that works only for the investigated data set. Moreover, the fitting has to be adopted again as soon as one test condition changes. Therefore, a thorough, physics-based friction model could be a tool that can facilitate more robust predictions. In the present work, first, an in-depth inspection and implementation of the existing physics-based models is

carried out. That builds the understanding and the basis for the development of a more inclusive and proficient friction prediction method, which is the ultimate mission of the current research.

To estimate friction between rubber and a rough surface using a physics-based model, the following steps are carried out:

- The road surface profiles, as well as the texture of different sandpaper grits, are measured via the Nanovea optical profilometer.
- The measured profiles are then characterized and parameterized, where the 2D Power Spectral Density is calculated using only 1D line-scans (more on this in the Methodology Chapter).
- Dynamic Mechanical Analysis tests are carried out (at Bridgestone), and the rubber compounds are characterized to generate viscoelastic master curves.
- A detailed study of rubber-road contact mechanics, using the existing theories, is done, including:
    - Contribution from different length scales of surface roughness
    - Estimation of real area of contact between rubber and substrate
    - Effect of sliding velocity
    - Effect of flash heating in the contact patch
    - Contact pressure dependency of friction
    - Friction estimation using present approaches, such as Persson, Klüppel, and Rado.

1.2 Research Contributions

The key contribution of the current research is the development of a multiscale friction model, through an exhaustive examination of the major factors that affect rubber-road friction. The model is more comprehensive and proficient than any single existing physics-based model. This is done by identifying

the strengths of each model and its advantages over the competitors, and incorporating those into a new consolidated model while additional factors are considered.

The real contact area for tire tread compounds, and the effect of using low strain and large strain viscoelastic master curves are meticulously studied. The outcome leads to better vision for researchers, when designing dynamic mechanical analysis tests, and when predicting friction and wear using either physics-based or finite-element methods.

Sensitivity of friction to surface parameters, contributions of different length scales to friction, the mean penetration depth and the thickness of the excited layer of rubber, and the effect of the short-distance cut-off wavevector are fully inspected. The learning from these efforts can equip researchers with an improved insight when designing tribometers, deciding on a profile measurement device and adjusting the parameters, scheming friction and wear prediction experiments, as well as friction and wear estimation algorithms, and designing tread compounds.

The surface profilometers that have been employed in most of the works reported in the literature up to the present time, either tactile or laser/laser, have at least one of the following shortcomings: the inability to measure sharp angles, failure to capture the profile of reflective surfaces, short vertical measurement range, incapability of apprehension of long enough profiles and therefore the realization of the largest wavelength of a rough surface, and outputting scores of invalid points. With the Nanovea JR25 optical profilometer that is recently purchased by CenTiRe, none of the aforementioned inadequacies is a concern. That results in more accurate profile characterization and friction prediction.

The other important contribution is designing and building a Dynamic Rubber Friction Tester (DRFT) that measures the coefficient of friction between tire tread compound samples and arbitrary surfaces. What makes this test rig unique is the capability of producing a friction coefficient vs. longitudinal slip ratio graph, which is of great interest for applications such as ABS braking, where it is desired to maintain the slip ratio around the point where friction reaches its peak value. To the best of our knowledge, no

other commercially available friction tester offers this capability. The other remarkable feature of the DRFT is that arbitrary surfaces, e.g. asphalt, concrete, sandpaper, etc., can be embedded onto the disk that simulates a road surface. The closest off-the-shelf friction tester is the LAT 100 from the VMI Group. That equipment is structurally similar to our test rig. However, LAT 100 can only measure friction with respect to slip angle, which is not as beneficial as 'friction vs. slip ratio', when one is dealing with tread compound samples, and not full tires. Furthermore, with LAT 100, one can only use a limited number of road surface disks that are provided. Last but not least, for the development of our friction tester, less than one-tenth of what a LAT 100 costs was spent. The friction prediction model is validated using the friction measurement data from the Dynamic Friction Tester.

In summary, the contributions of this research are:

- Development of a comprehensive multiscale friction model.
- Better vision for researchers, when designing dynamic mechanical analysis tests, and when predicting friction and wear using either physics-based or finite-element methods.
- Improved insight when designing tribometers, deciding on a profile measurement device and adjusting the parameters, scheming friction and wear prediction experiments, as well as friction and wear estimation algorithms, and designing tread compounds.
- The Dynamic Rubber Friction Tester that can produce friction coefficient vs. longitudinal slip measurements for tire tread samples against arbitrary rough surfaces.

1.3 Document Outline

The rest of this document is organized as follows:

Chapter 2: Literature Review

This chapter summarizes the works related to this research that has been done by other researches thus far. First, the features of pavement texture are discussed, followed by the techniques used to measure, characterize and classify road surfaces. Next, a brief introduction to the thermo-mechanical properties of tire tread compounds is presented. Finally, the existing rubber-road friction measurement, as well as friction prediction methods are investigated.

Chapter 3: Methodology

In this chapter, first, the approaches for measuring roughness profiles are discussed. In what follows, three profile parametrization techniques that are used in this research are reviewed, namely, Persson, Klüppel, and Rado. In addition, the fractal and texture parameters that are used in this work to classify road surfaces with different friction coefficients are studied. Next, the viscoelastic master curves of tire tread compounds, and the shifting techniques that are utilized for friction estimation at different sliding velocities are described. Then, the existing algorithms for modeling rubber-rough substrate contact and friction prediction are listed and detailed. Next, the constituents of the inclusive model are presented. Lastly, friction measurements via the Dynamic Friction Tester are explained.

Chapter 4: Results

This chapter discusses the results of the simulation studies that have been completed. First, the profile characterization results using constant percentage bandwidth, as well as height difference correlation function, and power spectral density are presented. Next, the results of the algorithms developed for classification of road surfaces by employing texture parameters, the angular parameter of the Indenters method, and global and local fractal parameters are summarized. In what follows, the results of using

Persson's theory for estimation of friction coefficient, real contact area, sensitivity of friction to surface parameters, contribution of different length scales to friction, and mean penetration depth are presented. Additionally, the hysteresis friction prediction results when the effect of flash heating is included are reported. Finally, the reproduction of Klüppel's friction estimation simulations, when using one and two scaling regimes with constant and varying minimum wavelength, are presented.

Chapter 5: Summary and Discussion

This chapter briefly summarizes the procedures, the progress, and the achievements of the research.

Chapter 6: Future Work

The potential future work after the conclusion of this project are listed and detailed. Physics-based modeling of tire wear is a new project that has been approved by CenTiRe as the continuation of this research, where the procedures developed here are going to be used.

2 Literature Review

In this chapter, the existing literature on the following topics is reviewed and discussed:

- Road surfaces and their textural features.
- The methods used to measure, characterize and classify pavements.
- Thermo-mechanical properties of tire tread compounds.
- The existing rubber-road friction measurement equipment.
- The current friction prediction methods.

2.1 Road Surfaces

Pavement texture is a feature of the road surface that determines most tire-road interactions and significantly contributes to tire-pavement friction. In terms of the deviations of the pavement surface with characteristic dimensions of wavelength and amplitude, pavement textures can be grouped into two classes of micro-texture (wavelengths of $1\ \mu m$ to $0.5\ mm$) and macro-texture (wavelengths of $0.5\ mm$ to $50\ mm$). Several researches have shown that road profiles are fractal on given ranges of scale [1] [2] [3]. Such a property has obvious consequences on friction [1] [4], i.e., in the presence of fractal roads, all scales of irregularity could contribute to friction. Those contributions are however not necessarily equivalent, and some length scales might be more effective than others [5].

Friction has two important components:

1. Adhesion, which is based on micro-texture, and is the tendency of dissimilar particles and surfaces to cling to one another. Chemical adhesion (intermolecular forces), mechanical adhesion (interlocking), and dispersive adhesion (van der Waals) are the main mechanisms that explain why one material sticks to another.

2. Hysteresis, that is based on macro-texture, and is primarily based on macro-texture and is the result of energy losses generated during local fluctuations of the polymer chains (inertial friction of rubber), since the energy of deformation (induced by surface asperities) is greater than the energy of recovery.

If both textures are maintained at high levels, they can provide sufficient resistance to skidding. This is due to the fact that at low slip speeds, the effect of microtexture dominates the friction measurement, while at high slip speeds, the effect of macrotexture becomes important. Therefore, both textures are important for providing sufficient resistance to skidding. As a result, it is of pronounced importance to have a contact model that can determine friction at different texture scales. The ultimate objective of the present work is to develop a multi-scale rubber-road friction model that can describe and predict pavement surface characteristics and the effectiveness of the tire as it interacts with the vehicle and the pavement, from road profile measurement and tread compound characterization. This will contribute to the science of friction in general and will allow tire designers to design tread compounds that will result in safer road transportation systems by predicting the pavement surface characteristics (e.g., fuel efficiency, traction, and friction) as they relate to the tire interaction in terms of the pavement surface features (e.g., texture, roughness, banking, elevation change). It will also provide the ability to determine the most important tire-road interactions and functional performances including dry and wet friction, noise, splash and spray, rolling resistance and wear.

2.2 Friction between the Rubber and the Road

Since friction is usually an interfacial property, often determined by the last few uncontrolled monolayers of atoms or molecules at the interface, first-principles calculations of frictional forces for realistic systems are generally impossible. An extreme illustration of this is offered by diamond, as the friction between two clean diamond surfaces in ultrahigh vacuum is huge because of the strong interaction between the

surface dangling bonds. However, when the dangling bonds are saturated by a hydrogen monolayer (as they generally are in real life conditions), friction becomes extremely low [6]. Since most surfaces of practical use are covered by several monolayers of contaminant molecules of unknown composition, a quantitative prediction of sliding friction coefficients is out of the question. An exception to this may be rubber friction on rough surfaces, which is the subject that we address here.

Rubber friction on smooth substrates, e.g., on smooth glass surfaces, has two contributions, namely an adhesive (surface) and a hysteretic (bulk) contribution [7] [8]. The adhesive contribution results from the attractive binding forces between the rubber surface and the substrate. Surface forces are often dominated by weak attractive van der Waals interactions. For very smooth substrates, because of the low elastic moduli of rubber-like materials, even when the applied squeezing force is very gentle, this weak attraction may result in a nearly complete contact at the interface [9] [10], leading to a large sliding friction force [40]. For rough surfaces, on the other hand, the adhesive contribution to rubber friction will be much smaller because of the small contact area. The actual contact area between a tire and the road surface, for example, is typically only∼1% of the nominal footprint contact area [11] [12] [4]. Under these conditions, the bulk (hysteretic) friction mechanism is believed to prevail [11] [4]. For example, the sensitivity of tire-road friction to temperature just reflects the strong temperature dependence of the viscoelastic bulk properties of rubber. In this research, the dependency of rubber friction on the surface roughness power spectra, the influence of wear-induced polishing and of water on the road track on rubber friction are discussed.

2.2.1 Wet friction

For rubber friction on wet rough substrates at low sliding velocities, it is known that the friction typically drops by as much as 20–30% relative to the corresponding dry case [13]. Owing to the small contact area, this cannot be the result of a water-induced change of adhesion. On the other hand, the friction decrease

cannot be blamed on a purely hydrodynamic effect either. That leaves the possibility that water might change the bulk, hysteretic friction. It was recently proposed that water pools that are formed under the tire in the wet rough substrate are sealed off by the rubber, as sketched in Figure 2-1, which effectively smoothens the substrate surface [14]. Smoothing reduces the viscoelastic deformation from the surface asperities, and thus reduces rubber friction.

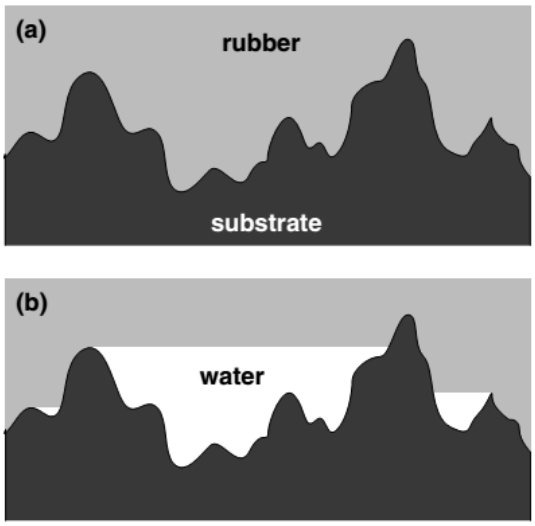

Figure 2-1. A rubber block sliding on a rough hard substrate. (a) On a dry substrate the rubber penetrates a large valley and explores the short wavelength roughness within. The pulsating rubber deformations induced by the short wavelength roughness contribute to the friction force. (b) On a wet substrate the valley turns into a water pool. Sealing of the pool now prevents the rubber from entering the valley. By removing the valley contribution to the frictional force, this sealing effect of rubber reduces the overall sliding friction; *Reproduced from [14] with permission from Nature Publishing Group.*

Another method for estimating wet friction is modeling the connection of road surface microtexture with water depth and friction [15]. This is a 2D approach, where thin water films ($< 1\ mm$) are represented by a horizontal line. The run-off that happens in the experiments is not accounted for in the theory.

Therefore, the experiments are not in good agreement with the theoretical results. This is due to the fact that water film supports the normal load, but the model neglects the shear stress of the water film. The curves of the coefficient of friction with respect to water depth are treated as Stribeck curves with three lubrication regimes. The adhesion and the hydrodynamic friction components are determined by fitting the simulation results with experiments.

2.3 Fractal Theory

A fractal is a natural phenomenon or a mathematical set that exhibits a repeating pattern that displays at every scale. If the replication is exactly the same at every scale, it is called a self-similar pattern. Fractals are different from other geometric figures because of the way in which they scale. Doubling the edge lengths of a polygon multiplies its area by four, which is two (the ratio of the new to the old side length) raised to the power of two (the dimension of the space the polygon resides in). Likewise, if the radius of a sphere is doubled, its volume scales by eight, which is two (the ratio of the new to the old radius) to the power of three (the dimension that the sphere resides in). But if a fractal's one-dimensional lengths are all doubled, the spatial content of the fractal scales by a power that is not necessarily an integer [16]. This power is called the fractal dimension of the fractal, and it usually exceeds the fractal's topological dimension [17].

A fractal dimension is a ratio providing a statistical index of complexity comparing how the details in a pattern (strictly speaking, a fractal pattern) change with the scale at which they are measured. It has also been characterized as a measure of the space-filling capacity of a pattern that tells how a fractal scales differently from the space it is embedded in; a fractal dimension does not have to be an integer [18] [19] [20].

The essential idea of "fractured" dimensions has a long history in mathematics, but the term itself was brought to the fore by Benoit Mandelbrot based in his 1967 paper on self-similarity, in which he discussed fractional dimensions [21]. In that paper, Mandelbrot cited previous work by Lewis Fry Richardson describing the counter-intuitive notion that a coastline's measured length changes with the length of the measuring stick used (see Figure 2-2). In terms of that notion, the fractal dimension of a coastline quantifies how the number of scaled measuring sticks required for measuring the coastline changes with the scale applied to the stick. There are several formal mathematical definitions of fractal dimension that build on this basic concept of change in detail with change in scale.

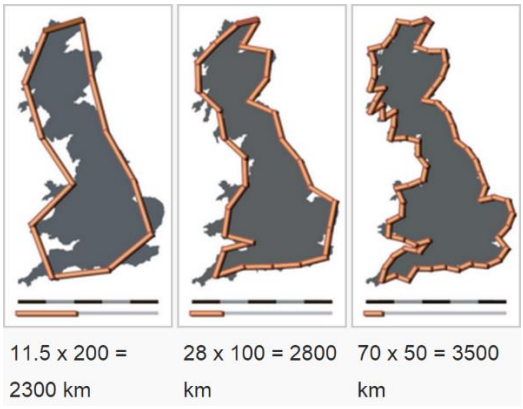

Figure 2-2. As the length of the measuring stick is scaled smaller and smaller, the total length of the coastline measured increases.

The concept of a fractal dimension rests in unconventional views of scaling and dimension [22]. As Figure 2-3 illustrates, traditional notions of geometry dictate that shapes scale predictably according to intuitive and familiar ideas about the space they are contained within, such that, for instance, measuring a line using first one measuring stick then another 1/3 its size, will give for the second stick a total length 3 times as many sticks long as with the first. This holds in 2 dimensions, as well. If one measures the area

of a square then measures again with a box of side length 1/3 the size of the original, one will find 9 times as many squares as with the first measure. Such familiar scaling relationships can be defined mathematically by the general scaling rule in Equation (2-1), where the variable N stands for the number of new sticks, ϵ for the scaling factor, and D for the fractal dimension:

$$N \propto \epsilon^{-D} \tag{2-1}$$

The symbol $\propto$ above denotes proportionality. This scaling rule typifies conventional rules about geometry and dimension – for lines, it quantifies that, because $N = 3$ when $\epsilon = 1/3$ as in the example above, $D = 1$, and for squares, because $N = 9$ when $\epsilon = 1/3$, $D = 2$.

The same rule applies to fractal geometry but less intuitively. To elaborate, a fractal line measured at first to be one length, when re-measured using a new stick scaled by 1/3 of the old may not be the expected 3 but instead 4 times as many scaled sticks long. In this case, $N = 4$ when $\epsilon = 1/3$, and the value of D can be found by rearranging (2-1):

$$\log_{\epsilon} N = -D = \frac{\log N}{\log \epsilon} \tag{2-2}$$

That is, for a fractal described by $N = 4$ when $\epsilon = 1/3$, $D = 1.2619$, a non-integer dimension that suggests the fractal has a dimension not equal to the space it resides in [20].

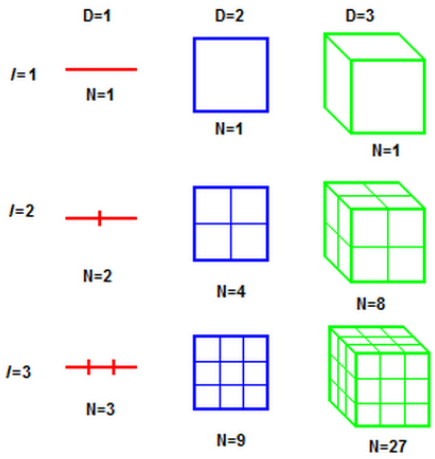

Figure 2-3. Traditional notions of geometry for defining scaling and dimension.

As is the case with dimensions determined for lines, squares, and cubes, fractal dimensions are general descriptors that do not uniquely define patterns. The value of D quantifies the pattern's inherent scaling, but does not uniquely describe nor provide enough information to reconstruct it.

Regularization Dimension:

The general idea is to define a fractal index for irregular functions based on the behavior of the lengths of less and less regularized versions of their graphs. The regularized versions are obtained by convoluting the function with a smooth kernel dilated by a scale parameter a. When a tends to 0, the kernel tends to the Dirac distribution and the regularized versions to the original graph.

A "fractal" graph will typically exhibit a power law for the regularized lengths as a function of a, with exponent $-d$. In this case, the regularization dimension is defined to be $1 + d$. In general, one uses as is customary lower and upper limits to obtain well-defined dimensions. The basic properties of the regularization dimension are similar to those of classical fractal dimensions, such as the box dimension

[23]. However, it has a number of advantages over other dimensions in the frame of signal and image processing. Indeed, thanks to its adaptive and analytical definition, it usually leads to estimations methods which are more precise than is the case for the box dimension and the Hausdorff dimension [24]. It also has interesting statistical properties. Indeed, if the data are corrupted with an additive white noise, one can easily distinguish, in the computation of the regularization dimension, the contribution of the noise and the one of the noise-free signal. This allows obtaining a robust estimator of the regularization dimensions of noisy signals. This applies to 1D as well as to 2D data. For more details on this and other aspects of the regularization dimension, see [25].

Since its introduction, regularization dimension has been used by various teams worldwide in many different applications, including the characterization of certain stochastic processes, statistical estimation, the study of mammography or galactograms for breast carcinomas detection, ECG analysis for the study of ventricular arrhythmia, encephalitis diagnosis from EEG, human skin analysis, discrimination between the nature of radioactive contaminations, analysis of porous media textures, well-logs data analysis, agro-alimentary image analysis, road profile analysis, remote sensing, mechanical systems assessment, and the analysis of video games [26] [27] [28] [29] [30].

2.4 Profile Measurement Techniques

In this section, the equipment employed to produce the profile data used in the present work are briefly introduced.

The RoLine 1130 Sensor uses 3D laser line technology to measure line scans (see Figure 2-4 Left). It can be mounted on a vehicle to measure the roughness profile of extended distances and produce a map owing to the auxiliary GPS IMU system. This system was used in the laboratory to measure a sample of 120-grit sandpaper (see Figure 2-4 Right). The disadvantages of this system are the low vertical and horizontal

resolution, and the substantial influence from sample reflectivity. Therefore, it's not suitable for this research.

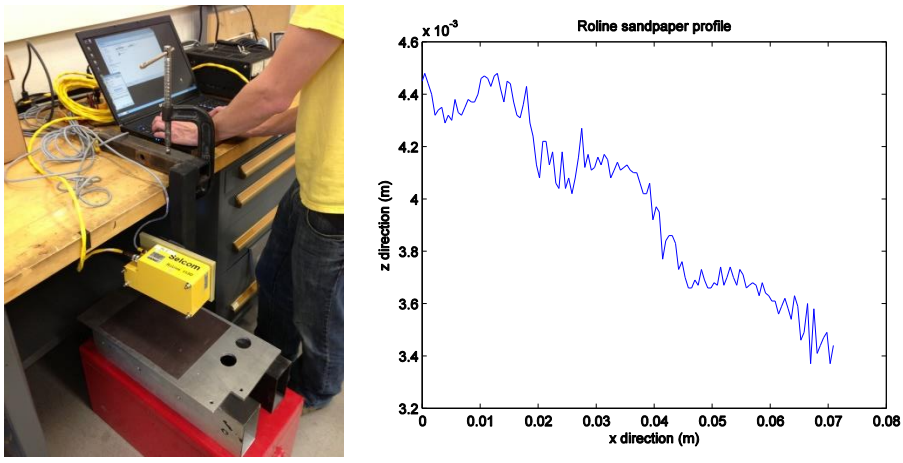

Figure 2-4. Left: RoLine 1130 Sensor; Right: a line-scan of 120 grit sandpaper.

The Zygo contact-type profilometer was used to measure a $\approx 1mm \times 1mm$ area of the 120-grit sandpaper (see Figure 2-5). It provides great spatial resolution. However, it's not portable, has low measurement speed, requires special sample preparation, is not able to measure high surface angles, can be easily damaged by surface or careless operators, has to do image stitching for larger area measurements, and is not capable of large Z measurement ranges. All in all, it's not the desirable profilometer for our application.

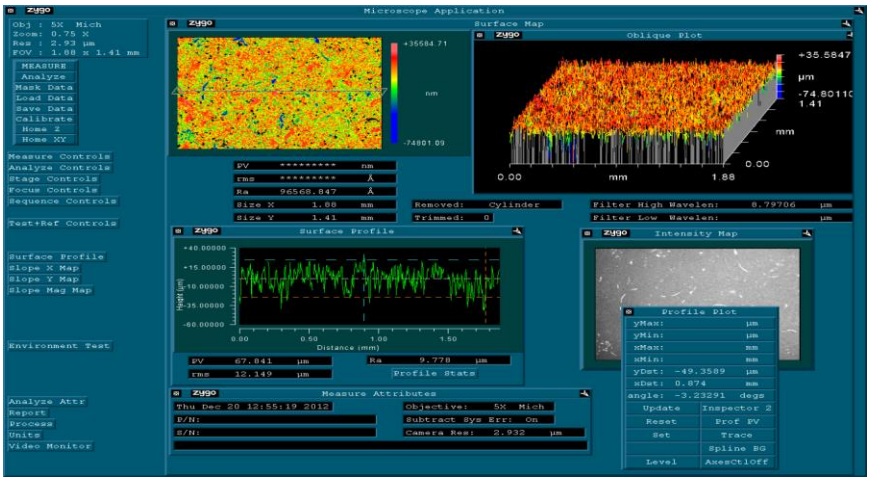

Figure 2-5. Zygo Contact-Type Profilometer; $\approx 1mm \times 1mm$ area of the 120 grit sandpaper.

We also used the KH-7700 3D Digital Microscope to measure a $\approx 1mm \times 1mm$ area of the 120 grit sandpaper (see Figure 2-6). KH-7700 reconstructs a 3D profile from 2D images at different depths of focus. Although this system delivers great resolution and large Z-range, it shares most of the disadvantages of the Zygo profilometer, namely, not being portable, low measurement speed, requiring special sample preparation and not being able of measuring high surface angles. There's no option for image stitching.

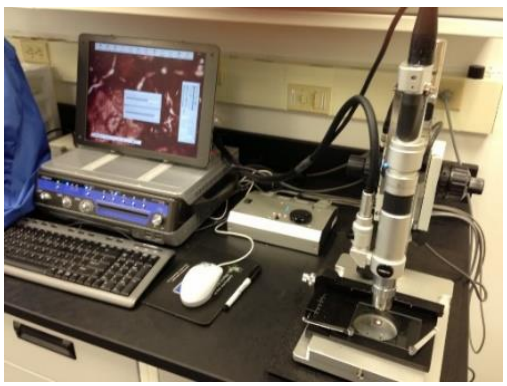

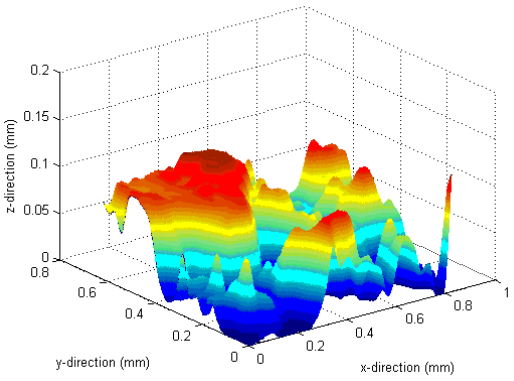

Figure 2-6. Left: KH-7700 3D Digital Microscope; Right: $\approx 1mm \times 1mm$ area of the 120 grit.

The Alicona Infinite Focus Sensor (see Figure 2-7) was used by Minh Tan Do in IFSTTAR to measure some of the gravel profiles we used for surface classification. This equipment measures large profiles and areas with good lateral resolution. However, the drop-out rate is higher than ideal.

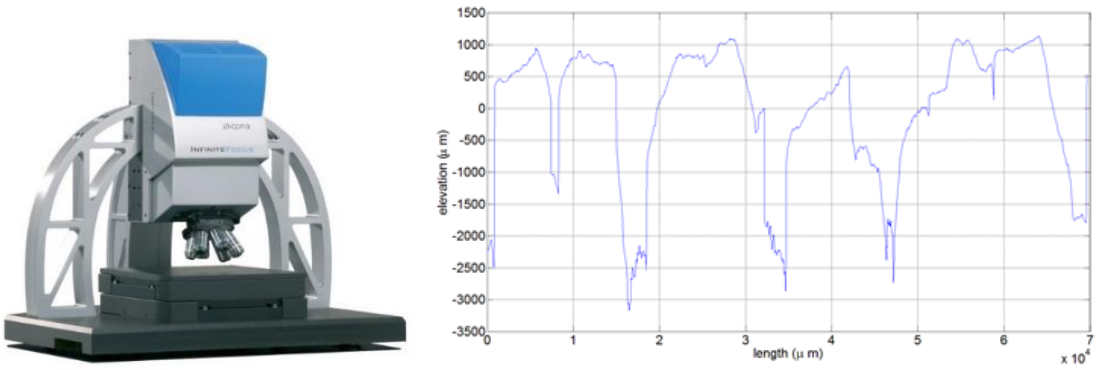

Figure 2-7. Left: Alicona Infinite Focus Sensor; Left: Line-scan of gravel cast into synthetic resin mold.

The OGP Digital Range Sensor System, DRS-8000 (see Figure 2-8) was used by George Dewey's group at the Michigan Tech Transportation Institute to measure highway pavements. We have used those measurements for profile characterization and classification.

Figure 2-8. OGP Digital Range Sensor System

CenTiRe recently purchased the Nanovea JR25 designed with leading edge optical pens using superior white light axial chromatism (see Figure 2-9). It offers excellent vertical and spatial resolution. It is easy to swap pens, which enables us to measure macro, micro, and sub-micro roughness. There are numerous add-on features available with Mountain's Ultra Analysis software, such as:

- Contour measurement: Helps measure precise dimensions of sample shapes and designs. The example application is for tread rubber.
- Fracture surface measurements.
- Worn surface subtraction (see Figure 2-10).
- Adhesion surface topography: Ensures intended adhesive strength.

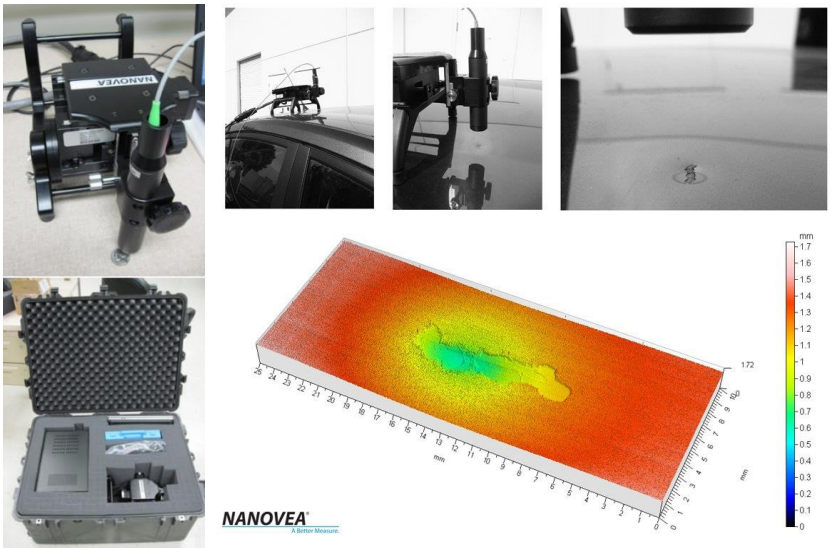

Figure 2-9. Nanovea JR25 portable profilometer

This system is used to profile sandpapers and realistic road surfaces such as asphalt and concrete.

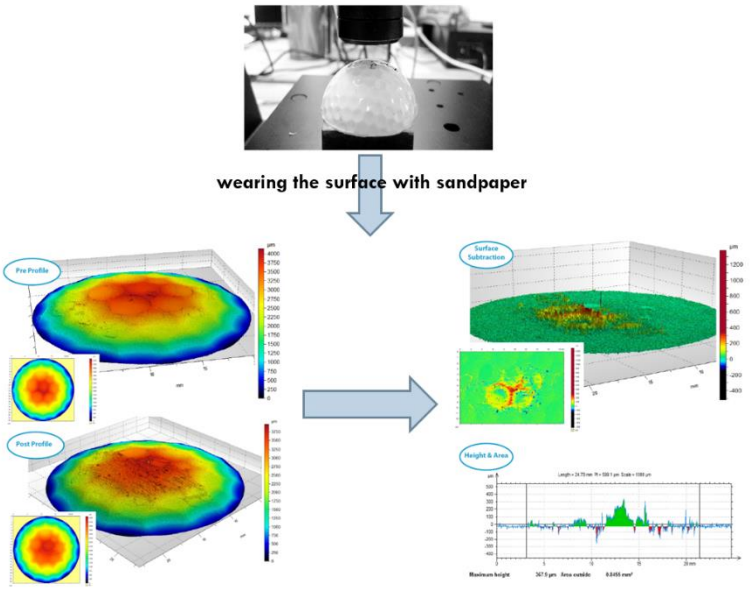

Figure 2-10. Surface wear subtraction with Nanovea JR25.

2.5 Characterization of Pavement Texture Using Surface Profiles

In this context, a spectral analysis of pavement surface profile signals is performed. The one- or two-dimensional surface profiles describe the pavement roughness amplitude as a function of the distance along a straight or curved trajectory over the pavement. The result of the frequency analysis will be a spatial frequency (or texture wavelength) spectrum. This spectrum can also be described in constant percentage bandwidth bands of octave or one-third-octave bandwidth, as will be seen in later sections. It has to be noted that spectral analysis as specified in this document cannot express all characteristics of the surface profile under study. In particular, the effects of asymmetry of the profile, e.g., the difference of certain functional qualities for positive and negative profiles cannot be expressed by the power spectral density, as it disregards any asymmetry of the signal.

The most common and preferred way of sampling the surface profile of a road section is along a straight line in the longitudinal direction of the road. Alternatively, the profilometer may follow other trajectories, adapted to the nature of the survey, e.g., transverse and oblique lines, circles, spirals or sinusoids. The measured profiles should be analyzed separately. When the measured profiles constitute a representative sample from the test section under consideration, the relative standard deviation may be regarded as an estimate of the degree of variation of the surface characteristics along the test section.

2.6 Profile Classification

The objective of this effort is to find texture properties, calculated from road profile measurement data, which can predict tire-pavement friction, i.e., characterize pavement surfaces with different coefficients of friction. For profile characterization, texture and fractal parameters are examined. Mean square roughness and PSD of the measured roughness, as well as an angular parameter from the Indenters method [31] are

used for classification of surfaces. They represent the effect of texture on tire-road friction. Several researches have claimed that road profiles are fractal [1], and that this feature is related to the friction properties of the road [2] [4]. Fractal parameters are grouped into global and local parameters. Since friction is a local phenomenon, one should expect local parameters to be correlated with friction. In the present work, fractal analysis is done on road surface profiles. To investigate the correlation between the fractal behavior of road profiles and friction, Correlation Exponent [32] and Regularization Dimension [25] as global fractal parameters and the Pointwise Holder Exponent [33] as a local fractal parameter are studied.

The ultimate goal is addressing issues faced by tire designers such as the ability to predict the pavement surface characteristics (e.g., rolling resistance, fuel efficiency, tire wear and traction) as they relate to the tire interaction in terms of the pavement surface features.

2.7 Thermo-mechanical properties of tread compounds

Dynamic mechanical analysis (abbreviated DMA, also known as dynamic mechanical spectroscopy) is a technique used to study and characterize materials. It is most useful for studying the viscoelastic behavior of polymers. A sinusoidal stress is applied and the strain in the material is measured, allowing one to determine the complex modulus. The temperature of the sample or the frequency of the stress are often varied, leading to variations in the complex modulus [34]. This approach can be used to locate the glass transition temperature of the material [35], as well as to identify transitions corresponding to other molecular motions [36]. A master curve at a given temperature can be used as the reference to predict curves at various temperatures by applying a shift operation.

2.8 Friction Measurement Methods

High speed dynamic friction testing offers a unique possibility to determine friction coefficients of rubber samples on different surfaces and under various operating conditions to predict compound and pattern influence on the grip and traction performance [37]. The Dynamic Friction Test Machine that is being developed is aimed at finding the dynamic friction coefficient between the tire tread and road surface at designated loads and slip velocities. A brief review of some of the existing friction measurement apparatuses and polishing devices is as follows.

The most common device for laboratory testing of friction is the British Pendulum Tester (BPT). The manually operated BPT provides an indicator of friction through the swinging of a pendulum-based rubber slider and its contact with the pavement surface. The elevation to which the pendulum swings after contact provides the basis for the friction indicator, termed British Pendulum Number (BPN). The BPT is a portable device and can be used for both laboratory and field measurements. BPT is employed for measuring the friction characteristics of pavement surface at low speeds [38]. The test method for measuring friction using BPT is specified in [39].

The Hoop friction apparatus developed at the University of Virginia is a rather unusual type of tribometer. It is designed for fundamental studies of stick-slip (Bredell, Johnson Jr [40]). The apparatus is consisted of a narrow ring of metal tubing whose inner diameter serves as the sliding surface. A conformal slider rides up to the inside of the hoop within a shallow groove designed to prevent its wandering laterally as the hoop is slowly rotated about its axis. Fixed to the slider is a polarizing filter, which rotates as the slider climbs the inner diameter of the hoop. Light transmitted through an externally mounted polarizing filter and through the filter on the slider is changed in intensity as the latter is rotated. Thus, the light intensity can be measured to permit determination of the friction force at “slip”.

The Dynamic Friction Tester (DFT) developed by Auburn National Center for Asphalt Technology as described in [41] consists of three rubber sliders that are spring mounted on a disk at a diameter of

$350\ mm$. The DFT system can be used to measure friction characteristics of laboratory-manufactured samples that are at least 450 by $450\ mm$. The test is started while the rotating disk is suspended over the pavement and driven by a motor to a particular tangential speed. Water is sprayed on the rubber pad and pavement interface through surrounding pipes to simulate wet weather friction. The disk is lowered and the motor is disengaged. By measuring the traction force in each rubber slider the coefficient of friction of the surface is determined. The DFT can be used to measure the friction as a function of speed over the range of 0 to 90 km/h with good reproducibility [42].

The HSLFT Linear Friction Tester by Altracon SA is used for the purpose of test method development on road friction [43]. It determines coefficient of friction of rubber samples on different surfaces and under various operating conditions to predict compound and pattern influence on the grip and traction performance. It generates x, y, z force and moment data. The linear induction motor enables sliding velocities of up to $10\ m/s$, generating accelerations up to $100\ m/s^2$. Utilizing this system, testing surfaces like asphalt and concrete, as well as snow and ice surfaces with comparable characteristics to the outdoors is possible. The entire system is installed in a controllable climate chamber, simulating any road type and condition. It is not capable of generating longitudinal slip, slip angle (steer), and camber nonetheless.

The MTS Flat-Trac Tire Test System is designed to perform steady-state force and moment testing of passenger car and light truck tires for the acquisition of high-quality cornering force data for vehicle handling models and tire qualification. This system is ideal for conducting tire tests that produce large lateral or longitudinal forces, such as slip angle sweep, sinusoidal slip angle, radial deflection, and tractive force tests. Vehicle manufacturers use Flat-Trac systems to capture high quality data for vehicle modeling and to qualify tires for vehicles. The standard configuration employs a multi-axis Dynamic CT Load Transducer.

A rotating disc machine for identification of motorcycle tire properties has been developed and built at the Department of Mechanical Engineering, University of Padova, Italy [44]. Motorcycle tires require specific testing facilities, since large camber angles are used, which influence the tire forces and moments. The disc has a diameter of three meters and the wheel is mounted on a hinged arm. This arm makes it possible to set the side-slip and camber angle. The machine is equipped with three load cells that measure tire forces and torques.

Michigan Department of Transportation (MDOT) uses an indoor wear track to determine the performance of individual coarse aggregate specimens by polishing them using the full scale smooth tire in accordance with ASTM 524 [45]. The test specimens are casted in molds and clamped along the circular wear track. The specimens are individually tested using a laboratory friction tester at specified intervals. The friction tester consists of freewheeling tire powered by a motor; the wheel is drooped on to the specimen after a speed of 40mph is reached. The test specimens are made using coarse aggregates samples.

The North Carolina State University Wear and Polishing Machine comprises of a circular track that is used to polish aggregate and asphalt specimens. The device consists of four individually mounted, free rolling wheels pivoted about a driven central shaft. Pneumatic rubber tires are used for polishing asphalt specimens. The diameter of wear track is 36 inches to the center of wheel path and holds 12 equally spaced specimens. The friction tests are performed on the specimens at specified intervals during polishing using BPT or NCSU Variable Speed Friction Tester. The device polishes the specimens in fairly short periods of time and does not use slurry or water during operation [46].

The Penn State Reciprocating Polishing Machine is used to polish the aggregate and mixture samples in the laboratory. The apparatus consists of a rubber pad which is oscillated back and forth on the specimen surface to be polished while slurry of water and abrasive are sprayed which prevent the overheating of the rubber surface [47]. After polishing, the friction properties of the specimen are measured using BPT.

Locked Wheel Skid Tester (LWST) [48] is the most commonly used device in the U.S. [49]. In this method, the relative velocity between the surface of the tire and the pavement surface is equal to the vehicle speed. The operator applies the brakes and measures the torque for one second after the tire is fully locked then computing the correspondent friction value. According to [50], the measurement of skid resistance using LSWT is affected by several factors including pavement surface texture, age of the pavement, and tire used. In 2005, [51] found that friction measurement using ribbed tire is sensitive to micro-texture and insensitive to macro-texture. In the U.S., the use of a ribbed tire [52] predominates but the use of the smooth tire [53] has been increasing recently. Ribbed tires are preferred by some people because they are less sensitive to water film thickness than the smooth tire. Dynatest 1295 Pavement Friction Tester (PFT) is a locked wheel tester used for the purpose of traveling the highway at normal traffic speeds and producing an accurate measurement and record of highway friction values using full size ASTM E501 or E524 test tires. The PFT is a relatively expensive system. Yet, it doesn't account for the coefficient of friction changing with respect to slip ratio. It utilizes a two-axis force transducer to measure both the horizontal (traction) value and the dynamic vertical load. Test speeds from 20 to 70 mph are feasible. The system provides the Locked Wheel Skid Number (SN) in real time.

In this research, a laboratory-based low-cost apparatus that can measure the friction between tire tread samples and surfaces with arbitrary roughness properties is designed and fabricated. The key advantages of this system compared to the existing systems are the ability to measure friction at orderly slip ratios, and the capability to embed the desired road surface samples. The different pavement and sandpaper samples are used with the developed friction test equipment to better understand the rubber-road contact. One potential future plan is to use the rubber friction tester and do friction measurements for dominant wavelengths that are obtained via spectral analysis and fabricated into the road disk. An algorithm can be developed to investigate the contributions of macro- and micro-texture constituents to rubber-road friction. This algorithm can determine which scales are dominant in the buildup of friction.

2.9 Contact Mechanics - Friction Estimation Methods

2.9.1 Empirical/ Semi-empirical equations

Empirical and semi-empirical friction estimation methods are currently the widely used methodologies, and are developed through gaining knowledge by means of direct friction measurement experiments. The measured data is analyzed quantitatively and qualitatively, and a correlation between the input variables and the outputs is formulated. However, fitting a set of data with fully empirical equations is a short-term solution (as opposed to physics-based methods), which works for only the actually investigated data set. Moreover, the fitting has to be adopted again as soon as one test condition changes. In what follows, three well-known semi-empirical friction prediction approaches are reviewed:

2.9.1.1 LuGre model

An example of an extensively used semi-empirical friction model is the LuGre model [54]. The LuGre model has become popular because it incorporates many of the observed features of frictional behavior. For example, imbedded within the LuGre model is the Stribeck effect. For small levels of slip velocity, the friction force exhibits a negative derivative with respect to slip velocity. This negative slope is one of the key features of friction that contributes to limit-cycle behavior and stick-slip oscillations in frictional systems. Furthermore, the LuGre model behaves like a linear spring/damper pair when it is linearized for small motions.

At the microscopic level, two surfaces make contact at various asperities. These asperities are represented with bristles, and the bristles deflect like a spring when there is a relative velocity between the two surfaces. The deflection of the springs gives rise to the friction force. If the deflection is sufficiently large, then the bristles will slip in a highly random manner because of the irregular surfaces. Although the

deflection of the bristles is random, the LuGre model only considers the average deflection. The average deflection of the bristles, Z, is modeled by the first-order differential equation:

$$\dot{Z} = V - \frac{|V|}{G(V)} Z \tag{2-3}$$

where V is the relative velocity between the two surfaces and $G(V)$ is a function that describes the Stribeck effect. The function $G(V)$ also allows the LuGre model to accommodate a higher static coefficient of friction than dynamic coefficient of friction:

$$G(V) = \frac{1}{\sigma_0}\left\{F_c + (F_s - F_c)e^{-\left(\frac{V}{V_s}\right)^2}\right\} \tag{2-4}$$

where F_C is the kinetic friction force, F_s is the static friction force, σ_0 is the aggregate bristle stiffness, and V_S is the Stribeck velocity. Finally, the LuGre friction force is given by

$$F_L(V, Z) = \sigma_0 Z + \sigma_1 \dot{Z} + \sigma_2 V \tag{2-5}$$

where σ_1 is a damping coefficient and σ_2 accounts for viscous friction.

The values used for the LuGre parameters are usually optimized using the Runge-Kutta method as the explicit solver [55].

2.9.1.2 Grosch numerical and experimental studies

In the sixties, Grosch studied the friction of several types of rubber against hard surfaces over a wide range of temperatures and sliding velocities. The highest velocity didn't exceed a few centimeters per second so that frictional heating was negligible. The results show that the friction increases with the sliding velocity to a maximum value and then falls [56].

The master curve on a rough abrasive track shows, in general, two peaks – one of these occurs at a velocity related to the frequency with which the track asperities deform the rubber surface. The maximum is absent on a smooth track and thus reflects the deformation losses produced by the passage of the asperities over the rubber surface. The other peak occurs in general at much lower velocities; it coincides in position with the single maximum obtained on a smooth surface (see Figure 2-11). Introduction of a fine powder (MgO) into the interface between the rubber and track eliminates this peak on both smooth and rough surfaces; it is therefore attributed to molecular adhesion. It appears therefore that friction arises from adhesion and deformation losses, and that both are directly related to the viscoelastic properties of the rubber.

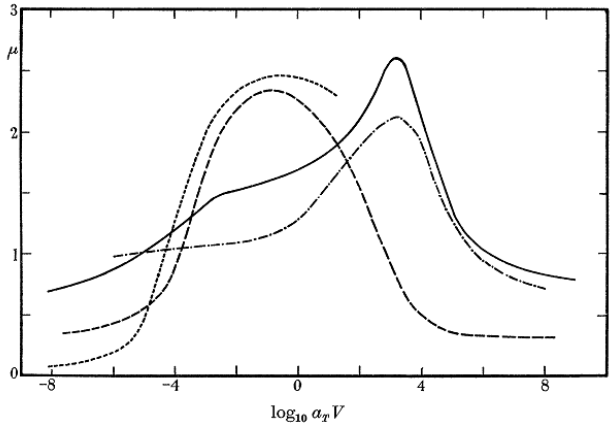

Figure 2-11 Master curves for the coefficient of friction of the acrylonitrile-butadiene rubber on four surfaces: – – – –, wavy glass; - - - - -, polished stainless steel; _____, clean silicon carbide; -.-.-.-, dusted silicon carbide; all curves referred to 20℃; *Reproduced from [56] with permission from Royal Society Publishing.*

2.9.1.3 Rado

Zoltan Rado developed a logarithmic friction model in his PhD thesis [1]. The model is a mathematical procedure describing the friction coefficient-slip speed curve completely for transient or variable slip processes. Unlike other models developed to date, this model separates the tire influence from that of the pavement influence on friction results. The model also describes and quantifies such very important parameters as the peak friction and the critical slip speed, making it possible to more precisely analyze the performance of tire and road surfaces. The resulting mathematical equation is given as shown in Equation (2-6):

$$\mu\,(V) = \mu_p\,.\,e^{-\left(\frac{\ln\left(\frac{V}{V_{peak}}\right)}{\hat{C}}\right)^2} \tag{2-6}$$

where μ_p, V_{peak}, and $\hat{C}$ are constants.

The obtained mathematical procedure was evaluated by fitting the model to data measured on 10 different surfaces during the PIRAC international experiment. The R-value of the fits ranged from $R = 0.92$ to the higher limit of $R = 0.996$ for a target sliding speed of $60\ km/h$ and were between 0.81 and 0.986 for a target sliding speed of $90\ km/h$. It was also shown that the model is capable of describing the variations in the coefficient of friction-slip speed curve to a very high degree.

As for texture description, two new models were developed and discussed in detail, namely the Markov Random Field model [57], and the Fractal Surface model [58].

2.9.2 Physics-based friction models

A thorough, physics-based friction model could be a tool that can facilitate better predictions. The model should take account of rubber's thermo-mechanical properties, take in mathematical description of the road, account for ambient conditions, and possibly include flash heating. An extension of some physics-based models could be potentially utilized to study the effects of road's micro- and macro-texture, and include the existence of water on the track. The focus is on wet ABS braking conditions, i.e., sliding speeds of $10^{-4} - 10^{1}\ m/s$ and reference temperatures of $20 - 40\ C$.

2.9.2.1 Greenwood-Williamson theory

When two bodies with rough surfaces are pressed into each other, the true contact area A is much smaller than the apparent contact area A_0. In contact between a "random rough" surface and an elastic half-space, the true contact area is related to the normal force F by [59] [60] [61]:

$$A = \frac{\kappa}{E^* h'} F \tag{2-7}$$

with h' equal to the root mean square (also known as the quadratic mean) of the surface slope and $\kappa \approx 2$. The median pressure in the true contact surface

$$p_{av} = \frac{F}{A} \approx \frac{1}{2} E^* h' \tag{2-8}$$

can be reasonably estimated as half of the effective elastic modulus E^* multiplied with the root mean square of the surface slope h' .

For the situation where the asperities on the two surfaces have a Gaussian height distribution and the peaks can be assumed to be spherical, the average contact pressure is sufficient to cause yield when $p_{av} =$

$1.1\sigma_y \approx 0.39\sigma_0$ where σ_y is the uniaxial yield stress and σ_0 is the indentation hardness. Greenwood and Williamson [60] defined a dimensionless parameter Ψ called the plasticity index that could be used to determine whether contact would be elastic or plastic.

The Greenwood-Williamson model requires knowledge of two statistically dependent quantities; the standard deviation of the surface roughness and the curvature of the asperity peaks. An alternative definition of the plasticity index has been given by Mikic [61]. Yield occurs when the pressure is greater than the uniaxial yield stress. Since the yield stress is proportional to the indentation hardness σ_0, Mikic defined the plasticity index for elastic-plastic contact to be

$$\Psi = \frac{E^* h'}{\sigma_0} > \frac{2}{3} \tag{2-9}$$

In this definition Ψ represents the micro-roughness in a state of complete plasticity and only one statistical quantity, the rms slope, is needed which can be calculated from surface measurements. For $\Psi < \frac{2}{3}$, the surface behaves elastically during contact.

In both the Greenwood-Williamson and Mikic models the load is assumed to be proportional to the deformed area. Hence, whether the system behaves plastically or elastically is independent of the applied normal force.

2.9.2.2 Persson model

Bo Persson started the development of a physics-based contact mechanics model in 1990's and established the Multiscale Consulting Institute dedicated to this research [8]. They approached the problem by using the theory of elasticity (assuming an isotropic elastic medium for simplicity), to calculate the displacement field on a surface in response to the surface stress distribution. By calculating the frictional shear stress, the energy dissipated during the time period t_0 equals:

$$\Delta E = \sigma_f A_0 v t_0 \quad (2\text{-}10)$$

where A_0 is the surface area, and σ_f is the shear stress. When rubber slides on a hard rough substrate, the surface asperities of the substrate exert oscillating forces on the rubber surface leading to time-dependent deformations on the rubber surface and energy dissipation via the internal friction of the rubber. Persson's theory is based on the viscoelastic energy dissipation in the rubber due to hysteresis at multiple magnification levels. The model can be used when surfaces have roughness on many different length scales, i.e., fractal and self-affine surfaces. Unlike Continuum Mechanics approaches that neglect adhesion (e.g., Hertz model), this method takes into account both adhesion & hysteresis. The surface roughness enters into the equations via the correlation function (surface roughness power spectrum). In this framework, friction is a function of frequency dependent viscoelastic modulus of rubber, surface roughness, contact pressure, contact temperature, sliding velocity, wavevector, and magnification (see Equation (2-11)). Wavevector is a vector whose magnitude is the wavenumber ($= 2\pi/\lambda$) and its direction is the direction of wave propagation. Magnification, $\zeta = \lambda_0/\lambda$, refers to some arbitrary chosen reference length scale, where λ_0 is the roll-off wavelength, and λ is the shortest wavelength roughness which can be resolved at magnification ζ.

Assume that an elastic solid with a flat surface is squeezed against a hard, randomly rough substrate. Figure 2-12 shows the contact between two solids at increasing magnification ζ. At low magnification (ζ ≈ 1) it looks as if complete contact occurs between the solids at many macroasperity contact regions. But when the magnification is increased, smaller length scale roughness is detected, and it is observed that only partial contact occurs at the asperities. In fact, if there were no short distance cut-off the true contact area would vanish. In reality, however, a short distance cut-off will always exist since the shortest possible length is an atomic distance. For rubber friction the effective short distance cut-off may be much larger (of micrometer order).

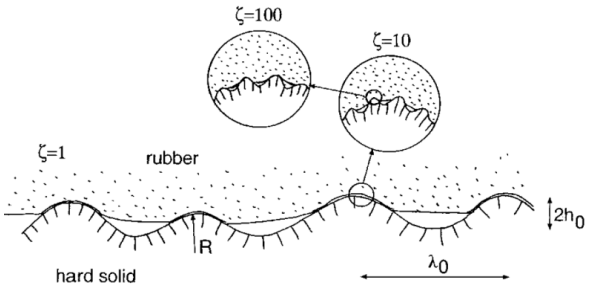

Figure 2-12. A rubber block (dotted area) in adhesive contact with a hard rough substrate (dashed area); *Reproduced from [11] with permission from AIP Publishing.*

$$\mu = \frac{1}{2}\int d^2q\, q^2\, cos\phi\, C(q)P(q)Im\frac{E(qvcos\phi)}{(1-v^2)\sigma_0} \qquad (2\text{-}11)$$

The algorithm will be explained in more detail in the Methodology section.

2.9.2.3 Klüppel model

Like Persson, Klüppel and his colleagues also started their research in the 1990's. The fundamentals of their theory are very similar to Persson's. Their approach relates the rubber friction on rough surfaces to the dissipated energy of the rubber during sliding stochastic excitations on a broad frequency scale. The description of the dynamic contact is treated within the framework of a generalized Greenwood-Williamson theory for rigid-soft frictional pairings. The effect of surface roughness is obtained from a fractal analysis of the road texture measured via a profilometer. The surface roughness enters into the equations via the correlation function (surface roughness power spectrum). The results are reported to be in agreement with the classical friction data of Grosch. The model adopts the view of Persson that assumes hysteresis energy losses arising from the deformation by surface asperities as the dominant factor of rubber friction. Under dry conditions, both hysteresis and adhesion components contribute to the

frictional process. Under wet conditions, the adhesion component of the total friction is drastically reduced, whereas the hysteresis loss remains largely unaffected. Yet, even under wet conditions, statistically distributed islands of dry contact can form. This mechanism can be hindered by the use of detergents (avoids using the semi-empirical equations of interfacial shear stress through putting off the contribution from adhesion force, by using detergents). This theory significantly improves the description of wet and dry friction behavior using the “two scaling ranges” approach. The algorithm will be explained in more detail in the Methodology section.

2.9.2.4 Indenters method – Stefani model

In this method, the detailed mechanisms of indentation and adhesion involved in some concepts related to the modeling of a tire with a solid Kelvin phenomenon is justified by the comparison of the results to friction SRT which is closely related to the rate of longitudinal slip. The Indenters technique is used in combination with Stefani friction model [5]. Preliminary results on the Indenters obtained by Minh Tan Do are published in [62], showing the relevance of geometric parameters extracted from the road profiles to describing friction.

The development of the forces of friction depends on the instantaneous normal load, various properties of the tires, the geometric characteristics of the road and contact conditions (dry, the presence of pollutants and water). The complexity of the phenomena involved explains the absence of complete physical models for calculating friction forces of a tire on a road from parameters related to the road and the tire. As part of the research program "Infrastructure and road safety" LCPC, Surface Section of Roads and Vehicle Dynamic Adhesion proposed to tackle the problem by a local approach to better understand and quantify the phenomena at the contact between a rubber pad and of the road unevenness. The work aims at better understanding and quantifying the role of micrometer asperities. The fractality of road profiles is proven, and the contribution of Hölder interpolation techniques and multifractal denoising on the calculation of

friction is shown. The rubber in tires is a vulcanized elastomer, and its molecular properties result in a viscoelastic behavior. The authors of [62] have determined the areas of the profile that may come into contact with the tire. These are called indenters (see Figure 2-13). An indenter breaks the possible water film and deforms the rubber of the tire to generate friction. Obviously, the magnitude of these two properties, depends on the shape of the indenter ([63] and [64]), but also the density and topography created by their relative positions. An indenter is defined as the triangle formed by a peak and two adjacent valleys. The shape of the indenter is characterized by the cotangent of the half angle (α) at the top. The topography is represented by the angle θ. α and θ are defined as,

$$\theta = \tan^{-1}\left|\frac{Z_{s+1} - Z_s}{X_{s+1} - X_s}\right| \tag{2-12}$$

where Z_s, X_s are the height and the abscissa of the S_{th} summit.

$$\alpha = \frac{1}{2}\left[\tan^{-1}\left|\frac{X_e - X_{e-1}}{Z_e - Z_{e-1}}\right| + \tan^{-1}\left|\frac{X_{e+1} - X_e}{Z_{e+1} - Z_e}\right|\right] \tag{2-13}$$

where Z_e, X_e are the height and the abscissa of the e_{th} extremum.

The mean values of $cotan(\alpha)$ and θ are then correlated to the values of friction SRT. It was concluded that the shape descriptors and reliefs are highly correlated to friction SRT.

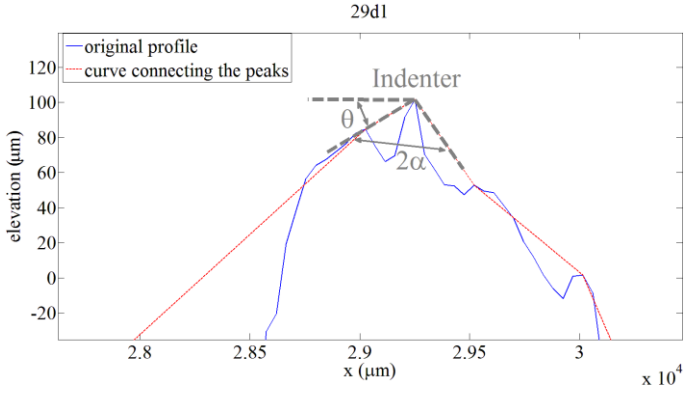

Figure 2-13. Definition of shape and relief parameters

In the Stefani contact model, the two angular parameters are used to explain the influence of the surface texture on the friction. The approach describes contact between a solid Kelvin model and a profile pattern substrate. Due to its simplicity, this model will allow to easily take the input parameters defined above describing the microtexture. A pattern consists of two peaks separated by a valley. The decisive parameters of the pattern are α_1, α_2, the widths $l1$, $l2$ and θ_1, θ_2 (see Figure 2-14 left). It is assumed that the Kelvin model moves at speed V. The model assumes that the friction comes only from the deformation of the solid. This is a realistic assumption in the case of water on the surface. In fact, in the presence of water on the substrate, the molecular bonds are non-existent.

By studying the kinematics of contact, we can calculate the forces and friction. The vertical force and horizontal force are given respectively by the following expressions ([62]):

$$f_v = \frac{1}{T}\left(\int_0^{t_1} \frac{E}{\tan(\alpha_1)}\left[h_0 \tan(\alpha_1) + l1 - V(t+\tau)\right] dt\right) + \frac{1}{T}\left(\int_0^{t_2} \frac{E}{\tan(\alpha_2)}\left[h_0 \tan(\alpha_2) + l2 - V(t-\tau)\right] dt\right)$$

$$f_h = \frac{1}{T}\left(\int_0^{t_1} -\frac{E}{[\tan(\alpha_1)]^2}\left[h_0 \tan(\alpha_1) + l1 - V(t+\tau)\right] dt\right) + \frac{1}{T}\left(\int_0^{t_2} \frac{E}{[\tan(\alpha_2)]^2}\left[h_0 \tan(\alpha_2) + l2 - V(t-\tau)\right] dt\right) \quad (2\text{-}14)$$

$$\mu = \frac{f_h}{f_v}$$

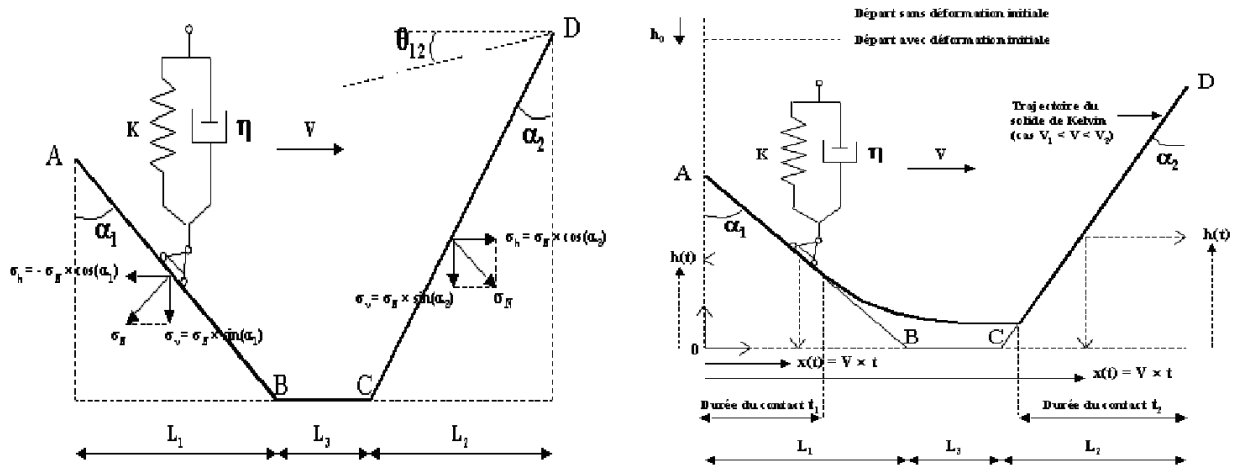

Figure 2-14. Left: Basic geometry of the Stefani model; Right: Kinematics of solid contact Kelvin model; *Reproduced from [5] with permission from the author*.

where $T = (l1 + l2 + l3)/V$ is the total duration of the passage (see Figure 2-14). h_0 is the starting height of the solid and the E is the modulus of the rubber. τ is the relaxation time of the rubber.

For each sample, a pattern is defined by characterizing the texture of the surface. Then the parameters of the pattern are introduced into the Stefani model. This allows one to calculate the vertical stress and the horizontal force. After some simplifying assumptions ($h_0 = 0$, $l1 = l2$ and $l3 = 0$),

$$f_v = \frac{VL}{2E}\left[\frac{Lt_1}{\tan(\alpha_1)} + \frac{Lt_2}{\tan(\alpha_2)} - \frac{V}{2}\left(\frac{t_1^2}{\tan(\alpha_1)} + \frac{t_2^2}{\tan(\alpha_2)}\right) - V\tau\left(\frac{t_1}{\tan(\alpha_1)} - \frac{t_2}{\tan(\alpha_2)}\right)\right] \qquad (2\text{-}15)$$

and

$$f_h = \frac{VL}{2E}\left[\frac{Lt_2}{(\tan(\alpha_2))^2} - \frac{Lt_1}{(\tan(\alpha_1))^2} - \frac{V}{2}\left(\frac{t_2^2}{(\tan(\alpha_2))^2} - \frac{t_1^2}{(\tan(\alpha_1))^2}\right) + V\tau\left(\frac{t_1}{(\tan(\alpha_1))^2} + \frac{t_2}{(\tan(\alpha_2))^2}\right)\right] \quad (2\text{-}16)$$

There is a strong correlation between SRT and the estimated friction. The calculation by taking into account the scale of roughness (that of the measured profile) underestimates the friction. Also, considering the ripple scale (profile envelope of all the vertices of indenter) would greatly improve the result. Friction calculated from the average pattern across the ripple is added to that obtained on the average pattern of the roughness scale.

3 Methodology

In this chapter, some of the existing procedures, as well as the ones developed during the course of this research, to produce the required pieces for contact modeling, friction measurement, and friction prediction are explained.

First, the roughness profile measurement approaches are discussed followed by the techniques to characterize those measurements and extract the parameters that will be used for friction estimation. Next, some parameters that can help predict tire-road friction, using texture measurements, are introduced. Also, the techniques for generating and utilizing viscoelastic master curves of tire tread compounds for friction prediction are explained. In what follows, the existing algorithms for modeling rubber-rough substrate contact and friction prediction are listed and detailed. In the last section, the configuration of the developed Dynamic Rubber Friction Tester (DRFT) is introduced.

3.1 Measurement of surface roughness profile

The Nanovea JR25 is used to measure different road surfaces and sandpaper samples [65]. Several surface parameters are automatically calculated including the most common, 'average surface roughness' (see Figure 3-1).

Wavelength of light (color!) reflected in focus off the surface with the highest intensity in the visible light spectrum is physically measured [66]. The measurement is performed by Raster scan, getting each point associated to the wavelength of the maximum peak. The measurements become height information through direct calibration of physical wavelength for the specific optic to a traceable displacement. There are no mathematical algorithms involved. The limitations are thin films with highly reflective substrate, surface tilt, relative axial and radial motions (not a concern during raster scan), self-imaging effects found on localized small shape, and the size of the focus point. Consequently, there are limits to the capability of the technique to measure angular surfaces. However, these limits far surpass what is achievable with Coherence Scanning Interferometry (CSI) for the same height range [67] [68]. Thin film with high reflective substrate can be taken in account using the specific selection of peaks at the specific wavelength as to follow one or the other. All variation related to edges is limited to the specific point measured because it is a scanning technique.

Limited range of restrictions results in more accurate roughness measurement. Good resolution is achieved, as well as high accuracy/precision and repeatability. Unlike CSI, this technique is not sensitive to measurement parameters. Special care is required to make sure that the light source is not saturated. For the sample setup, no special leveling procedure is required.

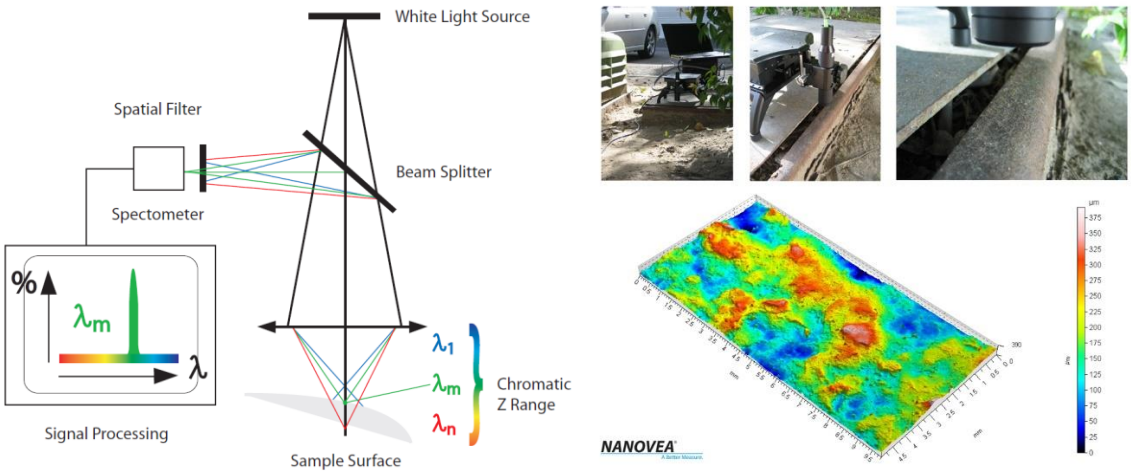

Figure 3-1. The axial chromatism technique uses a white light source, where light passes through an objective lens with a high degree of chromatic aberration. The refractive index of the objective lens will vary in relation to the wavelength of the light. In effect, each separate wavelength of the incident white light will re-focus at a different distance from the lens (different height). When the measured sample is within the range of possible heights, a single monochromatic point will be focalized to form the image. Due to the confocal configuration of the system, only the focused wavelength will pass through the spatial filter with high efficiency, thus causing all other wavelengths to be out of focus. The spectral analysis is done using a diffraction grating. This technique deviates each wavelength at a different position, intercepting a line of CCD, which in turn indicates the position of the maximum intensity and allows direct correspondence to the Z height position.

3.2 Profile characterization techniques

For characterization of pavement texture, a spectral analysis of pavement surface profile signals is performed. The one- or two-dimensional surface profiles describe the pavement roughness amplitude as a function of the distance along a trajectory over the pavement. The result of the frequency analysis will be a spatial frequency (or texture wavelength) spectrum. In what follows, the necessary steps to obtain the power spectral density of a surface profile for rubber-pavement friction prediction are explained.

Treatment of drop-outs:

The measurements on a particular pavement should be considered valid only if the drop-out rate for the evaluation length in question is not more than 10%. Linear interpolation is used to replace the invalid samples. Several drop-outs in a series may occur, as is illustrated in Figure 3-2. When a series of invalid samples is preceded and followed by valid samples, each of the invalid samples has to be replaced by an interpolated value z_i according to Equation (3-1),

$$z_i = \frac{z_n - z_m}{n - m}(i - m) + z_m \tag{3-1}$$

where i is the sample number where the value is invalid, m is the sample number of the nearest valid value before i, n is the sample number of the nearest valid value after i, z_i is the interpolated value for sample i, z_m is the value of sample m, and z_n is the value of sample n.

Measurements with higher drop-out rates than the allowable values should be discarded. The Mountain Software that accompanies the JR25 profilometer has the feature to treat the drop-outs.

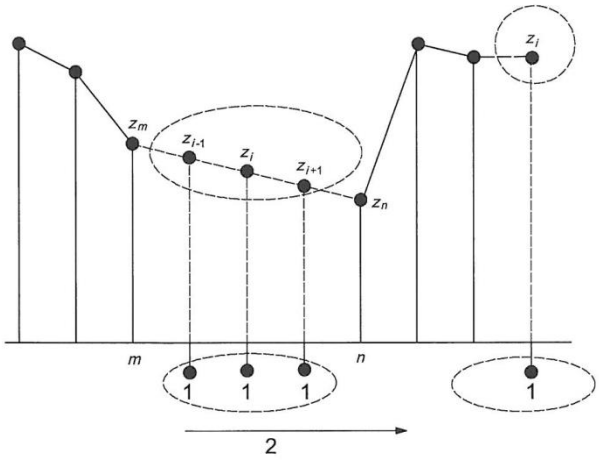

Figure 3-2. Illustration of interpolation and extrapolation of drop-outs; *Reproduced from [69] with permission from ANSI.*

Slope and Offset Suppression:

Let z_i be the measured signal value for sample i at x_i and N be the number of samples within the evaluated signal. Then slope b_1 of the surface profile is given by,

$$b_1 = \frac{12\sum_{i=0}^{N-1} iz_i - 6(N-1)\sum_{i=0}^{N-1} z_i}{N(N+1)(N-1)} \tag{3-2}$$

The offset b_0 of the surface profile is given by,

$$b_0 = \frac{1}{N}\sum_{i=0}^{N-1} z_i - b_1 . \frac{1}{2}(N-1) \tag{3-3}$$

The measured signal value z_i should be corrected for slope and offset according to Equation (3-4) (see Figure 3-3). The corrected sample signal value Z_i is,

$$Z_i = z_i - b_1 i - b_0 \qquad \text{for } i = 0, \ldots, N-1 \tag{3-4}$$

For the calculation of the slope of offset correction, the surface profile is treated as a function of the sample number i, and not the measured distance $x(= i\Delta x)$.

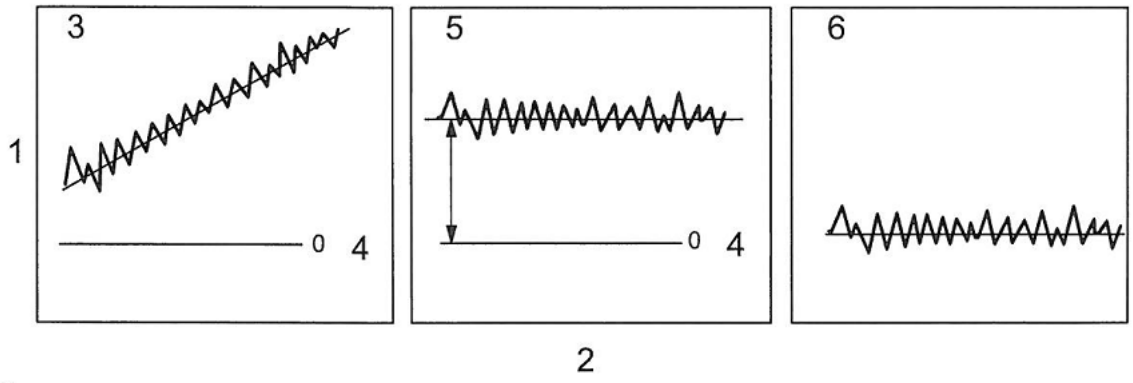

Key
1 vertical distance
2 horizontal distance
3 original profile
4 0 level
5 slope suppression applied
6 offset suppression applied

Figure 3-3. Illustration of slope and offset suppressions; *Reproduced from [69] with permission from ANSI.*

Windowing:

The Discrete Fourier Transform is based on the assumption that the input signal repeats itself with a period equal to signal duration. At the edges of the signal, there might be a jump in the composite signal. This effect is known as leakage that affects the spectrum obtained. To prevent leakage, a window that reduces the signal to zero at the edges should be applied.

The preferred window type to be used for spectral analysis of surface profiles is the Hanning window [70]. This window has the shape of a squared cosine and is defined as (see Figure 3-4 Left):

$$w_{i,H} := \frac{1-\cos(2\pi i/N)}{2} = 1 - \cos^2(\frac{\pi i}{N}) \qquad \text{for } i = 0, \dots, N-1 \tag{3-5}$$

Because of its shape, the Hanning window reduces the effective length of a signal, which influences the low frequency content of the signal. Therefore, an alternative window that was used in this research is the Split Cosine Bell Window (SCBW; sometimes indicated as Cosine Digital Tapering Window) [69]. This windowing method is specifically handy when the evaluation length is rather short. The shape of the SCBW is that of an increasing squared cosine in the first tenth of the window length and a decreasing squared cosine in the last tenth. In the intermediate section of eight tenth of the length, the window is equal to unity, as follows (see Figure 3-4 Right),

$$w_{i,C} := \begin{cases} \cos^2\left(\dfrac{5\pi i}{N} - \dfrac{\pi}{2}\right) & for\ 0 \le i < N/10 \\ 1 & for\ N/10 \le i \le 9N/10 \\ \cos^2\left(\dfrac{5\pi i}{N} - \dfrac{9\pi}{2}\right) & for\ 9N/10 < i < N/10 \end{cases} \tag{3-6}$$

A disadvantage of the SCBW is a loss of spectral resolution compared to the Hanning window. However, actual roads do not tend to have such regular deformations with very specific wavelength peaks appearing in the spectrum. Therefore, the spectral resolution is not an important issue here.

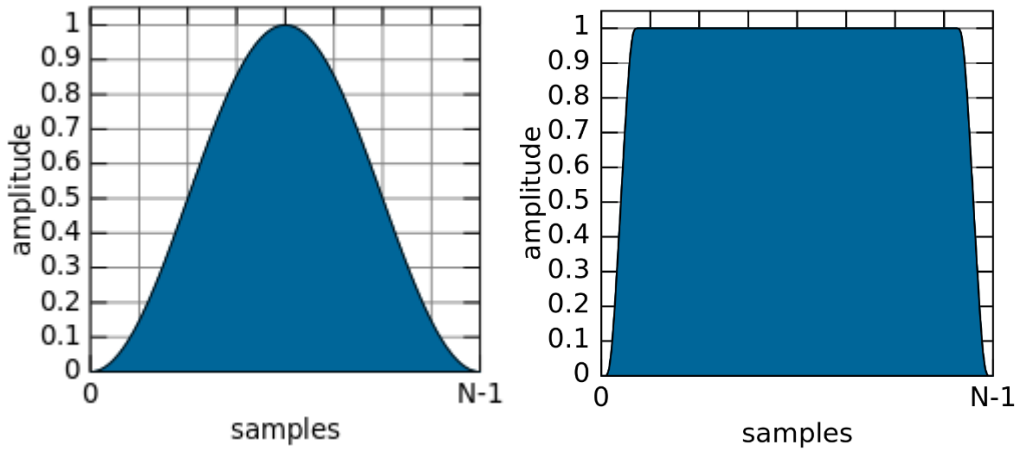

Figure 3-4. Left: Hanning window; Right: Split Cosine Bell window.

3.2.1 Persson's method

The Discrete Fourier Transform (DFT) Z_k of the windowed profile is defined by,

$$Z_k = \frac{1}{N}\sum_{i=0}^{N-1} Z_{i,win}\, \mathrm{e}^{-j\left(\frac{2\pi k}{N}\right)i} \qquad \text{for} \quad k = 0, \dots, N-1 \tag{3-7}$$

Depending on the software package used to calculate the DFT, the factor $\frac{1}{N}$ might be disregarded or replaced by $\frac{1}{\sqrt{N}}$. This can be checked by applying Parseval's theorem defined as,

$$\sum_{i=0}^{N-1} \left|Z_{i,win}\right|^2 = N \sum_{k=0}^{N-1} |Z_k|^2 \tag{3-8}$$

which shows the total power of the signal is equal in spatial frequency and space domains.

The result of the DFT is a constant bandwidth narrow band spectrum with complex values. The bandwidth depends on the evaluation length l and is equal to,

$$\Delta f_{sp} = \frac{1}{l} \tag{3-9}$$

The frequency scale starts at 0 with steps equal to Δf_{sp} until $(N-1)\Delta f_{sp}$ (note: $N\Delta f_{sp} = 1/\Delta x$). Only the frequencies up to $(\frac{1}{2}N - 1)\Delta f_{sp}$ should be used for further evaluation. To obtain the power spectral density (PSD) from the results of a DFT, the amplitude of each narrow band should be squared and divided by the spectral bandwidth according to Equation (3-10),

$$Z_{PSD,k} = \frac{2|Z_k|^2}{\Delta f_{sp}} \qquad \text{for} \quad k = 0, \dots, (\tfrac{1}{2}N - 1) \tag{3-10}$$

The surface roughness power spectrum $C(q)$ of an area (see Figure 3-5) is defined by,

$$C(q) = \frac{1}{(2\pi)^2} \int d^2x \langle h(x)h(0)\rangle e^{-iq.x} \tag{3-11}$$

Where q is the wavevector, and $h(x)$ is the substrate height measured from the average plane defined so that $\langle h(0)\rangle = 0$. The $\langle \dots \rangle$ stand for ensemble averaging, or averaging over the surface area, i.e., averaging over a collection of different surfaces with identical statistical properties. $\langle h(x)h(0)\rangle$ is basically the average of the autocorrelation of the height profile signal.

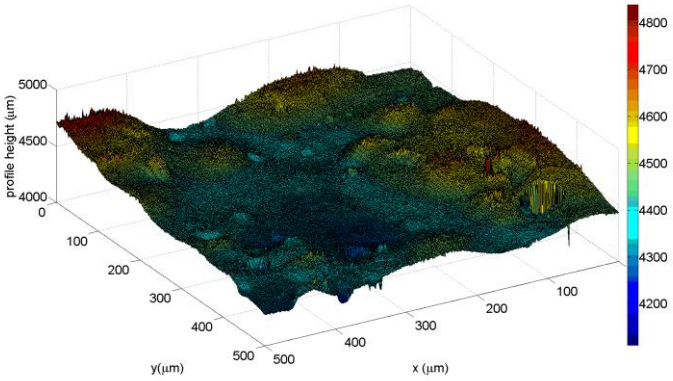

Figure 3-5. 2D area profile of an asphalt pavement.

We have assumed that the statistical properties of the substrate are translationally invariant and isotropic so that $C(\boldsymbol{q})$ only depend on the magnitude $q = |q|$ of the wavevector $\boldsymbol{q}$. Then,

$$\langle h(x)h(0)\rangle = \int d^2q\, C(q)\, e^{iq.x} \tag{3-12}$$

so that the RMS roughness amplitude $h_0 = \langle h^2\rangle^{\frac{1}{2}}$ is determined by,

$$\langle h^2\rangle = \int d^2qC(q) = 2\pi \int_0^\infty dq\, q\, C(q) \tag{3-13}$$

In reality, there will always be an upper, q_1, and a lower, q_L, limit to the q-integral in Equation (3-13). Thus, the largest possible wavevector will be of order $2\pi/a$, where a is some lattice constant, and the smallest possible wavevector is of order $2\pi/L$, where L is the linear size of the surface. Many surfaces tend to be nearly self-affine fractal. A self-affine fractal surface has the property that if part of the surface is magnified, with a magnification which in general is appropriately different in the perpendicular direction to the surface as compared to the lateral directions, then the surface 'looks the same', i.e. the statistical properties of the surface are invariant under the scale transformation. For a self-affine surface the power spectrum has the power-law behavior:

$$C(q) \sim q^{-2(H+1)} \tag{3-14}$$

where the Hurst exponent H is related to the fractal dimension D_f of the surface via $H = 3 - D_f$. Of course, for real surfaces this relation only holds in some finite wavevector region $q_0 < q < q_1$, and in a typical case $C(q)$ has the form shown in Figure 3-6. Note that in many cases there is a roll-off wavevector q_0 below which $C(q)$ is approximately constant. Asphalt and concrete road pavements have nearly perfect self-affine fractal power spectra, with very well defined roll-off wavevector $q_0 = 2\pi/\lambda_0$ of order $1000\, m^{-1}$, corresponding to $\lambda_0 \approx 1\, cm$, which reflect the largest stone particles used in the asphalt. From the slope of the curves for $q > q_0$ one can deduce the fractal dimension $D_f \approx 2.2$, which is typical for asphalt and concrete road surfaces.

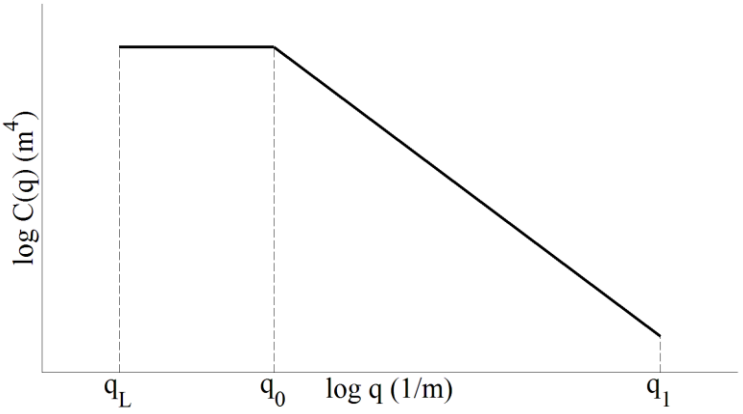

Figure 3-6. Surface roughness power spectrum of a surface which is self-affine fractal for $q_1 > q > q_0$. The long distance roll-off wavevector q_0 and the short distance cut-off wavevector q_1 depend on the system under consideration. The slope of the $\log C - \log q$ relation for $q > q_0$ determines the fractal exponent of the surface. The lateral size L of the surface (or of the studied surface region) determines the smallest possible wavevector $q_L = \frac{2\pi}{L}$.

Simplified version of $C(q)$ for self-affine surfaces is given by,

$$C(q) \approx k\left(\frac{q}{q_0}\right)^{-2(H+1)} \tag{3-15}$$

Now, to restrict the Fourier transform of $h(x)$ to a square area A, we can replace $h(\boldsymbol{q})$ with $h_A(\boldsymbol{q})$,

$$h_A(\boldsymbol{q}) = \frac{1}{(2\pi)^2}\int_A d^2x\, h(x)\, e^{-iq.x} \tag{3-16}$$

With N data points along the x and y coordinates, $h(x)$ is sampled and its values are known only at the points $x = (n_x, n_y)a = na = x_n$, where $n_x = 1, \dots, N$ and $n_y = 1, \dots, N$ are integers. By sampling the Fourier transform too, in the $\boldsymbol{q}$ space,

$$\boldsymbol{q} = (q_x, q_y) = (\frac{2\pi m_x}{L}, \frac{2\pi m_y}{L}) \tag{3-17}$$

where $m_x = 0, \dots, N-1$ and $m_y = 0, \dots, N-1$. Then,

$$h_A(\boldsymbol{q}) \approx \frac{a^2}{(2\pi)^2}\sum_n h_n\, e^{-i2\pi N(m_x n_x + m_y n_y)} = \frac{a^2}{(2\pi)^2} H_m \tag{3-18}$$

where H_m is the two dimensional DFT of h_n, and,

$$C(q) = \frac{(2\pi)^2}{A}\langle |h_A(\boldsymbol{q})|^2 \rangle \tag{3-19}$$

where $A = L^2$ is the surface area under study.

Let's assume that the surface roughness is isotropic and the statistical properties are translationally and directionally invariant. Then $C(\boldsymbol{q})$ is independent of the direction of $\boldsymbol{q}$, i.e., $C(\boldsymbol{q}) = C(q)$, and the 2D PSD $C(q_x, q_y)$ is independent of the wave propagation vector's direction, and can be converted into the 1D $C(|\boldsymbol{q}|)$, while still carrying the power of the height profile of the square area [71],

$$q_L^2 \sum_{m_x=0}^{N/2} \sum_{m_y=0}^{N/2} \bar{C}(m_x, m_y) = 2\pi q_L^2 \sum_{m=1}^{N/2} mC(m) \tag{3-20}$$

where,

$$\bar{C}(m_x, m_y) = C(m_x, m_y) + C(N - m_x, m_y) + C(m_x, N - m_y) + C(N - m_x, N - m_y) \tag{3-21}$$

Equation (3-21) is obeyed if we define the angular average as,

$$C(m) = \frac{1}{2\pi m} \sum_{-\frac{1}{2} < |m'| - m < \frac{1}{2}} \bar{C}(m_x', m_y') \tag{3-22}$$

With this definition, the 'sum rule' will be obeyed,

$$\langle h^2 \rangle = 2\pi \int dq\, q\, C(q) = 2\pi q_L^2 \sum_{m=1}^{N/2} mC(m) \tag{3-23}$$

3.2.1.1 2D power spectrum of measured profiles

We consider randomly rough surfaces where the statistical properties are transitionally invariant, but not necessarily isotropic. In this case, complete information about the statistical properties of the surface is in general only obtained by measuring the height profile over a square (or rectangular) surface area, i.e., a single line scan does, in general, not contain the full information about the statistical properties of the surface. In particular, the 2D power spectrum cannot be obtained from the 1D power spectrum. However, for the limiting cases of 1) isotropic surface roughness [72], and 2) 1D surface roughness [73], the 2D power spectrum can be obtained from the 1D power spectrum. Isotropic surface roughness may prevail for, e.g., surfaces prepared by sand blasting, while 1D surface roughness may result from polishing, if the

direction of polishing is fixed. Since some experimental techniques measure the surface topography only along line scans rather than over rectangular surface areas, it is important to be able to calculate the 2D power spectrum from 1D profile measurements. For the two limiting cases discussed above, this can be done as follows:

3.2.1.1.1 Isotropic Roughness

In this case, the 2D power spectrum will only depend on the magnitude q of the wave vector $\boldsymbol{q}$ [74]. After converting to the polar coordinates in the x-plane and performing the C_{2D} integral over z by summing up the contributions from the poles located inside the unit circle in the complex z-plane, C_{2D} can be obtained from 1D line scans of the surface topography by using the Inverse Abel transform [75] [76]:

$$C_{2D}(q) = \frac{1}{\pi} \int_{q}^{\infty} dq' \frac{[-C'_{1D}(q')]}{(q'^2 - q^2)^{1/2}} \tag{3-24}$$

3.2.1.1.2 Unidirectional roughness

If we choose the y-axis along the direction where $h(\boldsymbol{x})$ is constant, we get $h(\boldsymbol{x}) = h(x, 0)$, and,

$$C_{2D}(\boldsymbol{q}) = \frac{1}{2\pi} \int dx \, \langle h(x,0)h(0,0)\rangle \, e^{-iq_x x} \times \frac{1}{2\pi} \int dy \, e^{-iq_y y} = C_{1D}(q_x) \, \delta(q_y) \tag{3-25}$$

The angular average of $C_{2D}(\boldsymbol{q})$ only depends on the magnitude q of the wave vector,

$$\bar{C}_{2D}(q) = \frac{1}{2\pi} \int_0^{2\pi} d\phi \, C_{2D}(\boldsymbol{q}) = \frac{1}{2\pi} \int_0^{2\pi} d\phi \, C_{1D}(qcos\phi) \, \delta(qsin\phi) = \frac{C_{1D}(q)}{\pi q} \tag{3-26}$$

where $\delta(qsin\phi) = \frac{[\delta(\phi)+\delta(\phi-\pi)]}{q}$.

3.2.1.2 Texture measurement resolution and evaluation length

The upper cut-off distance $1/q_0$ for asphalt is typically about $4mm - 1\,cm$, which is the dimension of the typical grain size. L is the linear size of the tread block used in measurements $\approx 1cm$ (with slip of the order of $5 - 10\%$, and typical footprint length of the order of $10 - 15\,cm$). L is also mentioned to be the diameter of macroscopic contact area. q_L is the smallest relevant wavevector, and rubber friction is very insensitive to the exact value of q_L. If $L = 1cm$, for spectral analysis we need an evaluation length of $2\,cm$. The shortest possible cut-off distance q_1 is the atomic distance. In practice, cut-off occurs at a much larger length scale, because of contamination, trapped fluid, or trapped pockets of compressed air, or if the rubber has a modified thin surface skin that might act as a cut-off length. If the road is covered by small particles, e.g., dust or sand particles, with typical diameter D, then one may expect $q_1 \approx 1/D$. Similarly on a wet road, the water trapped in surface cavities may act as an effective short distance cut-off. However, for clean dry road surfaces, q_1 may be determined by the rubber compound properties (Layer of modified rubber at the surface $\approx 1 - 10\,\mu m$). In rubber friction on smooth surfaces, the more likely cut-off length which is the mean distance between rubber cross-links, is in the order of a few nanometers.

The thermal and stress-induced degradation results in a thin layer of modified rubber at the surface, that can be estimated from scanning electron microscopy pictures of the surface region of a car tire tread block. We make the basic assumption that the deformation of the rubber on length scales shorter than the thickness of the modified layer gives a negligible contribution to tire-road friction. Thus, the modified surface layer acts as a dead layer [77]. Friction would be overestimated if ones takes length scales shorter than this layer's thickness into account for $C(q)$ in the estimation of μ. As for the measurements of the profiles, we can always measure with smaller resolution and then filter if needed. The formation of the

layer requires some run-in time period (a freshly prepared rubber surface exhibits higher μ). Analytically, the thickness of this layer can be roughly estimated by iterations of Equation (3-27) [77],

$$\frac{\Delta E\left(1-\frac{\sigma}{\sigma_c}\right)}{k_B T} = \ln\left(\frac{\omega_0}{\omega}\right) \approx 28 \tag{3-27}$$

where ΔE is the activation energy for bond breaking, σ_c is the stress necessary for bond breaking at zero temperature, T is temperature, σ is the tensile stress, ω_0 is the attempt frequency, ω is the rate of bond breaking, and k_B is the Boltzmann constant.

In [78], good agreement between the simulation results and the experimental data is achieved for different rubber compounds and rough surfaces, when the short-distance cut-off wavevector is selected such that the rms-slope equals 1.3. In the common practice in industry, the short-distance cut-off is estimated by fitting friction coefficient estimations to measured friction data.

3.2.2 Klüppel's method

Instead of spatial frequency, Klüppel works in temporal frequency domain (rad/s). Therefore, the frequency depends on velocity too. It changes $\log(S(\omega)) - \log(\omega)$, but doesn't change the fractal dimension D. Also, having the frequency in rad/s or Hz, and also dividing the Fourier transform by the number of samples N or $\sqrt{N}$ doesn't affect the slope.

To verify the FFT algorithm, Fourier series and Inverse Fourier Transform were used:

Fourier series: $s_N(x) = \sum_{n=1}^{N} a_n \cos\left(\frac{2\pi n x}{p}\right) + b_n \sin\left(\frac{2\pi n x}{p}\right) = \sum_{n=-N}^{N} c_n\, e^{i\frac{2\pi n x}{p}}$

$a_n = \frac{2}{p}\int_{x_0}^{x_0+p} s(x)\cos(\frac{2\pi n x}{p})dx$

$$b_n = \frac{2}{p}\int_{x_0}^{x_0+p} s(x)\sin\left(A\frac{2\pi nx}{p}\right)dx$$

$$c_n = \frac{1}{p}\int_{x_0}^{x_0+p} s(x)\mathrm{e}^{-\mathrm{i}\frac{2\pi nx}{p}}dx = = \begin{cases}\frac{1}{2}(a_n - ib_n) & n > 0\\ c_{|n|}^{*} & n < 0\end{cases}$$

$$iFFT \rightarrow \ \ s(x) = \sum_{-\infty}^{+\infty}|s|\, e^{i\phi}\, e^{i\frac{2\pi nx}{p}} = \sum\ \ |s|\, e^{i\left(\frac{2\pi nx}{p}+\phi\right)}$$

$$\phi = \frac{Im(|s|)}{Re(|s|)}$$

$$e^{i\left(\frac{2\pi nx}{p}+\phi\right)} = \cos\left(\frac{2\pi nx}{p}+\phi\right) + i\,\sin(\frac{2\pi nx}{p}+\phi)$$

$$\Rightarrow c_n = |s|\, e^{i\phi} = |s|\,(cos\phi + i\, sin\phi) = \frac{1}{2}(a_n - ib_n)$$

Where $a_n = 2|s|cos\phi$ and $b_n = 2|s|sin\phi$

$$\Rightarrow s_N(x) = 2\sum_{n=1}^{N}|s|\, cos\phi\cos\left(\frac{2\pi nx}{p}\right) - |s|\, sin\phi\sin\left(\frac{2\pi nx}{p}\right) = 2\ \sum_{n=1}^{N}|s|\cos\left(\frac{2\pi nx}{p}+\phi\right)$$

3.2.2.1 Height Difference Correlation Function and Power Spectral Density

If the profile $z(x)$ of a rough surface is considered, the surface is self-affine if the transformation $x \rightarrow \alpha x, z \rightarrow \alpha^H z$ leaves the surface statically invariant. The exponent H is called the Hurst exponent. It can be obtained by different methods, such as the box counting method [16] [79] [80]:

$$D = 3 - H \tag{3-28}$$

In addition to the surface fractal dimension D, two further length scales are necessary to characterize a self-affine surface: 1) the correlation length $\xi_{||}$ parallel to the surface, and 2) the variance $\tilde{\sigma}$, i.e., the root mean square fluctuations around the mean height:

$$\tilde{\sigma}^2 = \langle (z(x) - \langle z \rangle)^2 \rangle \tag{3-29}$$

Here $\langle z \rangle$ is the mean height of the surface points and $\langle \dots \rangle$ is the average over the set of observations of surface topography. The variance $\tilde{\sigma}$ can also be expressed by the correlation length $\xi_\perp$ normal to the surface ($\tilde{\sigma}^2 = \frac{1}{2}\xi_\perp^2$). The height difference correlation function, $C_z(\lambda)$, calculates the mean square height fluctuations of the surface with respect to the horizontal length scale λ, and is given by:

$$C_z(\lambda) = \langle (z(x+\lambda) - \langle z(x) \rangle)^2 \rangle \tag{3-30}$$

For large length scales, $C_z(\lambda)$, plateaus-off at a value of $\xi_\perp$. The largest horizontal asperity is of dimension $\xi_{||}$.

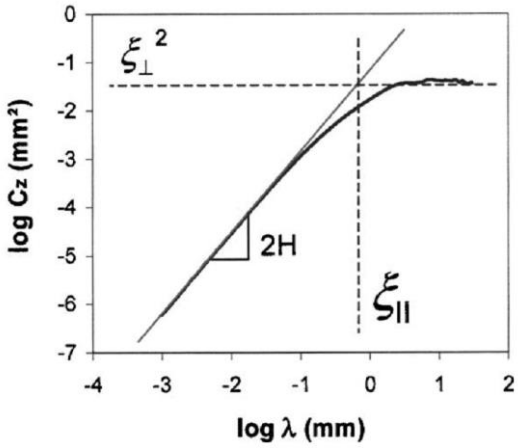

Figure 3-7. The height difference correlation function with respect to wavelength; ; *Reproduced from [81] with permission from AIP.*

If there is one distinct region (one straight slope on the $\log(C_z(\lambda))$ versus $\log(\lambda)$ curve), the resulting height difference correlation function is:

$$C_z(\lambda) = \left(\frac{\lambda}{\xi_{||}}\right)^{2H} \xi_{\perp}^2 \qquad \text{for } \lambda < \xi_{||} \tag{3-31}$$

Equation (3-31) can be derived from the line $y = mx + b$, and plugging in the values shown in Figure 3-7.

But one single region does not always describe the surface well. The $\log(C_z(\lambda))$ versus $\log(\lambda)$ curve can be approximated as having two distinct regions, each of which can be described by self-similar geometry within itself. For this type of surface, the height difference correlation function is:

$$C_z(\lambda) = \xi_{\perp}^2 \left(\frac{\lambda}{\lambda_2}\right)^{2H_2} \left(\frac{\lambda_2}{\xi_{||}}\right)^{2H_1} \qquad \text{for } \lambda < \lambda_2 \tag{3-32}$$

For the macrotexture, the power spectrum density (in frequency space) is:

$$\begin{aligned} S_1(\omega) &= S_{0,1} \left(\frac{\omega}{\omega_{min}}\right)^{-(7-2D_1)} \\ S_{0,1} &= \frac{(3-D_1)\xi_{\perp}^2}{2\pi v \xi_{||}} \end{aligned} \tag{3-33}$$

for $\omega_{min} < \omega < \omega_2$,

$$\omega_{min} = \frac{2\pi v}{\xi_{||}} \quad \text{and} \quad \omega_2 = \frac{2\pi v}{\lambda_2}$$

The relations for the microtexture are:

$$\begin{aligned} S_2(\omega) &= S_{0,2} \left(\frac{\omega}{\omega_c}\right)^{-(7-2D_2)} \\ S_{0,2} &= \frac{(3-D_1)\xi_{\perp}^2}{2\pi v \xi_{||}} \left(\frac{\omega_{min}}{\omega_c}\right)^{(7-2D_1)} \end{aligned} \tag{3-34}$$

An alternative approach to the fractal analysis of rough surfaces considers the height correlation function $\Gamma_z(\lambda)$ that is also termed auto-correlation function:

$$\Gamma_z(\lambda) = \langle z(x+\lambda)z(x)\rangle - \langle z(x)\rangle^2 \quad (3\text{-}35)$$

This function characterizes the correlation of heights at two different positions. For stationary surfaces the Fourier transform of $\Gamma_z(\lambda)$ equals the spectral power density $S(f)$, where f is the spatial frequency (Wiener-Khinchin theorem) [82]:

$$\Gamma_z(\lambda) = \int_{f_{min}}^{\infty} S(f) e^{2\pi i f \lambda} df \quad (3\text{-}36)$$

The minimum frequency f_{min} corresponds to the inverse correlation length $\xi_{||}$ and represents the maximum wavelength of the modulations of the surface.

3.2.3 Rado's technique

Rado [1] used the product of the Fourier transform of the signal and the complex conjugate of the Fourier transform. The following proof shows that it should give the same results as when getting the Fourier transform of the autocorrelation of the signal.

Autocorrelation: $R_{xx}(k) = \frac{1}{2N}\sum_{n=-N}^{N} x_n\, x_{n-k}$

Auto Power Spectrum (Fourier Transform of Autocorrelation):

$Power\ Spectral\ Density \rightarrow S_{xx}(f) = \int_{-\infty}^{\infty} R_{xx}(t)\, e^{-j2\pi f t} dt$

$S_{xx}(f) = X^*(f)\, X(f) = |X(f)|^2$

Time Convolution: $F\left(\int_{-\infty}^{+\infty} x_1(\tau) x_2(t-\tau)\right) = X_1(f)\, X_2(f)$

Frequency Convolution: $F\left(x_1(t)x_2(t)\right) = X_1^*(f)\, X_2(f)$

The Auto Power Spectrum (Klüppel) is equivalent to the product of the Fourier Transform of the signal and its Complex Conjugate (Rado).

3.3 Profile classification parameters

The objective of the work presented in this section is to discover parameters, extracted from pavement measurements, that can characterize road surfaces, i.e., classify road surfaces based on their coefficients of friction. The outcome is a useful tool to predict the friction of different road surfaces in certain environmental conditions, using only profile measurements. It is to be noted that the role of tire tread compound is not considered here, and it is assumed that the same tire that was used for the original field tests is in contact with the different road surfaces.

Michigan Tech Transportation Institute in collaboration with Michigan Department of Transportation (MDOT) began a joint investigation into the properties that influence pavement friction. This multi-phase research project, which began in the mid 1990s, set out to establish a definitive relationship between field and laboratory friction values and specific pavement characteristics. Initially, thirty pavement test sites within the state of Michigan were identified. The locations selected included a variety of road types, ranging from two-lane rural roads to six-lane urban highways, mix designs, and pavement ages. At each site, using the MDOT single axle friction trailer, locked wheel tests were performed in accordance with ASTM E274 at an average speed of 40 mph. A nozzle dispensed water in front of the tire to simulate wet conditions. Strain gauges on the wheel axle measured the amount of torque on the locked wheel and were then used to calculate the Friction Number (FN). The road profiles were measured using an OGP (Optical Gaging Products, Incorporated) Digital Range Sensor System DRS-8000, with a lateral resolution

of 45 μm (Figure **3-8**). The FN values are site values before the pavement is cored for profile measurement [45] [83]. Each core was taken from a spot on the road within the length where FN was recorded. In the present work, the data from the five road surface profiles (out of the thirty that have been measured) that were available to us are studied:

1. 14d1 (4-lane suburban), $FN = 42$
2. 15d1 (4-lane suburban), $FN = 46$
3. 26d1 (6 lane city highway), $FN = 35$
4. 29d1 (4 lane rural highway), $FN = 55$
5. 30b1 (4 lane rural highway), $FN = 76$

Figure 3-8. OGP Digital Range Sensor System DRS-8000

Twelve 46 mm long traverse lines were measured parallel to traffic directions evenly distributed across each surface (Figure 3-9).

Spectral analysis techniques such as the fast Fourier transform (FFT) are commonly adopted to analyze pavement profiles because their statistical characteristics resemble those of random signals [84] [85]. If

$z(x)$ is the surface profile height expressed as a function of longitudinal distance x, the corresponding finite-length Fourier transform can be written as [86],

$$Z(k) = \int_0^L z(x)e^{-ikx}dx \tag{3-37}$$

where $k = 2\pi f_m$ and f_m is the spatial frequency components of the surface roughness. To obtain a power spectral density profile curve useful for mathematical calculations, one needs to do slope and offset suppression that can be accomplished by subtracting a least square fit from the profile [69]. The Discrete Fourier Transform is based on the assumption that the input signal repeats itself with a period equal to signal duration. At the edges of the signal, there might be a jump in the composite signal. This effect is known as leakage that affects the spectrum obtained. To prevent leakage, a Split Cosine Bell Window (SCBW) is applied which reduces the signal to zero at the edges.

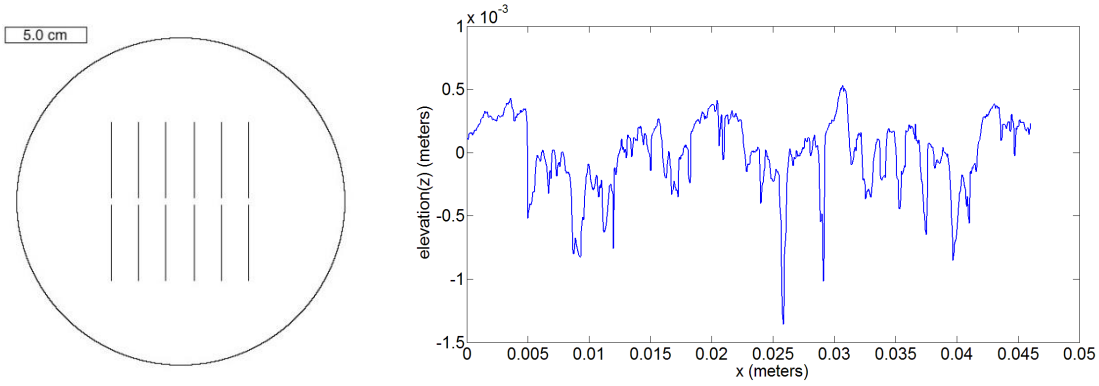

Figure 3-9. Left: Layout of traverse lines for measured profiles. Right: The elevation profile for one traverse line.

The mean square roughness β^2 is,

$$\beta^2 = \frac{1}{N}\sum_{n=0}^{N-1} z^2(n) \tag{3-38}$$

where N is the number of values of $z(x)$ measured at equally spaced intervals Δx over a total length of $L(= N\Delta x)$. The highest surface spatial frequency resolved in the measurement process, which is the Nyquist frequency, is $f_c = (2\Delta x)^{-1}$. Hence, it can be seen that the measurement interval Δx limits the bandwidth of frequencies.

Furthermore, one can integrate the PSD over the Nyquist bandwidth limits of surface spatial frequency to obtain the area under the PSD curve. Parseval's theorem [87] states that this area is equal to the mean square roughness of the pavement. Therefore it can be seen that the PSD plot of a surface profile can be employed to describe both frequency and roughness characteristics in terms of the spatial frequencies and the area under the plot, respectively. The Fast Fourier Transform of one traverse line from the surface 29d1 is plotted in Figure 3-10. Actual roads do not tend to have such regular deformations with very specific wavelength peaks appearing in the spectrum.

Another approach applied for characterization is the so-called Indenters method. The idea is, in the contact area between road and tire, contact is not established at every point of the road surface because the road surface is rough. Profile analysis related to friction should then take into account only the useful parts of the profile, i.e., those in contact with the tire. Very few of the previous studies have dealt with this concept [88]. The angular parameter θ is derived from the curve connecting profile peaks (Figure 3-11). Actually, the angles between every segment that connects two consecutive peaks and the horizontal are calculated. Peaks are simply defined as those composed of three consecutive points, the height of the middle point being the maximum. An indenter is defined as the triangle formed by a peak and two adjacent valleys. The shape of the indenter is characterized by the cotangent of the half angle (α) at the top. This method enables us to extract significant profile features and eliminate insignificant features.

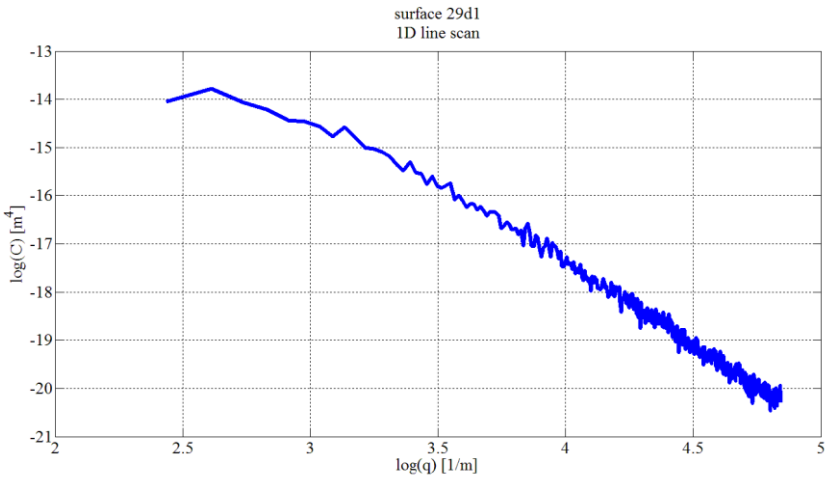

Figure 3-10. Fast Fourier transform of one traverse line from 29d1. The x and y axes represent the log of spatial frequency and the log of two dimensional power spectrum, respectively.

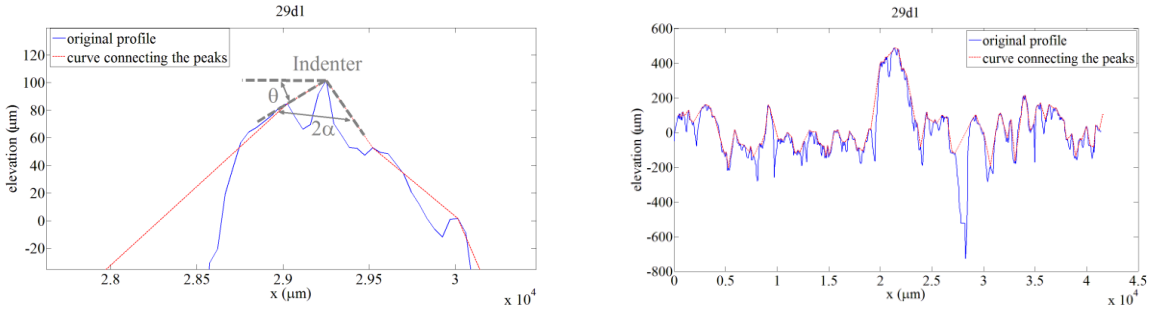

Figure 3-11. Left: The Indenters method. Right: The original profile of one traverse line from 29d1, together with the curve connecting the peaks.

A classical global fractal parameter is the Correlation Exponent. This exponent measures the speed of decay of the autocorrelation of a signal (the cross-correlation of a signal with itself). Fractional dimensions are one of the best known parts of fractal analysis. In this research, Regularization Dimension ($DimR$) is a global parameter that is dealt with. $DimR$ measures the speed of convergence of the finite length of the convolution of the signal with a Gaussian kernel of variance $s > 0$, to infinity, when s tends

to 0. The general idea is to define a fractal index for irregular functions based on the behavior of the lengths of less and less regularized versions of their graphs. The regularized versions are obtained by convoluting the function with a smooth kernel dilated by a scale parameter. A "fractal" graph will typically exhibit a power law for the regularized lengths as a function of s, with exponent $-d$. In this case, the regularization dimension is defined to be $1 + d$. It coincides in many cases with the box dimension.

Instruments with different resolutions and scan lengths provide different values of statistical parameters for the same surface. Therefore, it is very important to characterize rough surfaces by intrinsic parameters, which are independent of the sampling length or area. Holder Exponent, which indicates the scale of perturbation of surface topography, reflects an intrinsic property of random phenomena. Let $x_0 \in \mathbb{R}$ and s be a real number with $s > -1$. A function $f: \mathbb{R} \to \mathbb{R}$ belongs to global Holder space $C^s_{x_0}$ if and only if there exists a constant C and a polynomial P of degree at most "s" such that,

$$|f(x) - P(x - x_0)| \leq C|x - x_0|^s \tag{3-39}$$

The Pointwise Holder Exponent of f at x_0 denoted by $\alpha_f(x_0)$ or simply α, is defined to be $\sup [s: f \in C^s_{x_0}]$. By varying α, Holder Exponent characterizes the transition from a non-continuous to a smooth differentiable function. Thus, it can be considered as an indicator of roughness. Holder exponent is a measure of local behavior, because it is measured at each point. Since friction is mainly a local phenomenon, it might be correlated with local regularity measures.

3.4 Viscoelastic modulus of tread compounds

3.4.1 Time-temperature superposition

The time–temperature superposition principle is a concept in polymer physics and in the physics of glass-forming liquids [89] [90]. This superposition principle is used to determine temperature-dependent mechanical properties of linear viscoelastic materials from known properties at a reference temperature. Curves of the instantaneous modulus as a function of time do not change shape as the temperature is changed but appear only to shift left or right (see Figure 3-12). This implies that a master curve at a given temperature can be used as the reference to predict curves at various temperatures by applying a shift operation. The time-temperature superposition principle of linear viscoelasticity is based on the above observation [91].

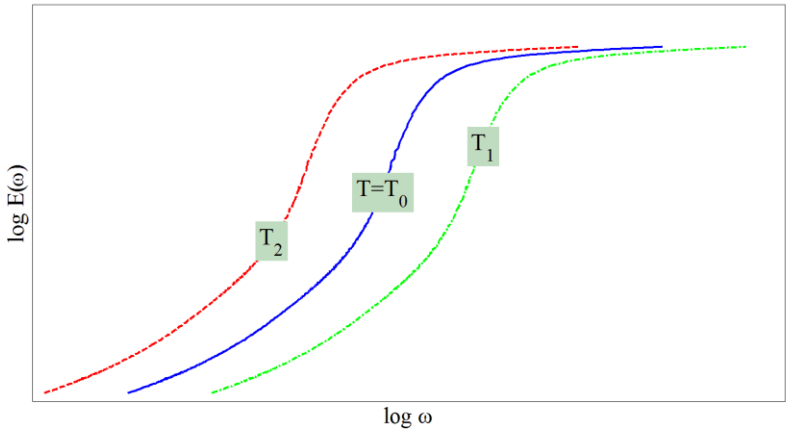

Figure 3-12. Temperature dependence of complex elastic modulus of a viscoelastic material under periodic excitation. ω is frequency, E is the complex modulus, and $T_2 < T_0 < T_1$.

The application of the principle involves the following steps:

- Experimental determination of frequency-dependent curves of isothermal viscoelastic mechanical properties at several temperatures and for a small range of frequencies.
- Computation of the shift factor to correlate these properties for the temperature and frequency range.
- Experimental determination of a master curve showing the effect of frequency for a wide range of frequencies
- Application of the shift factor to determine temperature-dependent moduli over the whole range of frequencies in the master curve.

The shift factor is often computed using an empirical relation first established by Malcolm L. Williams, Robert F. Landel and John D. Ferry (also called the Williams-Landel-Ferry or WLF model) [91]. An alternative model suggested by Arrhenius is also used [92]. The WLF model is related to macroscopic motion of the bulk material, while the Arrhenius model considers local motion of polymer chains.

3.5 Contact mechanics

A thorough, physics-based friction model could be a tool that can facilitate better predictions. The model should take account of rubber's thermo-mechanical properties, take in mathematical description of the road, account for ambient conditions, and possibly include flash heating. The Persson contact model, the Klüppel friction theory, and the inclusive friction model developed in this study are explained in this section.

3.5.1 Persson's theory

The main contribution to rubber friction when a rubber block slides on a rough substrate, such as in the case of a tire on a road surface, is due to the viscoelastic energy dissipation in the surface region of the rubber as a result of the pulsating forces acting on the rubber surface from the substrate asperities. This energy dissipation process is accurately described, and the velocity dependence (and, in a more general case, the time history dependence) of the rubber friction coefficient is predicted [11] [12]. The results depend only on the complex viscoelastic modulus $E(\omega)$ of the rubber, and on the substrate surface roughness power spectrum $C(q)$. Neglecting the flash temperature effect (the term flash temperature refers to a local and sharp temperature rise occurring in the tire–road asperity contact regions during slip), the kinetic friction coefficient at velocity v is determined by,

$$\mu_k = \frac{1}{2} \int_{q_0}^{q_1} dq\, q^3\, C(q)\, P(q) \int_0^{2\pi} d\phi\, cos\phi\, Im \frac{E(qvcos\phi)}{(1-\nu^2)\sigma} \tag{3-40}$$

where,

$$P(q) = \text{erf}(\frac{1}{2\sqrt{G}}) \tag{3-41}$$

and,

$$G(q) = \frac{1}{8} \int_{q_0}^{q} dq\, q^3\, C(q) \int_0^{2\pi} d\phi \left| \frac{E(qvcos\phi)}{(1-\nu^2)\sigma} \right|^2 \tag{3-42}$$

where σ is the mean perpendicular pressure (the load divided by the nominal contact area), and ν is the Poisson ratio which is close to 0.5 for rubber-like materials. ν depends on frequency, but for $\nu = 0.5$ (rubbery region) to $\nu = 0.4$ (glassy region), $\frac{1}{1-\nu^2}$ varies from 1.33 to 1.19, and we can neglect the weak dependence on frequency. Therefore, we take $\nu = 0.45 \rightarrow E = 2\, G\, (1.45) = 2.9\, G$.

The simplified equation of coefficient of friction for fractal surfaces is,

$$\mu \approx \frac{1}{4\pi}(q_0 h_0)^2 H \int_1^{\frac{q_1}{q_0}} d\xi\, \xi^{-2H+1}\, P(q_0\xi) \times \int d\phi \cos\phi\, Im \frac{E(\xi q_0 v cos\phi)}{(1-\nu^2)\sigma_0} \quad (3\text{-}43)$$

The theory takes into account the substrate roughness in the range $q_0 < q < q_1$, where q_0 is the smallest relevant wavevector of order $2\pi/L$, where (in the case of a tire) L is the lateral size of a tread block, and where q_1 may have different origins. Since q_0 for a tire tread block is smaller than the roll-off wavevector q_0 of the power spectra of most road surfaces, rubber friction is very insensitive to the exact value of q_0. The large wavevector cut-off q_1 may be related to road contamination, or may be an intrinsic property of the tire rubber. For example, if the road surface is covered by small contamination particles (diameter D), then $q_1 \approx 2\pi/D$. In this case, the physical picture is that when the tire rubber surface is covered by hard particles of linear size D, the rubber will not be able to penetrate into surface roughness 'cavities' with diameter (or wavelength) smaller than D, and such short range roughness will therefore not contribute to the rubber friction. For perfectly clean road surfaces we believe instead that the cut-off q_1 is related to the tire rubber properties. Thus, the high local (flash) temperatures during braking, and the high local stresses which occur in the tire rubber–road asperity contact regions, may result in a thin (typically of order a few micrometers) surface layer of rubber with modified properties (a dead layer), which would contribute very little to the observed rubber friction. Since the stresses and temperatures which develop in the asperity contact regions depend somewhat on the type of road (via the surface roughness power spectrum $C(q)$), the thickness of this dead layer may vary from one road surface to another, and some run-in time period will be necessary for a new dead layer to form when a car switches from one road surface to another. Such run-in effects are well known experimentally.

3.5.1.1 Flash temperature effect

The energy dissipation will result in local heating of the rubber. Since the viscoelastic properties of rubber-like materials are extremely strongly temperature dependent, it is necessary to include the local

temperature increase in the analysis. At very low sliding velocities the temperature increase is negligible because of heat diffusion. But for velocities of order $10^{-2}\ m/s$ and higher, the local heating may be very important.

The temperature increase usually results in a decrease in rubber friction with increasing sliding velocity. To estimate the coefficient of friction with flash temperature, one first needs to calculate the flash temperature by iteration (Equations (3-44), (3-45) and (3-46)). Then the viscoelastic modulus at that temperature needs to be computed and horizontal shifts performed. The last step is to calculate friction at the shifted modulus.

$$T_q = T_0 + \int_0^\infty dq'\ g(q,q')\ f(q') \tag{3-44}$$

$$g(q,q') = \frac{1}{\pi}\int_0^\infty dk\,\frac{1}{Dk^2}\left(1 - e^{-Dk^2 t_0}\right)\frac{4q'}{k^2+4q'^2}\,\frac{4q^2}{k^2+4q^2} \tag{3-45}$$

$$f(q) = \frac{vq^4}{\rho C_V}\ C(q)\ \frac{P(q)}{P(q_m)}\int d\phi\ cos\phi\ Im\frac{E(qvcos\phi,T_q)}{1-\nu^2} \tag{3-46}$$

where $\xi_m = 2 \sim 5$ is the magnification for which the macro-asperity contact regions typically appear, $q_m = q_0.\xi_m$, and R (average radius of a macro-asperity contact area) is estimated as $R = \frac{3}{2}\frac{1}{q_0}$. $P(q_m) = A/A0 = 0.25\text{–}0.3$.

Time-Temperature Superposition is used to determine temp-dependent mechanical properties of linear viscoelastic materials from known properties at a reference temperature. The WLF equation is an empirical equation associated with time-temperature superposition,

$$E(\omega, T) = E(\frac{\omega a_T}{a_{T_0}}, T_0)$$

$$\log(a_T) = -\frac{C_1(T-T_0)}{C_2+(T-T_0)} \quad (3\text{-}47)$$

where T is temperature, T_0 is a reference temperature chosen to construct the master curve, and C_1 and C_2 are the empirical constants adjusted to fit the values of the superposition parameter a_T.

According to Page 223 of [93]:

$$T > T_0 \rightarrow a_T < 1$$

$$T < T_0 \rightarrow a_T > 1$$

Going from T_0 to T, the horizontal displacement of $-\log a_T$ should be applied. Master curves obtained by horizontal only shifting are not ideal for filled compounds. We essentially would also have to do a vertical shift, when there's more than one relaxation mechanism. Having a vertical shift is better, but possibly still not ideal. In spite of this non-ideality, master curves, even with horizontal only shifting, are broadly used for filled rubber.

3.5.2 Klüppel's theory

The hysteresis friction interval is split into two integrals, one over each length scale region [94]:

$$\mu_H = \frac{F_H}{F_N} = \frac{1}{2}\frac{\langle\delta\rangle}{\sigma_0 v}\left\{\int_{\omega_{min}}^{\omega_2} d\omega\ \omega\ E''(\omega)\ S_1(\omega)\ +\ \int_{\omega_2}^{\omega_{max}} d\omega\ \omega\ E''(\omega)\ S_2(\omega)\right\} \quad (3\text{-}48)$$

where $\omega_2 = \frac{2\pi v}{\lambda_2}$ is determined by the wavelength of the road that marks the boundary between the two scaling regimes. Therefore, the first integral corresponds to macrotexture, and the second to microtexture.

A gradual increasing deviation in the statistical height difference correlation function can usually be detected at around $\lambda \approx 200\mu m$).

The front factor in the friction coefficient equation involves the nominal contact stress, σ_0, and the excited layer thickness, $\langle\delta\rangle$, which is proportional to the mean penetration depth of rubber, $\langle z_p\rangle$. These two contact parameters are governed by the largest length scales, and therefore can be handled by the Greenwood-Williamson theory [95], which is good for may macro situations, but not for micro cases. Therefore, these terms can be taken out of the integrals over the different scaling lengths.

The minimum relevant (contributes to hysteresis friction) wavelength λ_{min} has to be estimated iteratively, within the two scaling regime framework. It is a function of viscoelastic properties and roughness characteristics. A variable λ_{min} administers the diminishing contribution of microtexture as the sliding velocities increases.

In this model, $\langle\delta\rangle$ is the excited layer thickness, which is assumed to be proportional to the mean penetration depth of rubber $\langle z_p\rangle$. The latter term is given by,

$$\langle z_p\rangle = \tilde{\sigma} F_1\left(\frac{d}{\tilde{\sigma}}\right) \tag{3-49}$$

where F_1 is the Greenwood-Williamson function,

$$F_n(t) = \int_l^{\infty} (z-t)^n \phi(z) dz \tag{3-50}$$

with n set to 1.0, and where d is the distance between the rubber and the mean profile height of the substrate (see Figure 3-13).

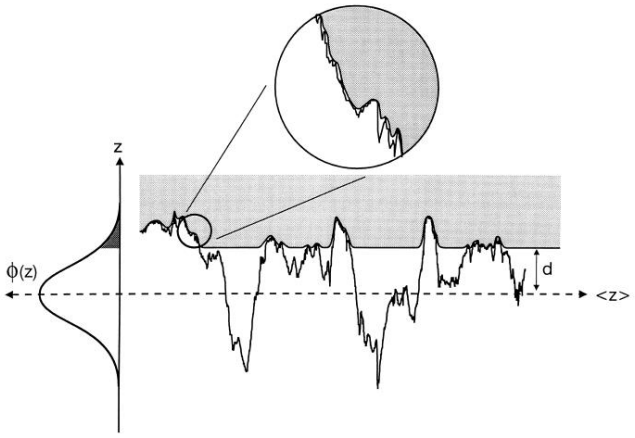

Figure 3-13. Schematic representation of elastic contact between a rubber sample and a rough road track. The distance d between the surfaces, the mean profile- or summit height $\langle z \rangle$ and the profile- or summit distribution function $\phi(z)$, respectively, are indicated. The dark area under the distribution function equals the probability $F_0\left(\frac{d}{\tilde{\sigma}}\right)$ that a summit is in contact with the rubber. The insert shows a magnification of the contact area, demonstrating its composition by individual contact spots.

In the F_1 integral, $t \equiv \frac{d}{\tilde{\sigma}}$ is the normalized distance with respect to the variance of the height distribution, $\phi(z)$. By approximating the expected total normal stress as the product of the weighted stress of a single macroscopic asperity summit according to the Hertz theory [96] and the density of asperity summits on the largest length scale, the mean penetration depth is estimated as,

$$\langle z_p \rangle \approx \frac{\pi \xi_{||}}{E'(\omega_{min})} \sigma_0 \tag{3-51}$$

Thus, the mean penetration depth is proportional to the (apparent) normal stress, and inversely proportional to the low frequency dynamic modulus. The mean penetration depth is governed by macro scale asperities, and is therefore associated with the lowest excitation frequency seen by the rubber.

Using the Greenwood-Williamson functions, the smallest length scale contributing to hysteresis friction with a two scaling ranges approach is given by,

$$\frac{\lambda_{min}}{\xi_{||}} \cong \left(\left(\frac{\lambda_2}{\xi_{||}} \right)^{3(D_2 - D_1)} \frac{0.09\pi s^{\frac{3}{2}} \xi_{\perp} |E(\lambda_{min})| F_0(t) \tilde{n}_s}{\xi_{||} |E(\xi_{||})| F_{3/2}(t_s)} \right)^{\frac{1}{3D_2 - 6}} \tag{3-52}$$

with $\tilde{n}_s = 6\pi\sqrt{3}\lambda_c^2 n_s$, where n_s denotes the summit density. Consequently, the corresponding real area of contact $A_c(\lambda_{mean})$ at a length scale λ_{mean} is given by [82],

$$A_c(\lambda_{mean}) \approx A_0 \left(\frac{\xi_{||} F_0^2(t) F_{3/2}(t_s) |E(\xi_{||})| \tilde{n}_s^2}{808\, \pi\, s^{3/2} \xi_{\perp} |E(\lambda_{min})|} \right)^{\frac{1}{3}} \tag{3-53}$$

3.5.2.1 Adhesion (semi-empirical)

Under dry conditions, both hysteresis and adhesion components contribute to the frictional process. The semi-empirical. equation that can define friction is given in Equation (3-62),

$$\mu = \mu_{Hyst} + \mu_{Adh} \tag{3-54}$$

where $\mu_{Adh} = \frac{F_{Adh}}{F_N} = \frac{\tau_S}{\sigma_0} . \frac{A_c}{A_0}$ and $\tau_S = \tau_{S,0} \left(1 + \frac{\frac{E_\infty}{E_0}}{\left(1 + \left(\frac{v_C}{v}\right)\right)^n} \right)$. F_{Adh} is the contribution to friction force arising from interfacial processes. τ_S is the true interfacial shear strength.

Under wet conditions, the adhesion component of the total friction is drastically reduced, whereas the hysteresis loss remains largely unaffected. Yet, even under wet conditions, statistically distributed islands of dry contact can form. To hinder this mechanism and evade using the semi-empirical adhesion model, Klüppel uses detergents in the experiments, so that the hysteresis friction simulations can be compared to the test results.

3.5.2.2 Mean Penetration Depth

The thickness of the excited layer of rubber is assumed to be proportional to the mean penetration depth. The mean penetration depth is a function of surface roughness, sliding velocity, compound properties and pressure. It cannot be evaluated exactly. In view of an estimation of the excited layer via a quantitative characterization of strain field in the vicinity of the surface asperities, indentation experiments monitored by photogrammetry are performed and validated using finite element simulations.

3.6 The developed comprehensive contact model

Among the physics-based friction prediction models developed to date, an analytical incorporation of the effect of flash heating, as well as a formulation for the contribution from adhesion are exclusive to Persson friction theory. Also, the extension of the friction estimation formulation in the frame of a two-scaling-regimes approach is unique to Klüppel friction theory. Taking these effects into account has led to more accurate predictions [94] [77] [78] [97]. In the present study, the aforementioned theories are used to develop an inclusive multiscale friction model, through a detailed analysis of the key variables of contact mechanics. The model takes into account more factors compared to the current approaches. This is accomplished by recognizing the strengths of each existing method and its advantages over the competitors, and integrating those into a new consolidated model.

The effect of flash temperature was described in section 3.5.1.1. Profile characterization and contact mechanics in the frame of the two-scaling-regimes approach, and the semi-empirical adhesion model within the framework of Persson contact theory are explained in this section.

3.6.1 Profile characterization in two scaling regimes

As discussed in Klüppel's surface characterization approach, one single slope does not always describe a rough surface well. Sometimes, a gradual increasing deviation between the fractal assumption and the statistical power spectrum can be detected for length scales larger than $\approx 200\,\mu m$ [98]. This simply suggests that the scaling properties of macrotexture and microtexture should be described by two distinct regimes [97]. When using the 2D power spectrum to characterize the roughness profile for friction prediction utilizing Persson contact theory, the $\log \mathrm{C}(q) - \log(q)$ curve is approximated as having two different regions (see Figure 3-14), each of which described by self-similar geometry within itself. The formulation of the power spectrum function $C(q)$ can be extended in the frame of a two-scaling-regimes approach.

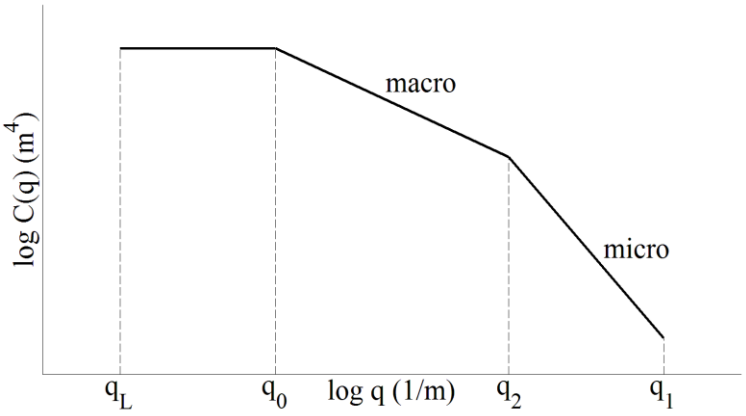

Figure 3-14. Schematic surface roughness power spectrum of a fractal surface with two distinct scaling regions. The slope for $q_0 < q < q_2$ is equal to $2D_{f_1} - 8$ and the slope for $q_2 < q < q_1$ is equal to $2D_{f_2} - 8$. $q_L = 2\pi/L$, where L is the diameter of macroscopic contact area.

The power spectrum of the macrotexture regime is evaluated to be,

$$C_1(q) \approx \left(\frac{h_0}{q_0}\right)^2 \frac{H_1}{2\pi} \left(\frac{q}{q_0}\right)^{-2(H_1+1)} \quad \text{for} \quad q_0 < q < q_2 \tag{3-55}$$

where q_2 is the wavevector corresponding to the intersection point of both scaling regimes, and H_1 is the Hurst exponent of macrotexture. For the microtexture regime,

$$C_2(q) \approx \left(\frac{h_0}{q_0}\right)^2 \frac{H_2}{2\pi} \left(\frac{q_0}{q_2}\right)^{2(H_1+1)} \left(\frac{q}{q_2}\right)^{-2(H_2+1)} \quad \text{for} \quad q > q_2 \tag{3-56}$$

where H_2 represents the Hurst exponent of microtexture. The sandpaper surface under study will be analyzed using both one and two scaling regimes approaches.

3.6.2 Contact mechanics in two scaling regimes

As previously discussed, sometimes the scaling properties of macrotexture and microtexture should be described by two distinct regimes [94]. The kinetic friction coefficient interval is then split into two integrals, one over each length scale regime. The formulation of the kinetic friction coefficient in Equation (3-40) can be extended in the frame of a two-scaling-regimes approach,

$$\mu_k = \frac{1}{2} \left[\int_{q_0}^{q_2} dq\, q^3\, C_1(q)\, P_1(q) + \int_{q_2}^{q_1} dq\, q^3\, C_2(q)\, P_2(q) \right] \int_0^{2\pi} d\phi\, cos\phi\, Im \frac{E(qvcos\phi)}{(1-\nu^2)\sigma} \tag{3-57}$$

The first integral corresponds to macrotexture, and the second to microtexture. For macro- and microtexture, respectively, $P_1(q)$ and $P_2(q)$ are computed by entering $C_1(q)$ and $C_2(q)$ from Equations (3-55) and (3-56) into Equations (3-41) and (3-42).

In the Results section, when estimating the friction of the studied summer tread compound sliding on sandpaper, both one and two scaling regimes are utilized and the outcomes are compared with the indoor experimental data.

3.6.3 Adhesion

When a rubber block is sliding on a rough substrate, the contribution to friction from adhesion in the contact area is dominant at low slip speeds. The adhesive friction coefficient is given by [99],

$$\mu_{adh} = \frac{F_{adh}}{F_0} = \frac{\tau_f(v,T)\, A(\zeta_1)}{\sigma_0\, A(\zeta_0)} \tag{3-58}$$

where F_0 is the normal load, and $\tau_f(v,T)$ is the velocity and temperature dependent frictional shear stress acting in the real contact area $A(\zeta_1) = P(q_1)\, A(\zeta_0)$.

For clean and dry surfaces, the contribution to μ_{adh} is from chemical adhesion (intermolecular forces), dispersive adhesion (van der Waals), interfacial crack propagation [100], interaction of filler particles with the surface asperities, and rubber wear that may be specially significant for slipping on substrates with sharp asperities, such as sandpaper. The bond formation might need some relaxation time, and the friction force approaches zero at very low sliding velocities. At high velocities, there is not enough time for the rubber molecules to adjust to the roughness interaction potential which also leads to small frictional shear stress. Therefore, the shear stress as a function of sliding velocity has a peak at an intermediate velocity [101] [102].

The effective shear stress is not analytically computed by the contact mechanics theory. In [78], τ_f was instead approximated by comparing the measured friction coefficient and the predicted hysteresis contribution according to Equation (3-59),

$$\tau_f = \left(\mu_{exp} - \mu_{hyst}\right) \sigma_0 A(\zeta_0)/A(\zeta_1) \tag{3-59}$$

The hysteresis friction coefficient and the area of real contact were calculated using the Persson contact mechanics theory. Then, the shear stress as a function of sliding velocity was well estimated by a smooth Gaussian master curve,

$$\tau_f = \tau_{f0} \exp\left(-c\left[log\left(\frac{v}{v_0}\right)\right]^2\right) \tag{3-60}$$

where $c = 0.1$, $v_0 = 6 \times 10^{-3}\, m/s$, and $\tau_{f0} = 6.5\, MPa$. The frictional shear stress at different temperatures and sliding velocities can be calculated using,

$$\tau_f(v, T) = \tau_f(a'_T\, v, T_0) \tag{3-61}$$

where a'_T is the shift factor extracted from the master curve in Equation (3-60), and is defined by the Arrhenius factor,

$$\ln a'_T = C'_1\left(\frac{1}{T} - \frac{1}{T_g} + C'_2\right) \tag{3-62}$$

where $C'_1 = 1.1 \times 10^4\, K$, $C'_2 = 8.4 \times 10^{-4}\ K^{-1}$, and T_g is the glass transition temperature. The authors of [78] have discovered that C'_1, C'_2, and τ_{f0} vary slightly for different rubber compounds and rough surfaces. They have suggested that for other compounds, good correlation between theory and experiment can be achieved by using a slightly changed C'_2, or alternatively, a marginally modified T_g.

3.7 Friction measurement

3.7.1 Dynamic rubber friction tester (DRFT)

The Dynamic Friction Test apparatus (see Figure 3-15) provides direct measurement of the horizontal tractive friction force of surface-rubber braking traction and the dynamic vertical load on the test sample. The system is composed of a fake road disk with an arbitrary surface, embedded in a rotating disk, and the tire tread sample embedded in the measuring arm and in contact with the disk. The road disk can be replaced easily. The measuring arm holds the load cell that measures the vertical load and is constrained in longitudinal and axial directions by the longitudinal force measurement mechanism.

The rubber sample and the disk spins at specific speeds to generate arbitrary slip ratios. The rubber sample has a diameter of $8\ cm$ and is $1.5\ cm$ thick. The diameter of the road disk is $30\ cm$. Since the thickness of the road disk and the diameter of the rubber sample are subject to change, a stack of shims will be used to change the height of the disk.

A Kollmorgen AKM44J Servomotor is employed to drive the disk. It is controlled by an AKD-P01206 Servodrive. A Thomson VT010-025-0-RM100-40 (25:1) Gearhead reduces the RPM of the motor and increase the torque to the desired rate. The gearhead is linked to the disk via a Front Driver Passenger CV Axle Shaft 4X4 5Lug Chevy and its Wheel Hub and Bearing Assembly. The rubber sample is driven by a Kollmorgen AKM42H Servomotor, an AKD-P00606 Servodrive, and a Thomson VT075-007-0-RM075-40 (7:1) Gearhead that ensures the same duty as the one used for the disk. The link between the gearhead and the sample is a drive shaft consisting of two McMaster-Carr U-joints and a SDP/SI spline shaft (see Figure 3-16 for CAD model). The parts lists are shown in Figure 3-17. Some sample engineering drawings of some of the parts are presented in Figure 3-18.

By controlling the speed of the rubber sample and the rotating disk at the same time, this equipment makes friction measurements at different slip ratios possible, as well. The system must work smoothly at

different slip ratios. The rubber sample has to be able to follow the profile on the road disk and move up and down as it travels over surface roughness. The normal load has to be maintained properly. Data acquisition and control algorithms are developed for the motors and sensors. That should enable one to control the speed of the motors and get sensible readings from the sensors. In order to validate the spot-on function of the apparatus, a benchmark surface for which the friction vs. slip curve data is available is needed to be used. A control surface with known friction characteristics is also required to calibrate the system on a regular basis.

The wheel speed as well as the turntable speed can be controlled precisely to generate known values of longitudinal slip. With the current system, the maximum reachable linear velocity is $5\,\mathrm{m/s}$. A set of pillow block bearings allow the rubber sample to move up and down in order to follow the profile on the road disk. The vertical load on the rubber sample can be adjusted and controlled precisely using a FSH00257 FUTEK Universal Load cell and a Die Spring preloaded with a nut. The longitudinal force (friction force) can be calculated through reading the torque from Torque-RPM curves of the motors. However, bearings and couplings cause losses and the readings would not be precise. Therefore, the same type of load cell is used to measure the friction force. The dynamic coefficient of friction vs. slip ratio can be calculated through the vertical and horizontal load cells and speed control.

A NI USB-6218 is utilized for data acquisition, where NI LabVIEW serves as the application software. Two FUTEK CSG110 strain gage signal conditioners provide voltage or current excitation to the sensors to generate a voltage output, and optimize the electrical signals generated by the transducers for the input range of the DAQ board. The control parameters are road disk speed, rubber sample speed, vertical load, slip ratio and wheel torque. The data acquisition parameters are friction force, vertical load, road disk speed, rubber sample speed and slip ratio. The drive system for the disk and the rubber sample, as well as the force measurement mechanisms and the control enclosure, housing the AKD drives, the amplifiers, the DAQ system, the fuse boxes and the power supplies, are shown in Figure 3-19.

A Techmor Inc. tire temperature sensor is purchased to record contact patch temperatures (see Figure 3-20 and Table 3-1).

General	
Sensor Type	Infrared
Temperature	
Range	0 to 400 F
Resolution	0.036 F
Accuracy	+/- 0.9 F
Environment	
Operating Temp	-40 to 250 F
Power	
Supply Voltage	5 V
Current	50 mA
Output	
CAN Bus Rate	1 MB/sec
Message Rate	20 Hz

Table 3-1. Techmor Inc. infrared temperature sensor specifications.

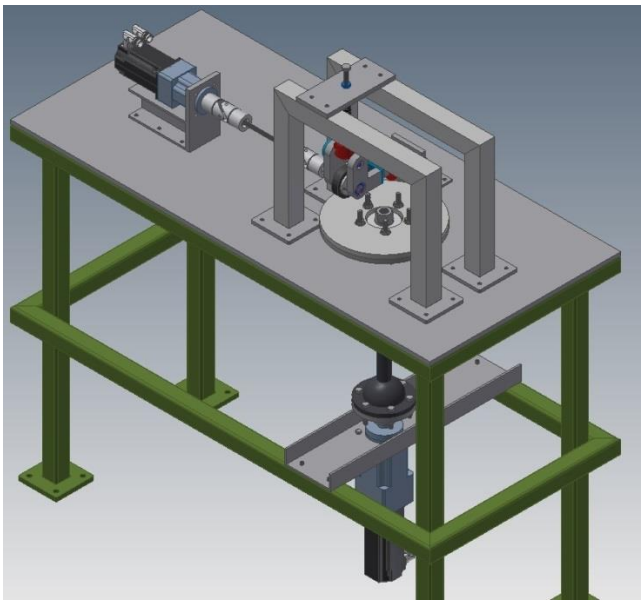

Figure 3-15. Overall view of the Dynamic Friction Test apparatus.

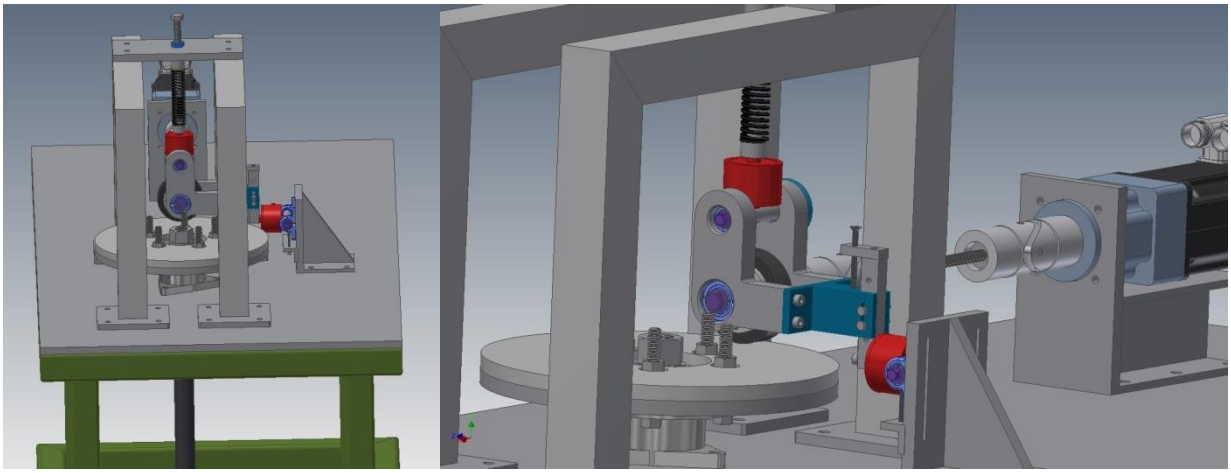

Figure 3-16. The driving and the force measurement modules for the rubber sample.

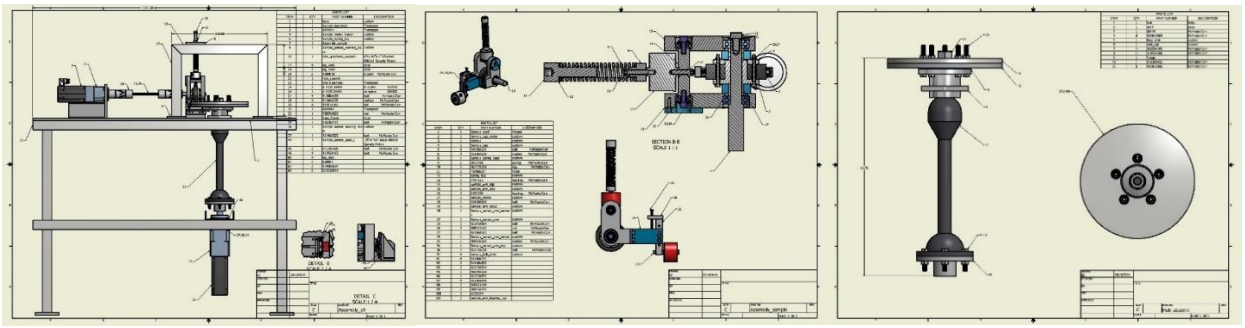

Figure 3-17. Parts lists.

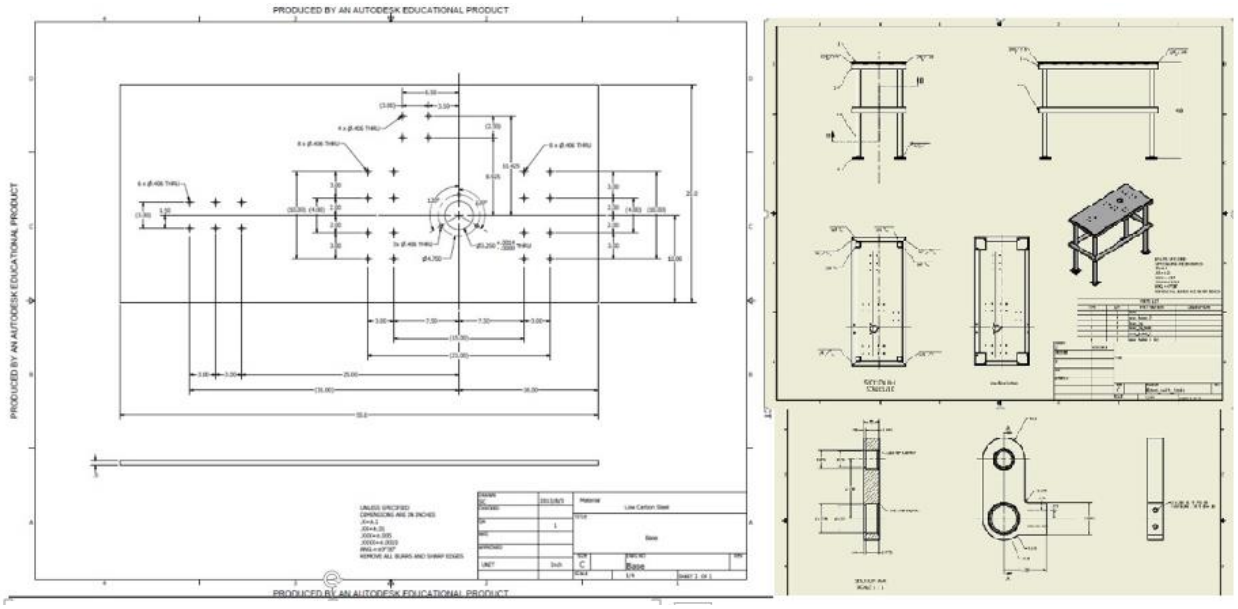

Figure 3-18. Sample engineering drawings.

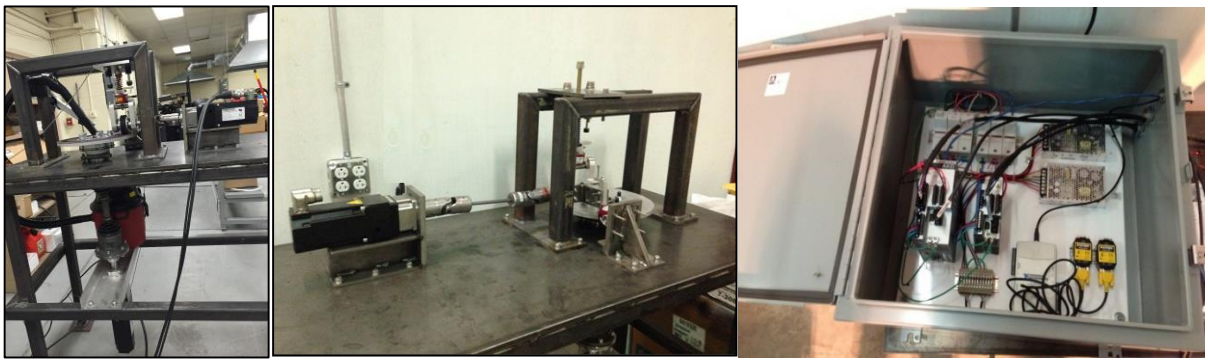

Figure 3-19. Left: Disk's drive system; Middle: Rubber's drive system and force measurement mechanism; Right: Control enclosure housing the AKD drives, the amplifiers, the DAQ system, the fuse boxes and the power supplies.

Figure 3-20. Techmor Inc. infrared temperature sensor.

4 Results

In this chapter, the results of the simulations and experiments, utilizing the methods explained in the previous chapter, are presented. The quantities that are computed and the specifics that are learnt from each section contribute to the development of a comprehensive multiscale rubber-road friction model.

First, the outcomes of using constant percentage bandwidth, height difference correlation function, and power spectral density for profile parameterization are shown. In what follows, the pavement classification results, using only texture-related parameters, are summarized. Then, the reproductions of Persson's and Klüppel's data, in view of the roles of features that are exclusive to each method, are presented. In some cases, comparisons are done between the outcomes of the two models. The strengths of each method are identified and incorporated into a consolidated model that is more comprehensive and proficient than any single existing physics-based approach. The experimental data from the MDOT friction trailer, as well as that of the Dynamic Friction Tester are presented. The correlations between the results of friction estimation simulations (using the existing models, as well as the inclusive model) and the experiments are studied.

4.1 Compound Characterization

The tread compound used in the estimations via the inclusive model and in the indoor experiments is from a summer passenger tire, and has a glass transition temperature of $T_g = -32$ C. A Dynamic Mechanical Analysis test procedure similar to the one presented in [103] is followed. The frequency sweep is performed between 1 Hz and 35 Hz and the temperature sweep is between $-50\ C$ and $120\ C$ in steps of $5\ C$. The horizontal shift factor a_T is selected to give a as smooth as possible master curve for the real modulus [104]. After having determined a_T this way, the same shift function is used to construct the master curve for the imaginary modulus. The resulting master curves at the reference temperature of $T_0 = 20\ C$ are shown in Figure 4-1. The viscoelastic shift factor as a function of temperature is illustrated in Figure 4-2.

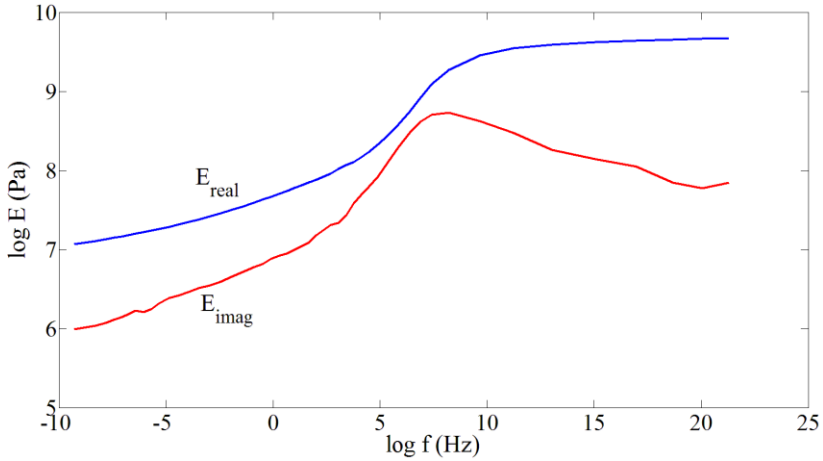

Figure 4-1. The viscoelastic modulus master curves for the summer tire tread compound resulting from shifting the real modulus. The reference temperature is $T_0 = 20\ C$.

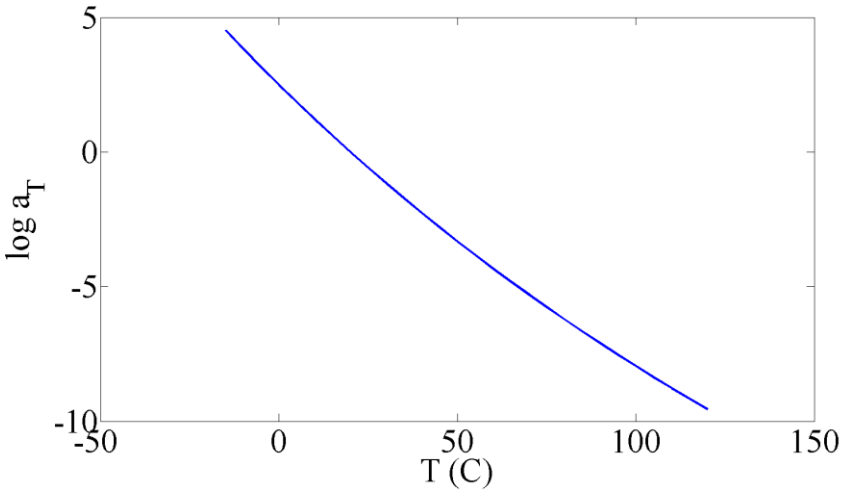

Figure 4-2. The viscoelastic shift factor as a function of temperature for the summer tire tread compound.

4.2 Profile characterization

Nanovea provided us with the area measurements and average particle diameter data of 36, 120 and 220 grit sandpapers. The roll-off wavevector (λ_0) of each profile was estimated by calculating and plotting the power spectra (see Figure 4-3). One can learn from the results that λ_0 is normally ~ 5 times larger than the average particle diameter (Table 4-1).

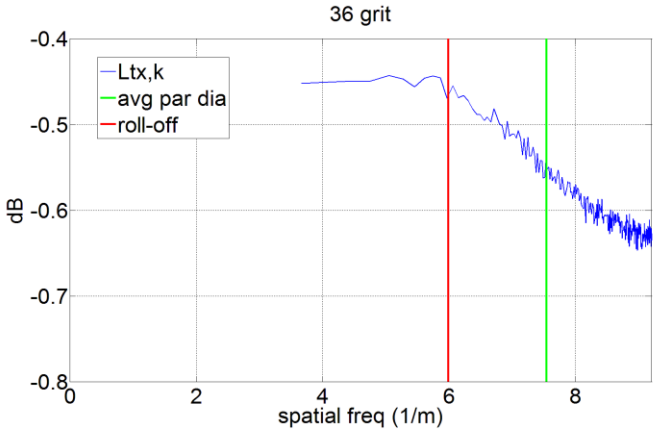

Figure 4-3. Power spectral density of the 36-grit sandpaper.

Sandpaper (Grit)	**Average Particle Dia. (μm)**	**Roll-off Wavelength (μm)**
36	530	2500
120	125	700
220	68	380

Table 4-1. Average particle diameter and roll-off wavelength for three sandpaper profiles.

The roll-off wavevector (λ_0) for some expressway profiles (courtesy of George Dewey, Michigan Tech Transportation Institute) and three gravel profiles (courtesy of Minh Tan Do, IFSTTAR) whose texture is similar to road surfaces were estimated. The results are presented in Table 4-2. The evaluation length needs to be twice the roll-off wavelength (the Nyquist wavelength), in order to process all the frequencies in the spectrum. Based on the results, for most pavements we would need to a measure a minimum of $2-3\ cm$ long profiles.

Profile	Roll-off Wavelength (cm)
4-lane suburban	0.92 – 1.50
6-lane city expressway	2.30
4-lane rural expressway	0.50 – 1.15
Gravels cast into a resin mold and polished	1.13, 1.16, 1.27

Table 4-2. Roll-off wavelength for highway and gravel profiles

To verify the developed characterization algorithm, we reconstructed the original signal, using the finite summation of the set of simple oscillation functions (sines and cosines), and utilized the Fourier Series and the Discrete Fourier Transform (see Figure 4-4).

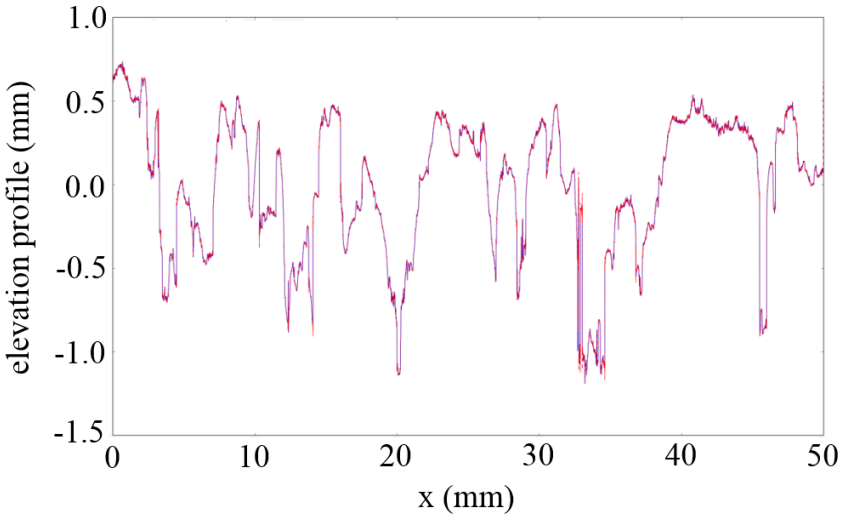

Figure 4-4. A line-can of an asphalt surface. Blue: Original profile; Red: reconstructed profile (courtesy of Tony Beall, Coopertire).

The Nanovea JR25 portable profilometer was recently purchased. The newly measured surfaces are used for the validation of the methodologies and algorithms as explained above.

On the friction tester's road disk, in the future we are planning on replacing the regular sandpaper with Microfinishing Films (from PSI, Inc.), where excellent finish is achieved by the precision grading system used to select abrasive particles for each grade. Classified by the more accurate micron grading system, particle size grading is held to much tighter tolerances than conventional abrasive products. This results in a higher density of the specified particle size available to do the grinding required. This controlled uniformity of particle size, combined with electrostatic coating of the polyester film backing, provides an unexcelled grinding product. Microfinishing Film products are available in both Aluminum Oxide (Al2O3) and Silicon Carbide (SiC). Aluminum Oxide is recommended for use on ferrous materials. Silicon Carbide products should be used on non-ferrous materials. The sheets are available in 80 to 1200 grit (9 to 180 μm average particle size). Other features of this product are longer life and less heat generation. The setbacks are the high price and the minimum quantity offered.

4.2.1 Spectral analysis of profiles; Constant percentage bandwidth

The constant bandwidth spectra were transformed to constant-percentage narrow bands. This is valid only for a transformation on the spatial frequency scale. The fractional-octave-bands (octave and 1/3-octave) used are assumed to be ideal, i.e., the band pass is a square window in the spatial frequency domain. The total power within each window is obtained by summation of all narrow band power contributions falling within the square window. The power of a narrow band that coincides with the boundary between two consecutive fractional-octave bands is divided proportionally over the bands [69].

The procedure was applied to the spectral analysis of sandpaper profiles to investigate the distribution of energy within different wavelength bands. Figure 4-5 shows the results for 1/3-octave bands. The data on the right of the vertical blue lines are to be considered only. The x-axis labels are the centers of the fractional-octave bands. For the 36 grit sandpaper which is the roughest, the energy drops as we move down to smaller wavelengths, while for the 120 and 220 grit it doesn't change substantially.

There were limitations, in terms of the evaluation lengths that were available to us (36 grit: $L = 25\,mm$; 120 grit: $L = 12.8\,mm$; 220 grit: $L = 6.37\,mm$). Therefore, the current interpretations might be inaccurate.

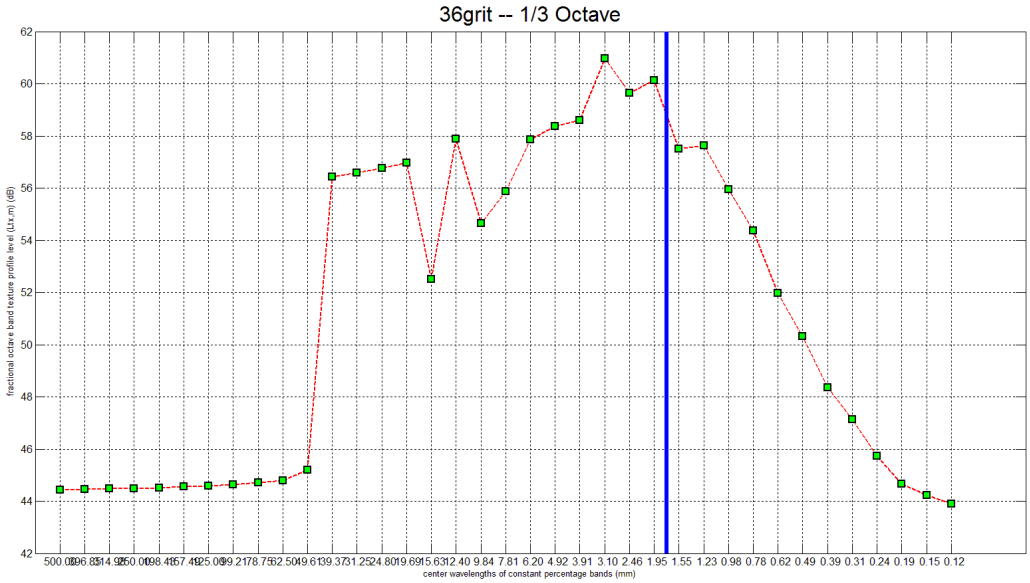

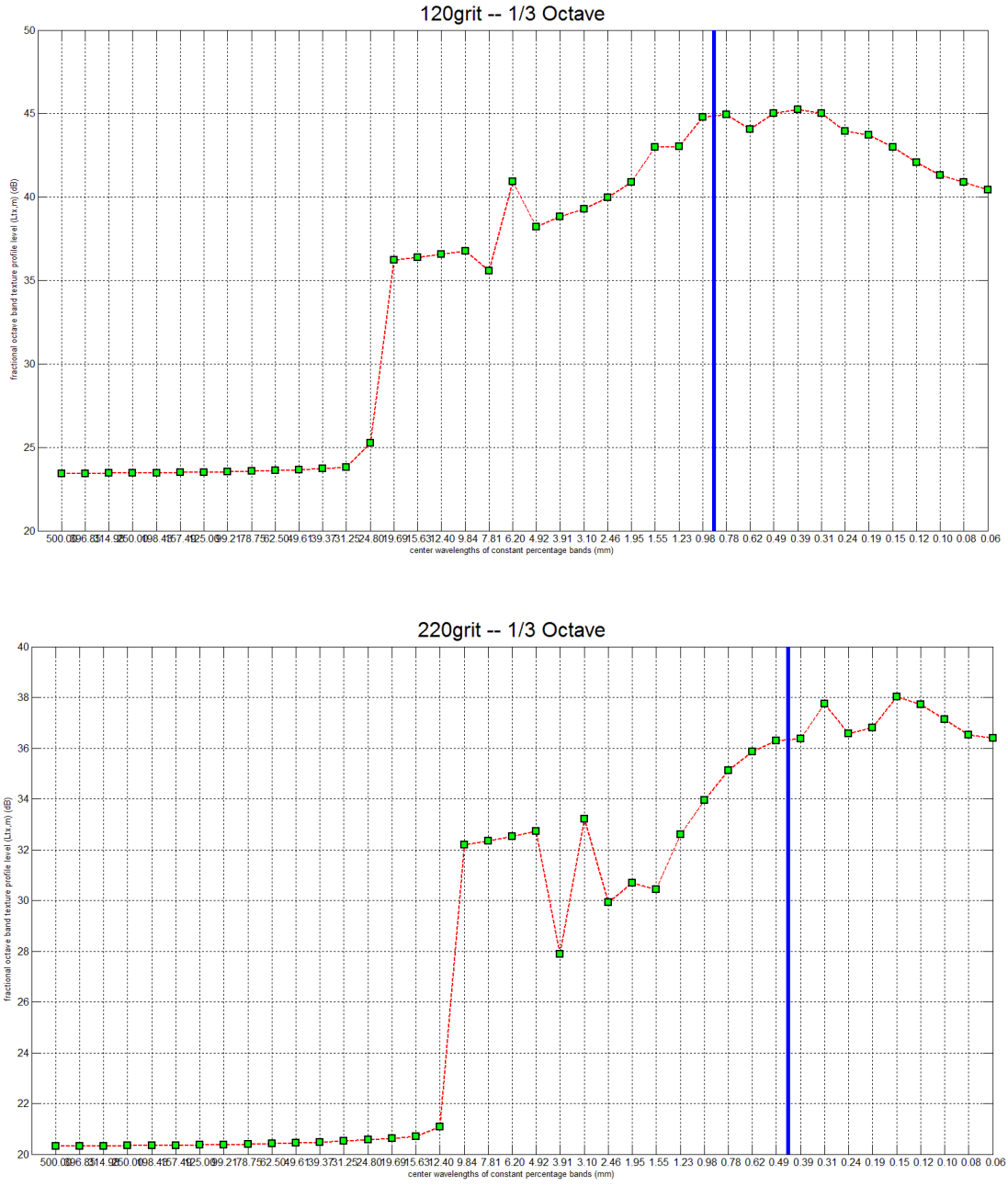

Figure 4-5. Power spectra of three sandpapers transformed to 1/3-octave bands. The data on the right of the vertical blue lines are to be considered only.

4.2.2 Persson‘s technique

Within Persson’s framework, a 2D PSD has to be integrated in the friction estimation procedure. The straightforward and less complicated approach is to compute that from a 2D area measurement. However, 2D profile measurements can take hours or even days, depending on the resolution and size of the area, whereas a number of line scan measurements with high resolution can be carried out in a few minutes. The 2D PSD can be obtained from the 1D PSD, for the limiting cases of: 1) Isotropic surface roughness where the Inverse Abel transform (In image analysis, it is used to project an optically thin, axially symmetric emission function onto a plane) is used. 2) 1D surface roughness (unidirectional polished surfaces), where the angular average of the 2D PSD is obtained from 1D line scans.

For an asphalt surface profile (courtesy of Tony Beall, Cooper Tire), assuming the roughness is isotropic, the 2D angular average of the power spectra of a number of line scans were calculated and averaged. The fractal dimension was calculated to be $D = 2.63$. After treatment of drop outs (replace each of the invalid samples by an interpolated value), we had $D = 2.32$ which is close to the expected value for asphalt (see Figure 4-6). A good match is observed for the 2D power spectra obtained from 2D and 1D measurements. Also, the ‘sum rule’ was satisfied.

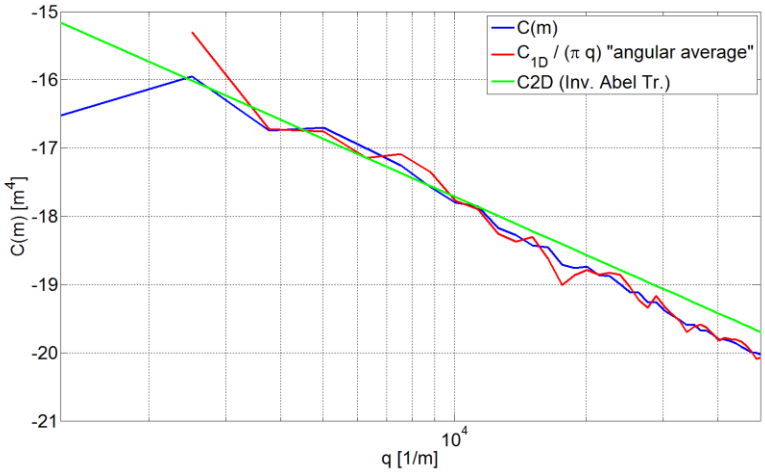

Figure 4-6. Blue: 2D PSD from 2D measurements (assuming isotropic roughness); Green: 2D PSD from 1D measurements via Inverse Abel transform (assuming isotropic roughness); Red: 2D PSD from 1D measurements via computation of angular average (assuming unidirectional roughness).

4.2.3 Klüppel‘s technique

For the asphalt profiles, the Height Difference Correlation Function (HDCF) is computed (see Figure 4-7). The parameters extracted are in agreement with those extracted from the PSD in the previous section. The HDCF and is constructed for two scaling regimes, namely macrotexture and microtexture.

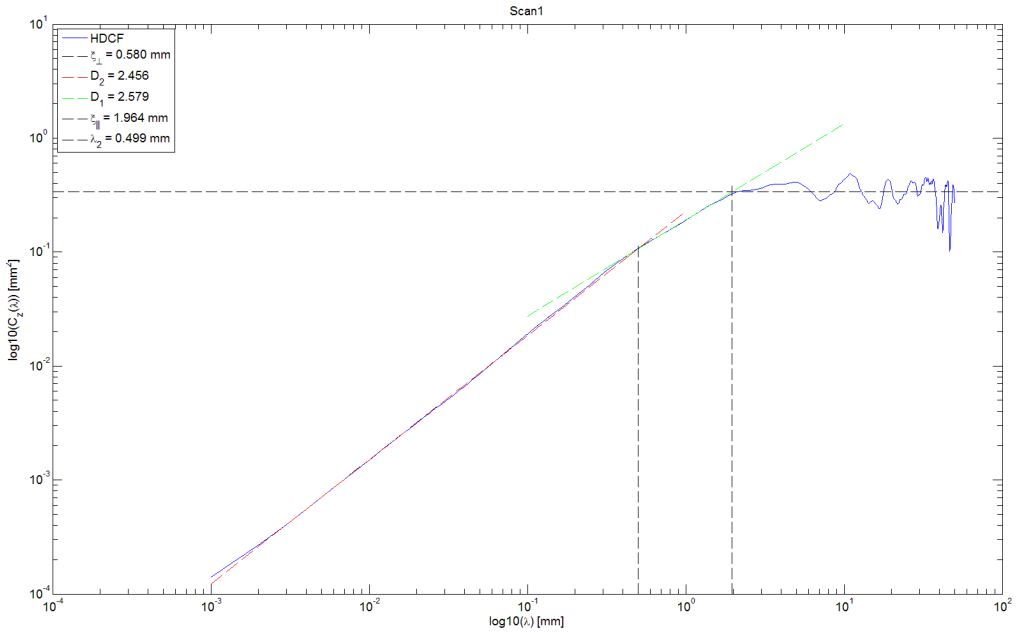

Figure 4-7. Characterization of the asphalt profiles; Height Difference Correlation Function.

4.2.4 Rado's technique

To generate the power spectral density of a profile, Rado has alternatively used the product of the complex conjugate of the Fourier transform and the Fourier transform of the signal ($X^*(f).X(f)$), instead of the Auto Power Spectrum of the profile ($S_{xx}(f)$). The result for one line-scan of the asphalt profile is shown in Figure 4-8. The fractal parameters extracted from the curve are close to the results obtained using Klüppel and Persson theories.

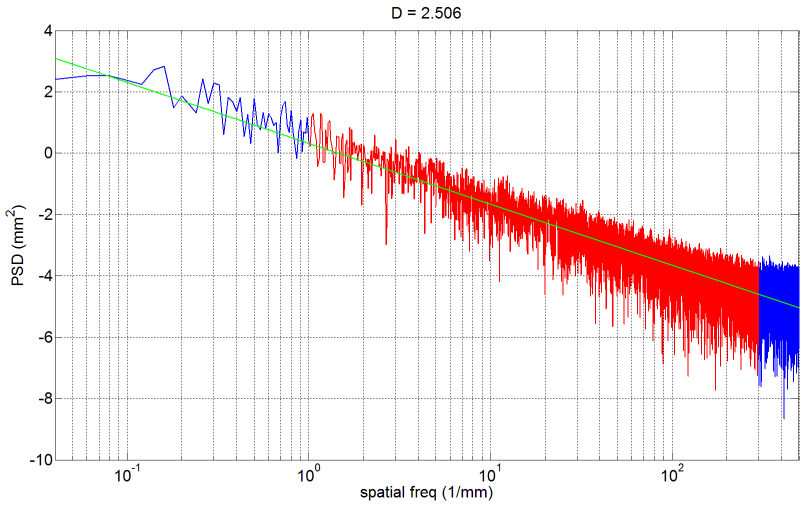

Figure 4-8. Power spectral density of the asphalt profile. The region highlighted in red is linear regression domain.

4.2.5 Power spectrum in two scaling regimes

In Figure 4-9, the surface roughness power spectrum for the 120-grit sandpaper surface is shown. It is calculated from the profile measurements by the Nanovea JR25 optical profilometer. The power spectrum is an average over the power spectra of 10 individual line-scan measurements. The evaluation length has been long enough to capture the roll-off region and the range of wavelengths that contribute to friction.

The short-distance cut-off wavelength is selected to be $\approx 6\ \mu m$, such that the rms-slope equals 1.3 [78]. Yet, the horizontal resolution of the profile data used in this study is $7\ \mu m$, which means that the smallest wavelength that can be processed is $14\ \mu m$ (Nyquist spatial frequency). However, as expected for fractal surfaces, the power spectrum curve on a log-log scale demonstrates linear behaviors for wavevectors larger than q_0 in the macrotexture and microtexture regions. Therefore, in order to have more accurate friction predictions the spectrum is linearly extrapolated to $\lambda_1 = 6\ \mu m$ ($q_1 = 2\pi/\lambda_1$).

The fractal dimension can be calculated from the slope of the log-log power spectrum curve. For the studied sandpaper surface, the fractal dimension is 2.30. In the two scaling regimes approach, a transition wavelength is detected in the power spectrum at around $\lambda_2\ (= 2\pi/q_2) \approx 150\ \mu m$ that characterizes the gradual slope change between the two scaling regions. The fractal dimension is calculated to be 2.69 and 2.18 for macrotexture and microtexture, respectively.

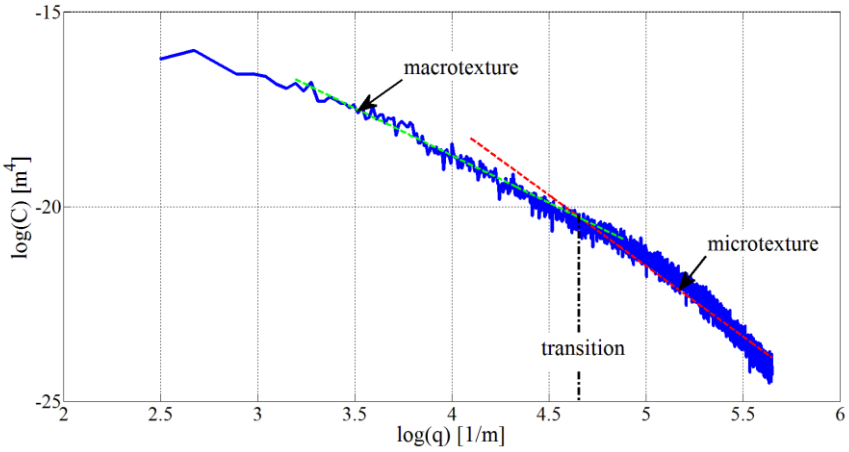

Figure 4-9. Power spectral density of surface roughness of 120-grit sandpaper. The measurements were carried out using the Nanovea JR25 optical profilometer, with a lateral resolution of $7\ \mu m$. This power spectrum is an average over the power spectra of all the individual line-scan measurements on the surface. A transition wavelength of q_2 ($\approx 2\pi/150\ \mu m$) is selected that separates the macrotexture ($C_1(q)$) and the microtexture ($C_2(q)$) length scales. The fractal dimension is calculated to be 2.69 and 2.18 for macrotexture and microtexture, respectively.

4.3 Classification of Road Surfaces

4.3.1 Texture parameters

We use five sets of road profiles measured via the Optical Gaging Products, Inc. (OGP) Digital Range Sensor System DRS-8000 by researchers at Michigan Tech Transportation Institute. The FN values are site values from the MDOT friction trailer before the pavement is cored. The lateral resolution of the data is $45\,\mu m$. Twelve 46 mm long traverse lines were measured parallel to traffic directions evenly distributed across each surface.

For each of the five surfaces, the average of "mean square roughness" over the twelve samples was calculated. It was detected that as FN grows, mean square roughness increases as well. Perfect correlation (correlation coefficient $r^2 = 0.975$) was obtained between the tire-pavement friction number and the mean square roughness of the surface profiles, which is equal to the area under the PSD plots (Table 4-3 and Figure 4-10).

Profile	Friction Number (FN)	Mean Square Roughness	Area Under PSD
14d1 (4-lane suburban)	42	3.54	3.54
15d1 (4-lane suburban)	46	3.83	3.83
26d1 (6-lane city)	35	3.52	3.52
29d1 (4-lane rural)	55	5.45	5.45
30b1 (4-lane rural)	76	7.16	7.16

Table 4-3. Friction Number, Mean Square Roughness, and the area under the PSD curve for five road profiles.

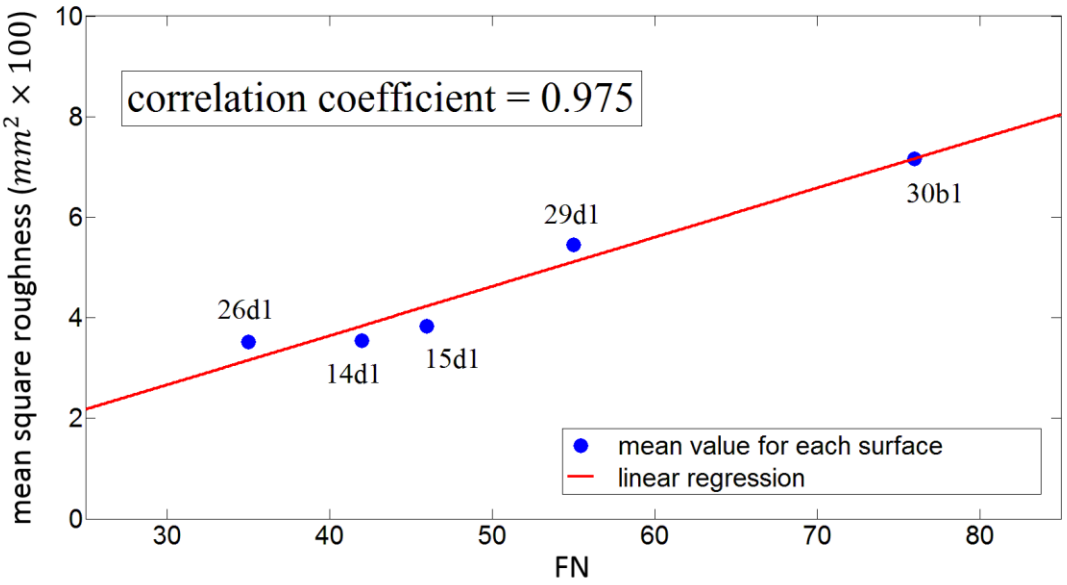

Figure 4-10. Correlation between the tire-pavement friction and the mean square roughness (= area under PSD) for the five profiles. Each point represents a road surface core.

4.3.2 Indenters method

For pavement classification using the Indenters method, a median θ of the 12 samples is set as the angular parameter for each specimen. The reason why median is used here is that compared to mean, median is less affected by extreme values within a set of observations. The results of profile characterization using θ are presented in Table 4-4 and Figure 4-11. It can be said that there exists a relatively perfect correlation between θ and friction. The correlation coefficient r^2 is 0.9652 in this case, which means that this angular parameter is able to predict tire-pavement friction with very good precision. This angular parameter is a good predictor of wet friction; the method can be used for dry contact as well. However, we have to take into account the adhesion part of friction, and also the true contact area.

Profile	**Friction Number (FN)**	**Angular Parameter θ (degrees)**
14d1 (4-lane suburban)	42	6.0117
15d1 (4-lane suburban)	46	6.8890
26d1 (6-lane city)	35	4.0073
29d1 (4-lane rural)	55	7.5898
30b1 (4-lane rural)	76	9.8631

Table 4-4. Friction Number and Angular Parameter θ for the five road profiles.

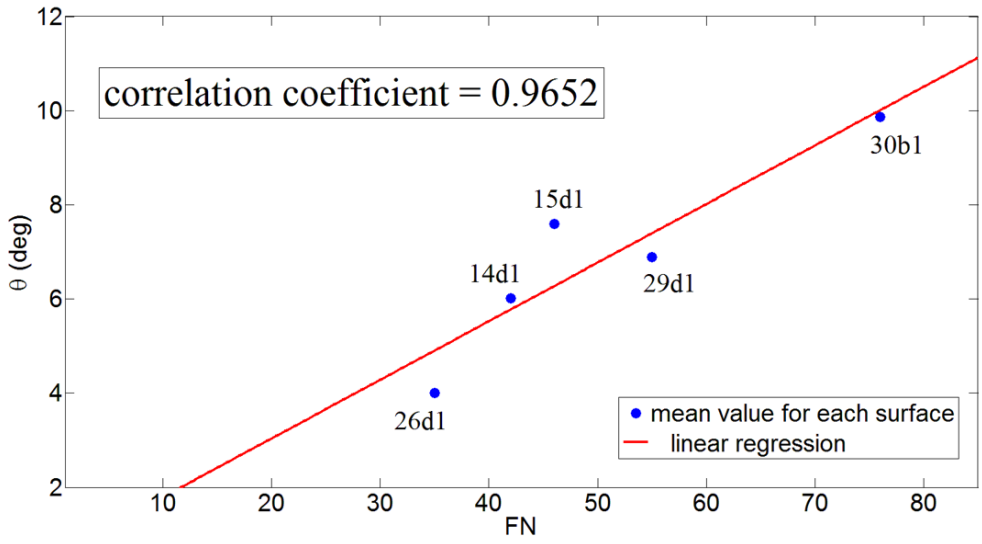

Figure 4-11. Correlation between tire-pavement friction and the angular parameter of the Indenters method for the five surfaces. Each point represents a road surface core.

4.3.3 Fractal analysis

4.3.3.1 Global fractal parameters

Many fractal properties are related to the evolution of the wavelet coefficients across scale [105]. One possible way to check for a fractal behavior is to investigate the evolution of the energy in the signal with respect to scale. Let $E_a = \int [CWT(a,b)]^2 db$ denote the energy at scale a, where CWT is the Continuous Wavelet Transform. Figure 4-12 illustrates a relation of the type $E_a \sim a^{\gamma}$ for some γ and a across a large range of scales, which indicates that the energy decays as a power law in scale. Now that it is verified that the profiles display a fractal behavior, this property will be used to characterize the signals.

A signal has a well-defined Correlation Exponent, if $C(l) \sim l^{-\beta}$ with $\beta > 0$ holds across a range of values of l, where $C(l)$ is the autocorrelation of the signal, and l is lag. For a fractal signal, we expect linear

behavior on almost all the range of possible values of l. The results shown in Figure 4-13 (Left) agree with Figure 4-12 and confirm the fractal behavior in the signals.

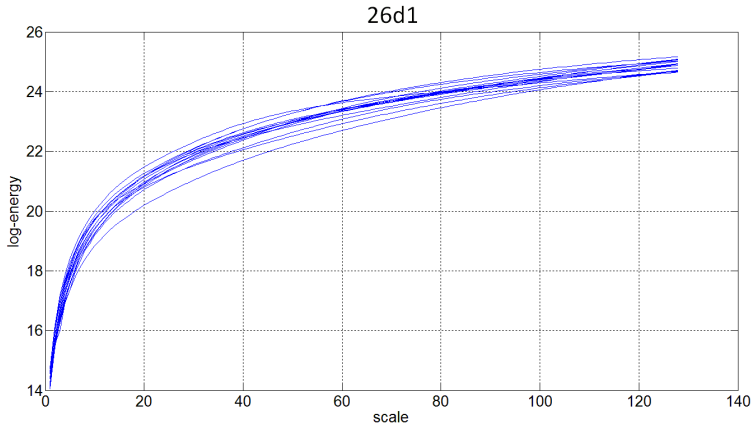

Figure 4-12. Log-energy with respect to scale for twelve samples from surface 26d1.

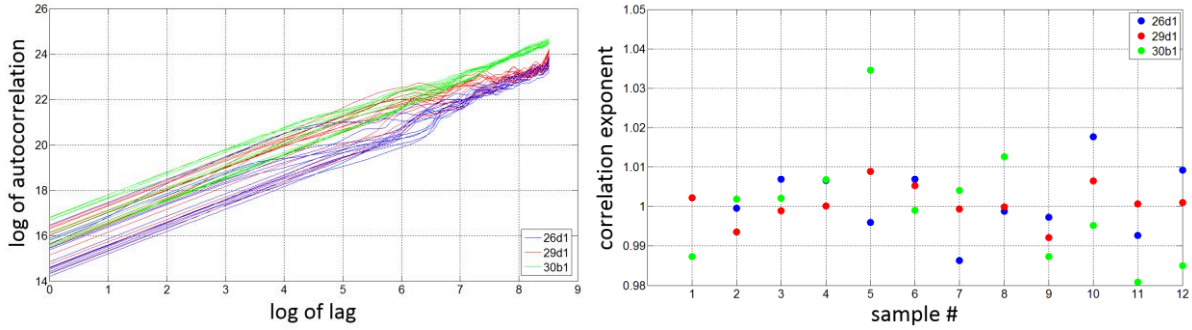

Figure 4-13. Left: Log-autocorrelation as a function of Log-lag for twelve samples from each of the three surfaces. Right: Classification of three surfaces using correlation exponent.

Nevertheless, Correlation Exponent is a global fractal quantity and it is not possible to separate the classes based on the information brought by this parameter. See Figure 4-13 (Right).

Figure 4-14 shows the typical behavior of Regularization Dimension on profiles. If the plot is linear in a certain range of values of scale, then the signal is considered fractal. There are however two linear regimes, one corresponding to lower regularization (high frequencies), and the other to large smoothing (low frequencies). This shows that the investigated road profiles have two well-defined dimensions, macro- and micro-texture, that behave in different ways.

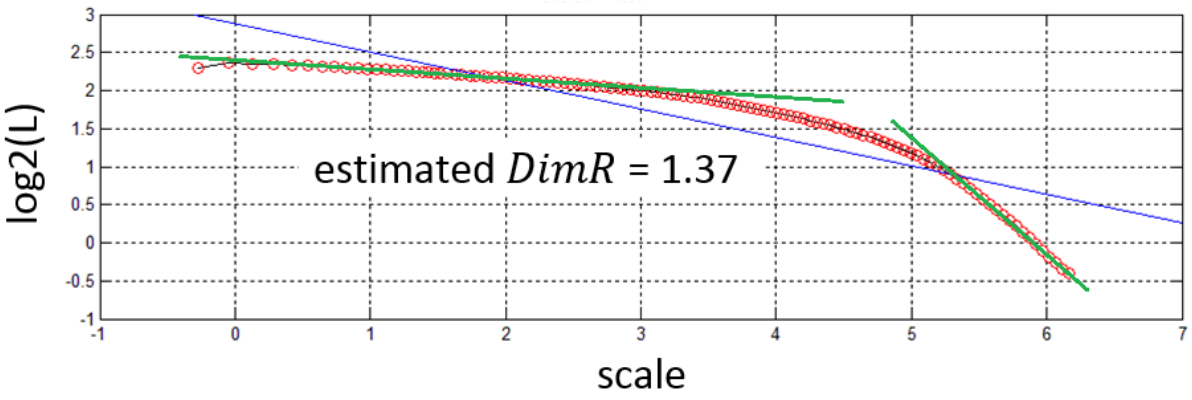

Figure 4-14. Log-convoluted length with respect to scale.

	26d1			29d1			30b1		
DimR	1.28	***macro***	1.14	1.33	1.15		1.29	1.19	
		micro	2.02		2.53			2.05	
	1.40	***macro***	1.14	1.27	1.14		1.30	1.18	
		micro	1.74		2.10			1.96	
	1.39			1.34			1.29		
	1.33			1.33			1.33		
	1.29			1.28			1.35		
	1.27			1.31			1.36		
	1.37			1.27			1.30		
	1.38			1.28			1.28		
	1.36			1.32			1.33		
	1.34			1.30			1.32		
	1.36			1.33			1.33		
	1.34			1.28			1.34		

Table 4-5. $DimR$ values for twelve samples from each of the three surfaces. For the first two rows, the separate $DimR$ values for microtexture (lower cell) and macrotexture (upper cell) are presented, as well.

$DimR$ values are calculated for the three surfaces (Table 4-5). For the first two samples of each surface, $DimR$ for micro- and macro-texture is calculated separately, as well. Still, the ranges of exponents for different classes often overlap. $DimR$ is a global quantity, and it is not able to characterize a given class of profiles. Therefore, $DimR$ and β may not be used to explain the differences in friction of the various profiles. As a result, we move on and investigate if local fractal parameters and particularly the Pointwise Holder exponent can serve as a tool in characterization of road profiles.

4.3.3.2 Local fractal parameters

We learned that global fractal parameters (e.g., correlation exponent, regularization dimension, fractional dimension) are not always able to characterize and discriminate between road profiles. For all we know, they could be largely unrelated to the friction coefficient. On the other hand, local parameters (e.g., pointwise Holder exponent) might allow separating road profiles that have different friction coefficients. The claim could be supported by the fact that friction is mainly a local phenomenon.

Since α (Holder exponent) is defined at each point, we associate it to f (Holder function). A Holder function of one sample of surface 30b1 is illustrated in Figure 4-15. Analysis results showed that Holder exponent and Holder function cannot tell if a signal is fractal. However, they provide a rich description of the local singularity structure of a signal, almost too rich for characterization purposes.

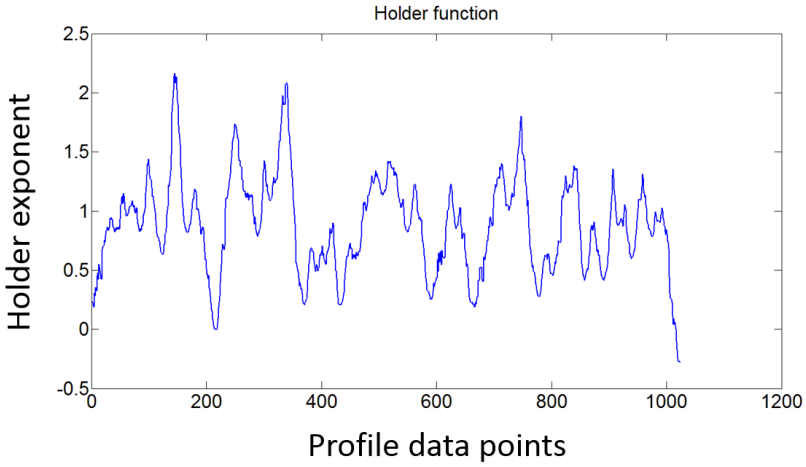

Figure 4-15. Holder function for one sample from 30b1.

Thus, for profile classification using Pointwise Holder exponent, one may start by using median of the Holder function. While the median will subsume information pertaining to the whole signal, it is still a

local parameter. Using the median (or even the mean) of the Holder function is consistent with the fact that the friction results from an average of many local interactions. Nevertheless, as seen in Figure 4-16, the procedure fails to separate the three surfaces.

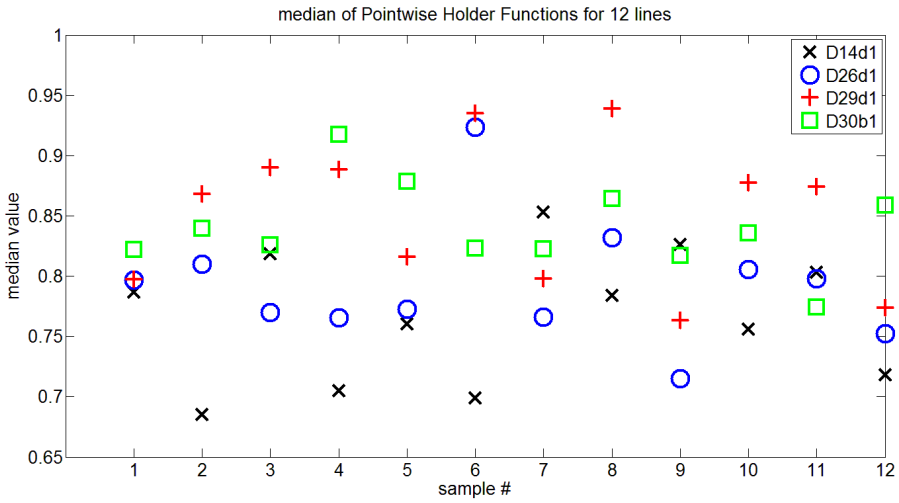

Figure 4-16. Classification of the three surfaces using Holder median. For twelve samples from three surfaces, each sample's median value of the Pointwise Holder exponent is displayed.

Therefore, instead of restricting to median, the histograms of Hölder functions are studied [106]. For the learning (training) class, eight profiles were randomly chosen among the twelve profiles from each surface. The remaining four profiles are used as the testing class. Histograms of pointwise Hölder exponents for each profile were created. Therefore, eight histograms represent the learning class of each surface (see Figure 4-17). The number of the histogram bins can be equal to or less than the number of pointwise Hölder exponent values. Next, the mean values of the eight histograms are computed. For each pointwise Hölder exponent bin, the standard deviation is also calculated.

To be able to examine the testing class profiles, the mean and the standard deviation values are then used to create new Gaussian functions for each bin, so that the learning class of every surface has a set of Gaussian functions. For each new profile from the testing class of a surface, $V_1, V_2, \ldots, V_n$ values are computed using the Gaussian functions of the learning classes of all surfaces (see Figure 4-18). Finally, T is computed for each surface by summing the V's ($T_j = \Sigma V_i$ (for surface j)). The T values are compared, and if T_j is largest for a surface, the new profile belongs to that surface. The comparison results are shown in Table 4-6. Each cell symbolizes the result of the classification for one test sample from one surface. Number '1' represents successful classification, '0.5' denotes marginal success, and '0' means failure to classify. An overall correct classification rate of 87.5% was achieved.

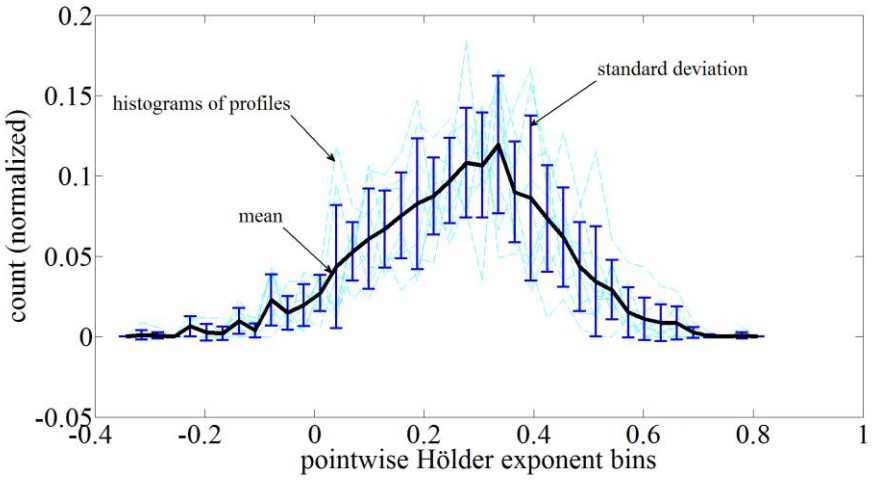

Figure 4-17. Normalized histograms of the pointwise Hölder exponents of the profiles of the learning class for one road surface. The means and the standard deviations are plotted for each bin. The number of the histogram bins used is less than the number of pointwise Hölder exponents.

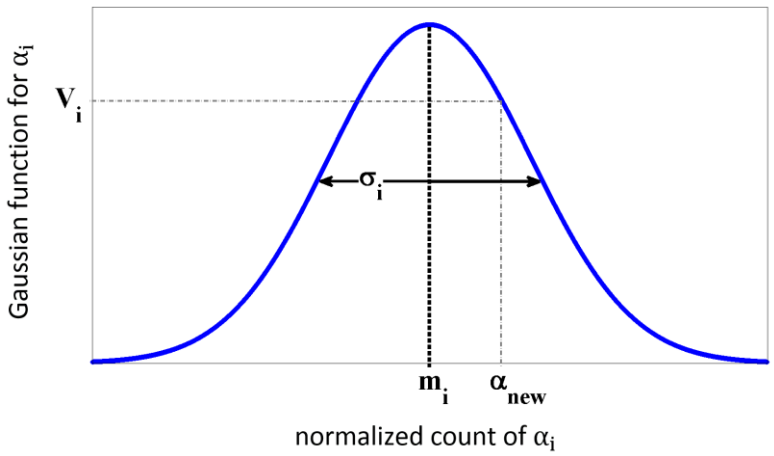

Figure 4-18. Gaussian function for one pointwise Hölder exponent bin with respect to the normalized count in that bin. V_i is the function value corresponding to the new profile's normalized count.

		Surface				
		14d1	**15d1**	**26d1**	**29d1**	**30b1**
Test Sample	**#1**	1	0	1	1	1
	#2	1	1	1	1	1
	#3	1	0.5	1	1	1
	#4	1	1	0	1	1
sum		17.5 / 20 = 87.5%				

Table 4-6. End results of classification via the pointwise Holder exponent for the four test samples from each of the five surfaces. 1: success, 0.5: marginal success, 0: failure.

4.4 Persson's theory for friction estimation; Real area of contact

A correct estimation of the real area of contact is a fundamental and integral piece in understanding the rubber-road contact and friction. The real area of contact has to be calculated in the process of friction prediction. Therefore an accurate approximation of the coefficient of friction could inherently authenticate the correctness of the estimation of the real contact area.

We start by trying to estimate the kinetic friction coefficient for polyisoprene rubber sliding on a substrate with a self-affine fractal surface profile characterized by the Hurst exponent $H = 0.85$. Calculations are presented for the magnifications $\xi = 100$ and 1000, and with $q_0 h_0 = 1$ and $q_0 = 2000$. For the $\xi_{max} = 100$ case we show results for three different nominal pressures, $\sigma_0 = 0.1$, 1, and 10 MPa. As illustrated in Figure 4-19, good agreement is observed between our simulations and Persson's data.

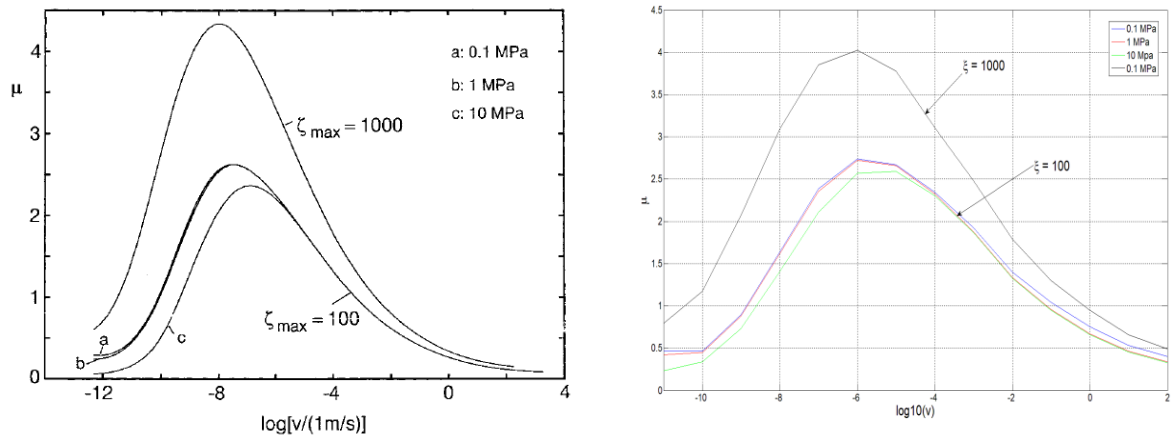

Figure 4-19. The friction coefficient for polyisoprene rubber sliding on a fractal surface with $D_f = 2.15$. Calculations are presented for the magnifications $\xi = 100$ and 1000, and with $q_0 h_0 = 1$ and $q_0 = 2000$. For the $\xi_{max} = 100$ case we show results for three different nominal pressures, $\sigma_0 = 0.1$, 1, and 10 MPa; Left: Persson's estimations; *Reproduced from [11] with permission from AIP Publishing;* Right: Current research.

Thus, we can expect our estimation of the real contact area to be accurate too. To further assess this assertion, we did a more detailed study and carried out more simulations to compare the outcome with friction prediction results obtainable from the literature. We investigated the rheological viscoelastic model of Figure 4-20 [11]. The model corresponds to the viscoelastic modulus,

$$E(\omega) = \frac{E_1(1-i\omega\tau)}{1+a-i\omega\tau} \qquad (4\text{-}1)$$

where $a = E_1/E_2$ and $\tau = \eta/E_2$ is the relaxation time. In all calculations below, $\tau = 0.001s$, $E_1 = 10^9 Pa$, and $a = 1000$.

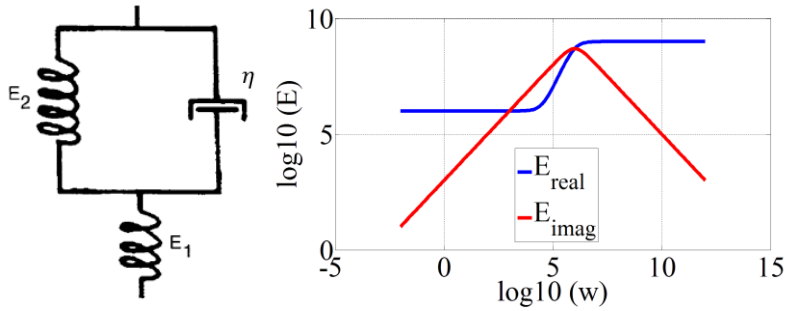

Figure 4-20. Left: the rheological model; *Reproduced from [11] with permission from AIP Publishing;* Right: master curve for the rheological model.

In Figure 4-21 the real contact area (RCA) is plotted with respect to magnification for four different sliding velocities, for the rheological model on a self-affine surface. As magnification increases, RCA become smaller. Also, RCA decreases with increasing velocity.

Friction vs. Velocity for the rheological model on a self-affine substrate is plotted in Figure 4-22 for three different magnification levels. Friction has a peak that corresponds to the peak of $tan\delta$. The magnitude increases as we go down to smaller minimum wavelengths.

Friction vs. Velocity for the rheological model on a self-affine substrate is plotted in Figure 4-23 for different fractal dimensions. Friction increases with fractal dimension (Hurst exponent decreasing).

Maximum Friction vs. Fractal Dimension for the rheological model on a self-affine substrate is shown in Figure 4-24. Friction's peak increases with the Hurst exponent at first, but then descends.

The results confirm that Persson's estimations of RCA and friction coefficient are reproduced accurately.

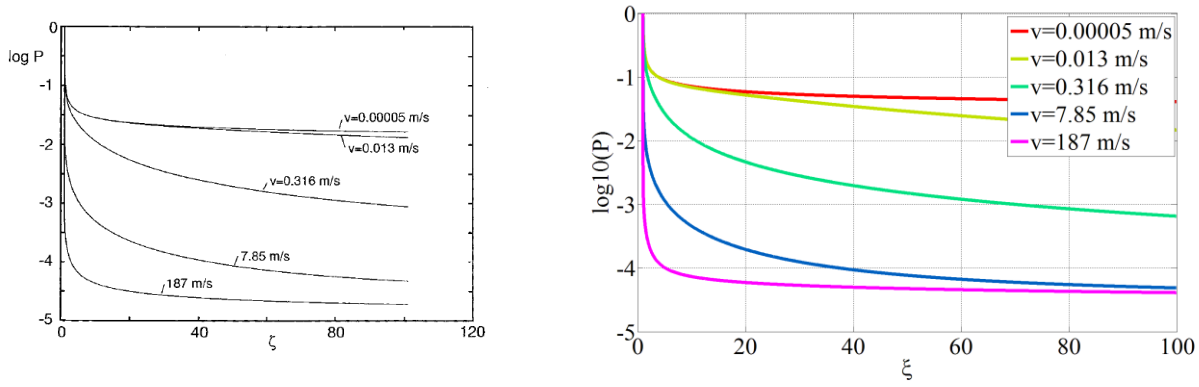

Figure 4-21. RCA vs. Magnification for the rheological model on a self-affine substrate. Left: Persson's results; *Reproduced from [11] with permission from AIP Publishing;* Right: current research.

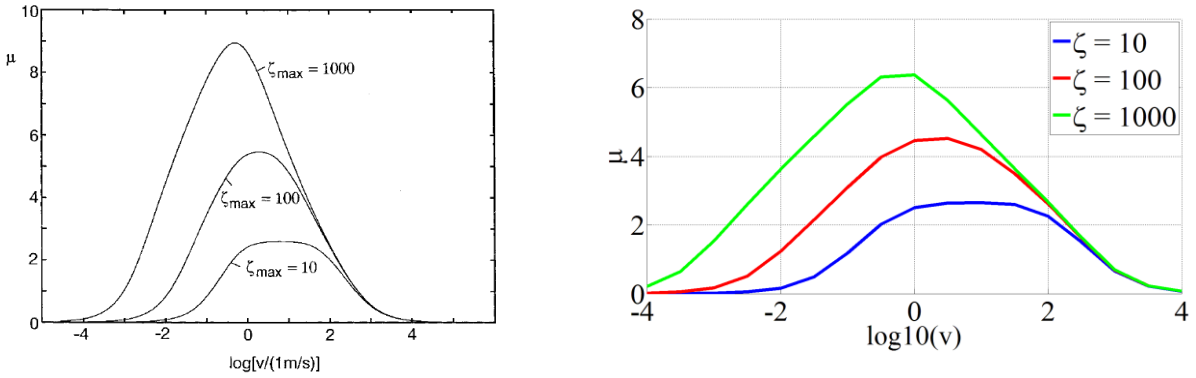

Figure 4-22. Friction vs. Velocity for the rheological model on a self-affine substrate; Left: Persson's results; *Reproduced from [11] with permission from AIP Publishing;* Right: current research.

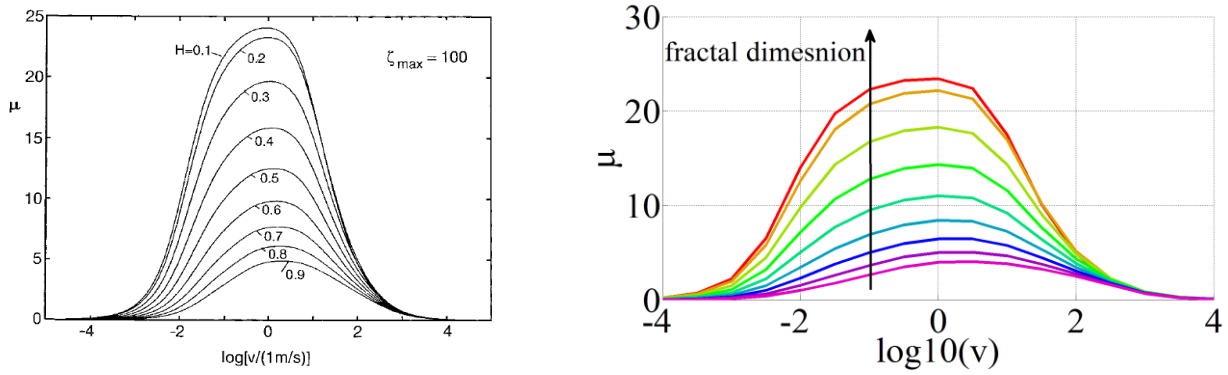

Figure 4-23. Friction vs. Velocity for the rheological model on a self-affine substrate; Left: Persson's results; *Reproduced from [11] with permission from AIP Publishing;* Right: current research.

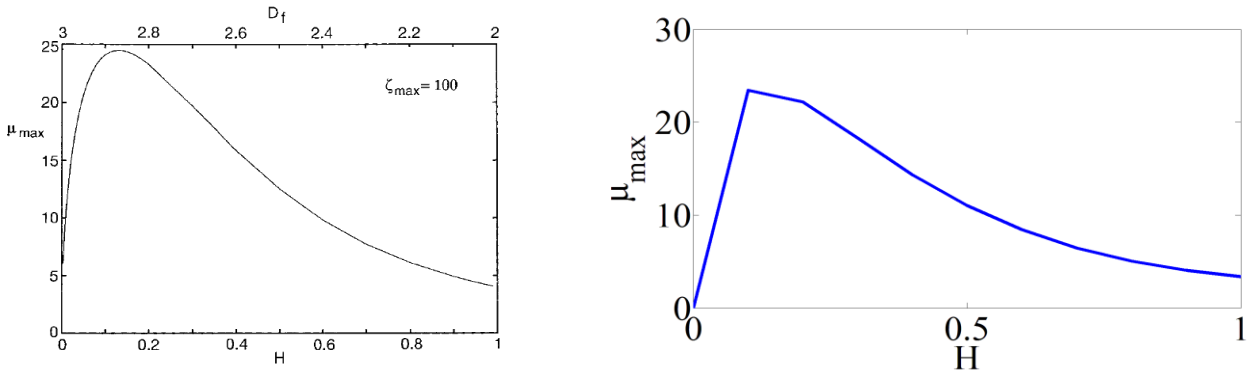

Figure 4-24. Max Friction vs. Fractal Dimension for the rheological model on a self-affine substrate; Left: Persson's results; *Reproduced from [11] with permission from AIP Publishing;* Right: current research.

Then, we also study how RCA changes with magnification for real tread compounds, since the viscoelastic master curve of a tread compound is quite different from that of the simple rheological model. In Figure 4-25 and Figure 4-26, we see that RCA decreases with magnification, for a carbon black filled Styrene Butadiene rubber compound at low strain and a tread compound at large strain, respectively. In both cases, RCA decreases with velocity too. We see that RCA increases when using

large strain viscoelastic modulus. Using the modulus data for a real tread compound, the RCA ratio is close to the numbers mentioned in the literature for ABS-braking sliding velocities (~ 1%).

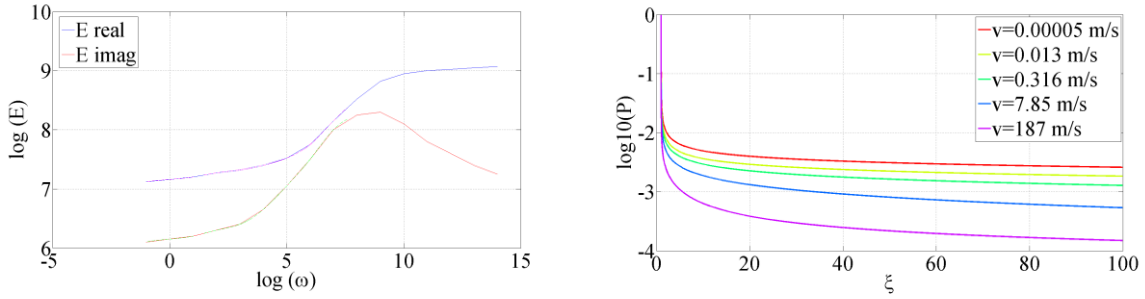

Figure 4-25. SBR–CB (small strain); Left: Master curve; Right: Real Area of Contact vs. Magnification

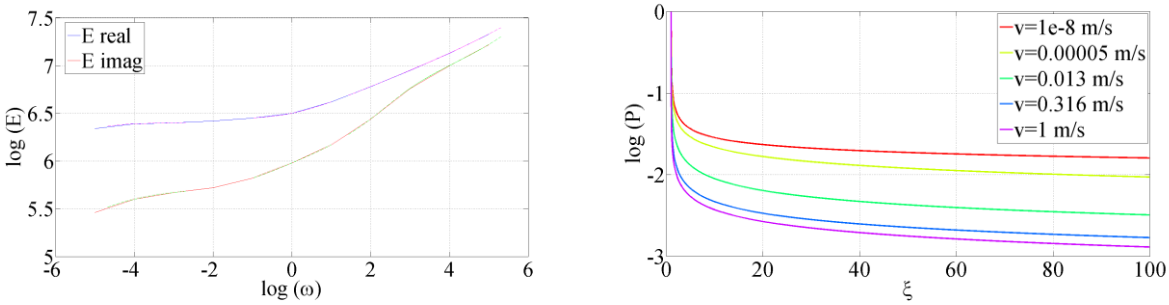

Figure 4-26. Tread Compound (Large Strain); Left: Master curve. Righ: Real Area of Contact vs. Magnification

4.4.1 Sensitivity of Friction to Surface Parameters

This analysis carried out to learn how the different pavement parameters that are used in the friction prediction algorithm affect friction and how sensitive the estimations are to each. For each case, we have four surfaces, where one is the original 240 grit sandpaper, and the other three are pseudo surfaces obtained by tweaking one parameter at a time.

First, the effect of the short distance cut-off wavevector (q_1) is studied (see Figure 4-27). As q_1 rises and smaller length scales are included in the realization of the substrate, the logarithmic PSD moves further to the right (larger wavevectors), and the short-distance cut-off wavelength decreases which in turn increases friction (see Figure 4-27 Right).

Then, we investigate the influence of the Roll-off wavevector (q_0). As apparent in Figure 4-28, when q_0 is reduced and larger wavelengths (macrotexture roughness) are included in the realization of the substrate, the logarithmic PSD moves further to the left (smaller wavevectors) that leads to an increase in friction.

In Figure 4-29, the effect of the vertical cut-off distance (h_0) is studied. A larger h_0 means a larger rms roughness, which would surely bring about larger friction coefficients.

Finally, the influence of the fractal dimension is illustrated in Figure 4-30. A larger fractal dimension simply adds more microtexture features to the surface, and consequently increases friction.

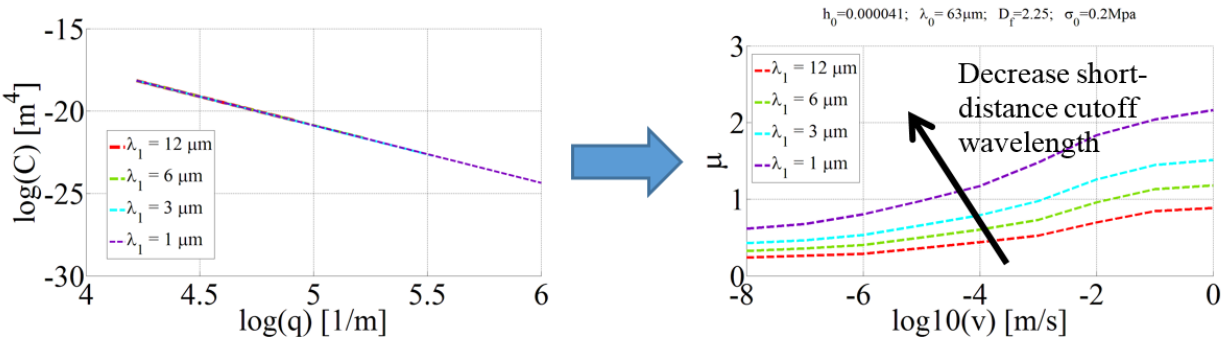

Figure 4-27. The effect of changes in short-distance cut-off wavevector/wavelength; Left: Power spectral density; Right: Friction vs. sliding velocity.

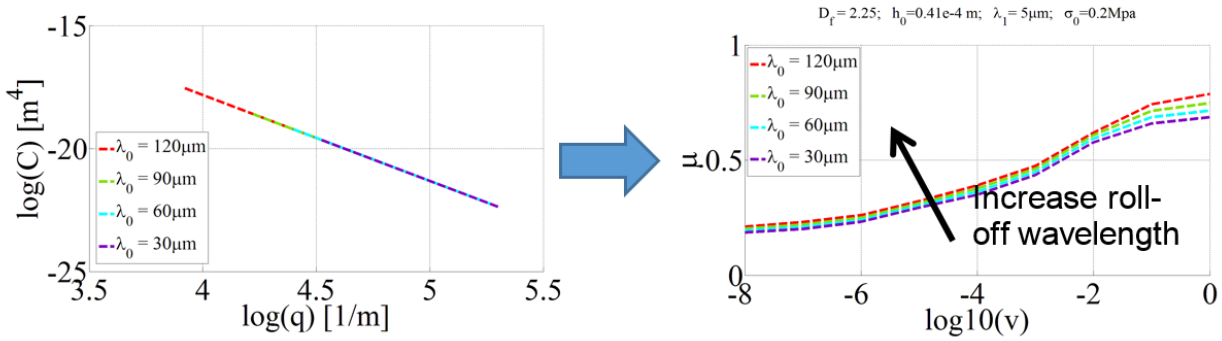

Figure 4-28. The effect of changes in Roll-off wavevector/wavelength; Left: Power spectral density; Right: Friction vs. sliding velocity.

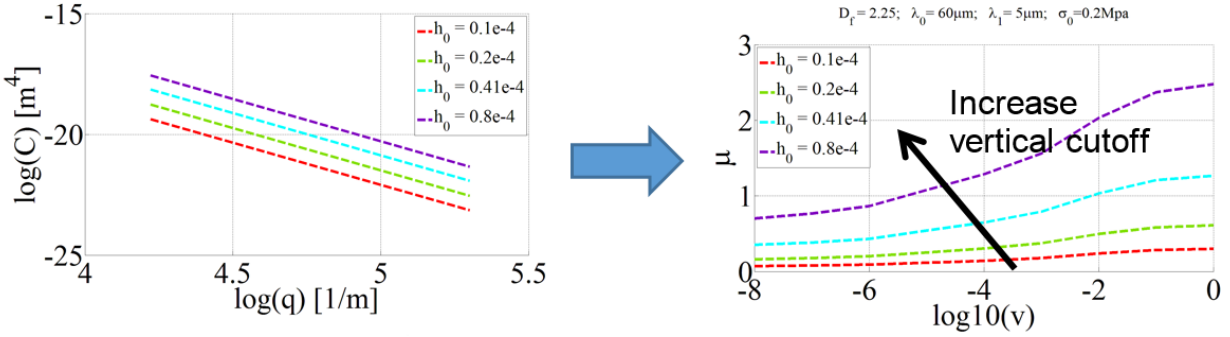

Figure 4-29. The effect of vertical cut-off length; Left: Power spectral density; Right: Friction vs. sliding velocity.

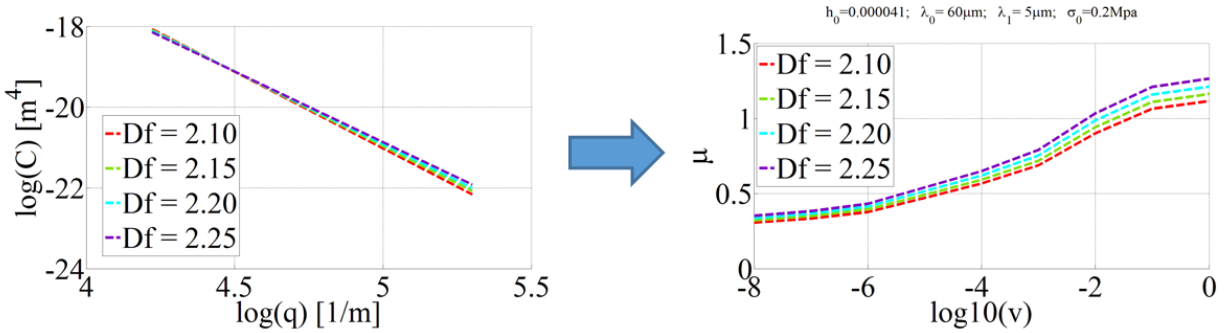

Figure 4-30. The effect of changes in fractal dimension/Hurst exponent; Left: Power spectral density; Right: Friction vs. sliding velocity.

4.4.2 Contribution of different length scales to friction

Which one is more important: macrotexture or microtexture? How important is the short-distance cut-off wavelength; e.g. what happens if we cut the spectrum at $10\ \mu m$ instead of $5\ \mu m$, and how much does that affect friction? Can we find length scale bands that have equal impact on friction; e.g, decades, octave bands, 1/3 octave bands, linear bands? To answer all these questions, in this section we do a quantitative analysis of the contribution of different wavelength levels to friction.

The first step is breaking the power spectrum of the surface into a number of length scale bands. For Surface segmentation, we use two approaches: 1) Taking the complete original surface, where contributions from wavelength bands add up to the friction value of the original surface with all the length scales; and 2) Breaking the roughness into several independent surfaces that leads to a higher friction coefficient than the original surface, since '$real\ contact\ area/nominal\ contact\ area$' ratio is one for each segment.

For the rubber side, we have used tread compound master curves at both low and large strains, to see if the dynamic behavior and characteristics of rubber makes a difference.

There are an infinite number of ways we can define the spatial frequency bands. We chose to investigate: 1) Linear Spatial Frequency Bands; 2) Logarithmic Length Scale Bands; 3) Linear Length Scale Bands; and 4) Friction vs. Continuous Length Scale, because they intuitively and also computationally made more sense.

After a careful examination of the all the results, we reached a few important conclusions. Here, only the results that are key for explaining those findings are presented. All of the following results are for the state of 'taking the complete original surface'.

In Figure 4-31 (left), the power spectral density of a sandpaper profile is illustrated. Unlike the '$\log PSD - \log q$' that we're used to seeing, in this case, we have both x and y axes in linear scale. The reason why we did that is that in the friction estimation integrals, the power spectral density and the wavevector are not logarithmic. Therefore, studying those quantities in linear scale is theoretically more relevant to length scale involvement. The equally wide spatial frequency bands are in linear scale, as well. The same plunging behavior is seen in the $C(q)$ graph when we zoom in to the plateau at higher frequencies.

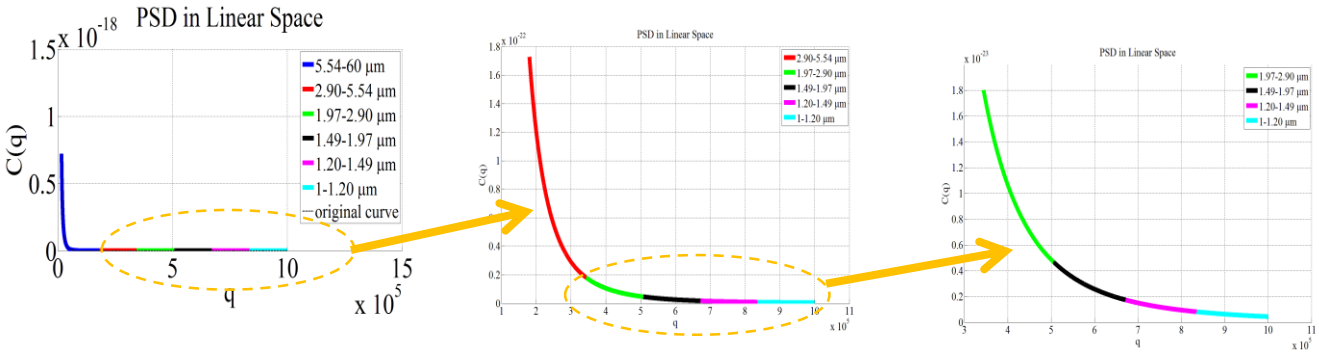

Figure 4-31. Power spectral density of a sandpaper profile in linear scale. The equally wide spatial frequency bands are in linear scale, as well.

Then, the length scale bands in linear scale are transformed into a log-log PSD (see Figure 4-32 Left). Since wavevector in linear scale is the integration variable in friction estimation, we observe a monotonic decrease in contribution of linear wavevector bands to friction (see Figure 4-32 Right). For the rubber, we

have used a tread compound at large strain. Another important point that is reinstated here is that hysteresis friction is very sensitive to the short-distance cut-off wavelength.

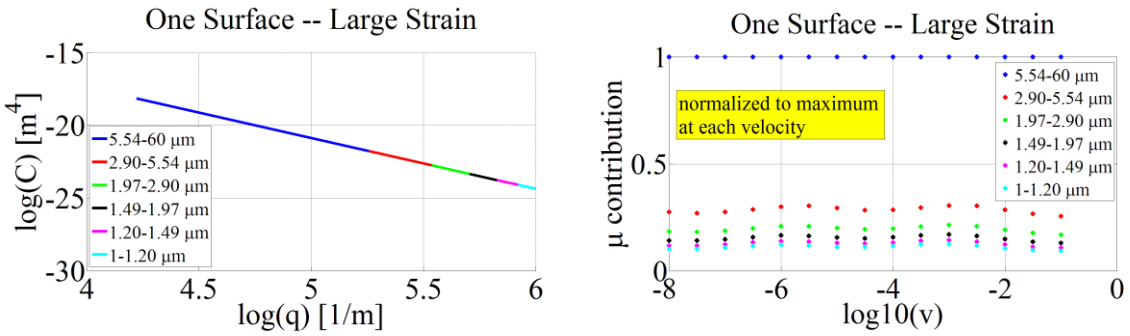

Figure 4-32. Left: Power spectral density of a sandpaper profile with spatial frequency bands are in linear scale; transformation into log-log PSD; Right: Normalized-to-max friction (tread compound at large strain on sandpaper) contribution from the frequency bands with respect to sliding velocity.

For the same rubber and substrate, Figure 4-33 illustrates logarithmic length scale bands (Left), and the normalized-to-max contribution of each band to friction (Right). It is apparent that the contribution of the different bands is not the same anymore at different sliding velocities. However, one interesting point that is noticeable here is that every decade in length scale is roughly equally important.

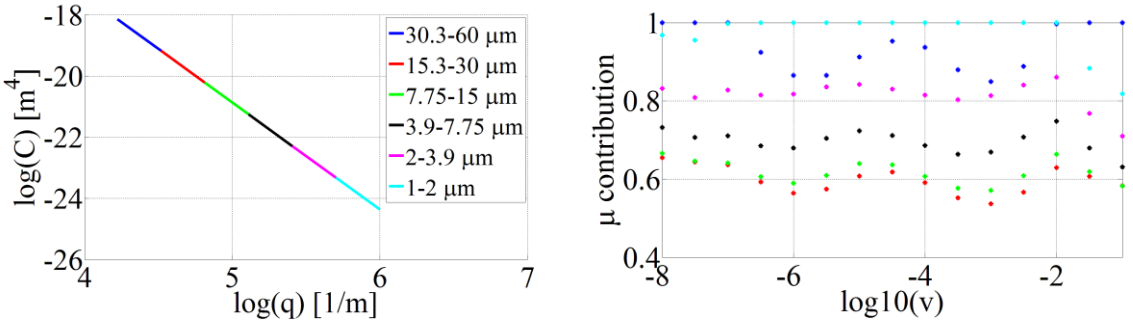

Figure 4-33. Left: Power spectral density of a sandpaper profile with logarithmic length scale bands; Right: normalized-to-max contribution of each band to friction (tread compound at large strain on sandpaper) with respect to sliding velocity.

The next step is to investigate the effect of $tan\delta$, which is important because it's strongly correlated with hysteresis friction (see Figure 4-34). By keeping $tan\delta$ constant (see Figure 4-35), we can factor out the influence from rubber's moduli changes with speed and frequency and only take into account the surfaces dynamic properties. That helps us have a more accurate assessment of the contributions from different length scales.

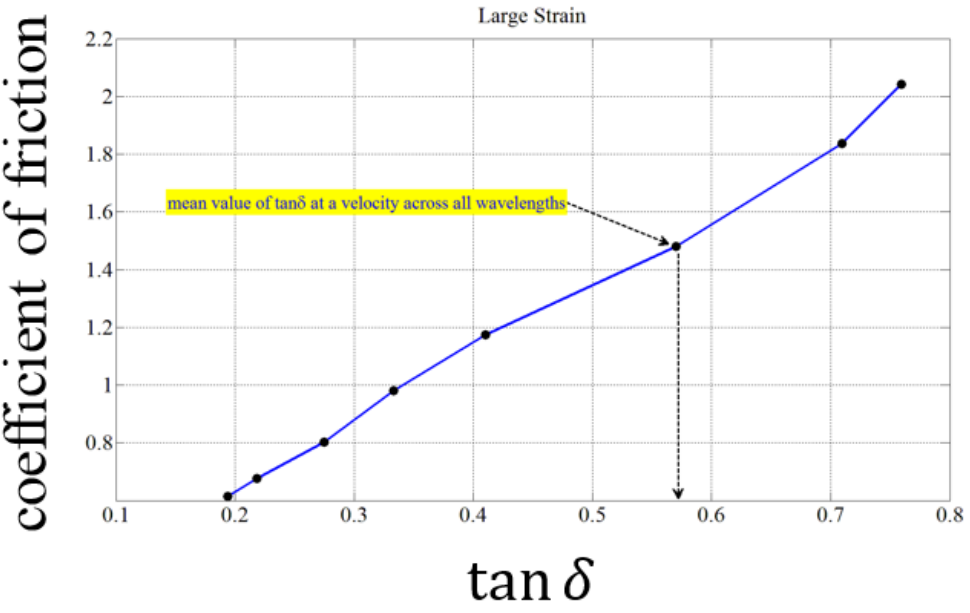

Figure 4-34. Correlation between coefficient of friction and $tan\delta$ for a large strain tread compound on sandpaper.

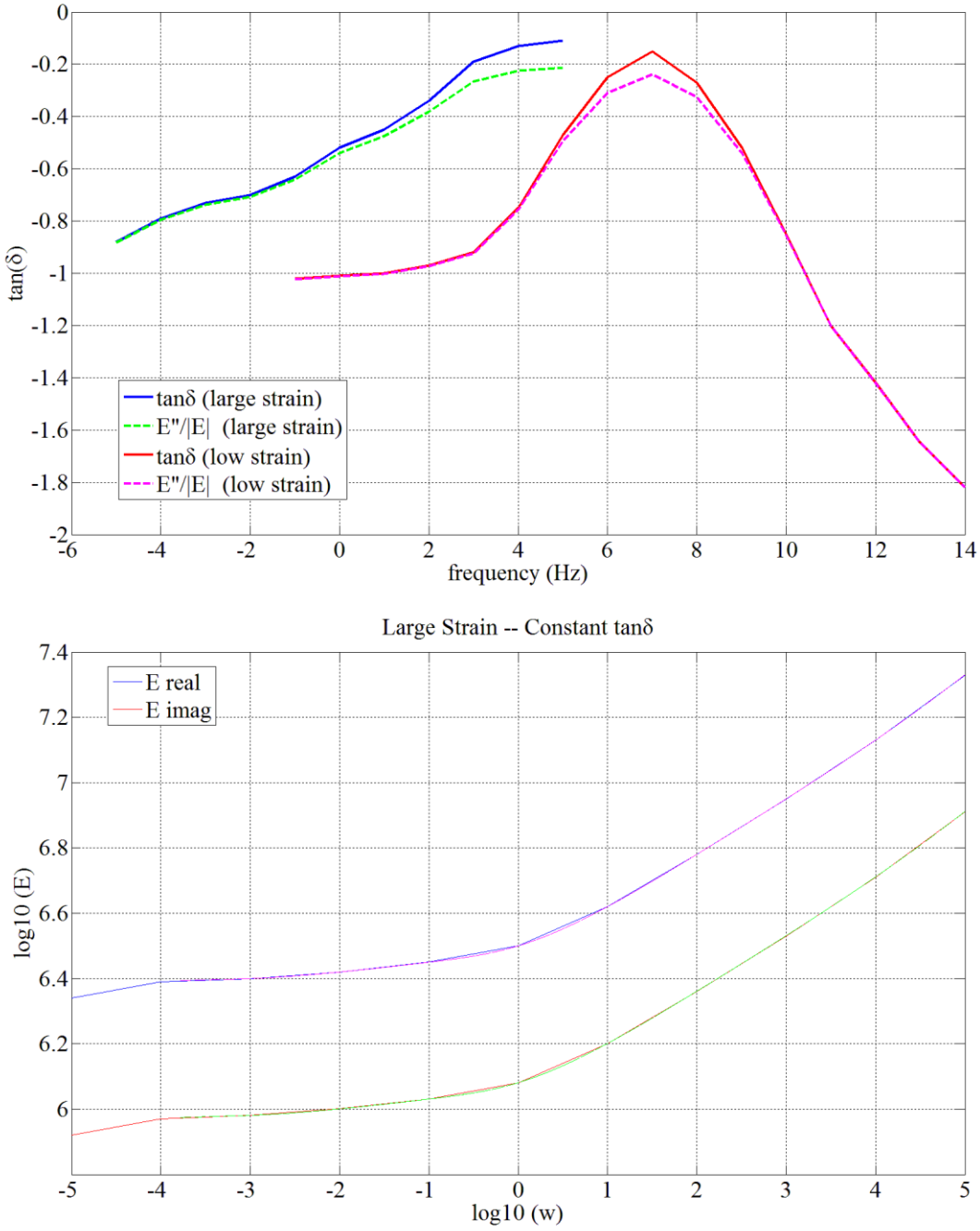

Figure 4-35. Top: $tan\delta$ for low and large strains for a tread compound; Bottom: constant $tan\delta$ for large strain (E" is changed to produce a constant ratio with E').

In Figure 4-36 (Left), for tread compound at large strain on sandpaper, the absolute values of contribution of logarithmic length scale bands to the coefficient of friction is shown for when $tan\delta$ is held constant. To see the differences more distinctly, the results are normalized to the maximum value at each sliding velocity (see Figure 4-36 Right). Although the sequence of the contributions for the different bands is the same at different velocities, the bands are not in order (unlike for linear scale length scale bands). The results reestablish that every decade in length scale is roughly equally important.

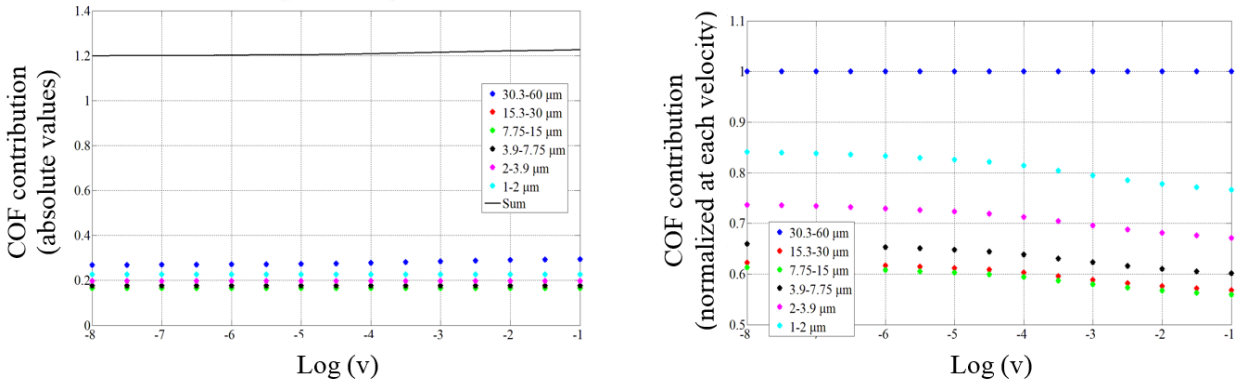

Figure 4-36. Contribution to friction from logarithmic length scale bands with respect to sliding velocity; Left: absolute values of contribution; Right: Normalized-to-max values of contribution.

So far, we have only considered bands of length scales. But now we want to see how friction changes with a continuous spectrum of wavelength. Computationally, the closest thing we can get to a continuous range is a finely discretized array. Again, computationally the friction is zero if we consider a wavevector number as the lower and upper limits of the integrals. Therefore, we consider an infinitesimal boundary around each value and calculate the friction for that (Equation (4-2)),

$$\mu(q) = A \cdot \int_{q-\epsilon}^{q+\epsilon} (B \cdot \int_{q-\epsilon}^{q+\epsilon} C) \qquad (4\text{-}2)$$

Where A, B and C are the integrands of friction prediction equation, which in turn include other integrands.

Persson has stated that the roll-off region gives a negligible contribution to friction. If $D_f > 2$, then the large wavevector region becomes more important and the friction coefficient as a function of the short-distance cut-off bends upwards with increasing q_1 for log-scale q. However, using Equation (4-2) does not yield to that outcome (see Figure 4-37).

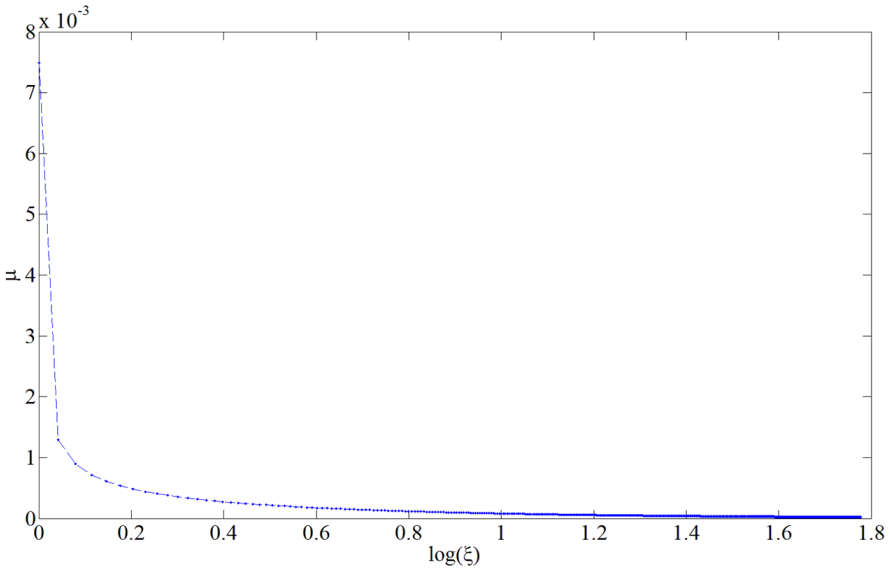

Figure 4-37. Coefficient of friction with respect to continuous linear magnification for tread compound at large strain on sandpaper. The infinitesimal boundary is considered around the linear wavevector values.

We redo the previous simulation, but this time for discretized values of logarithmic wavevectors (Equation (4-3)). In Figure 4-38 we see the expected behavior (the friction coefficient as a function of the short-distance cut-off bends upwards with increasing q_1 for log-scale q).

$$\mu(q) = A \cdot \int_{10^{\log(q)-\epsilon}}^{10^{\log(q)+\epsilon}} (B \cdot \int_{10^{\log(q)-\epsilon}}^{10^{\log(q)+\epsilon}} C) \qquad (4\text{-}3)$$

Where A, B and C are the integrands of friction prediction equation, which in turn include other integrands.

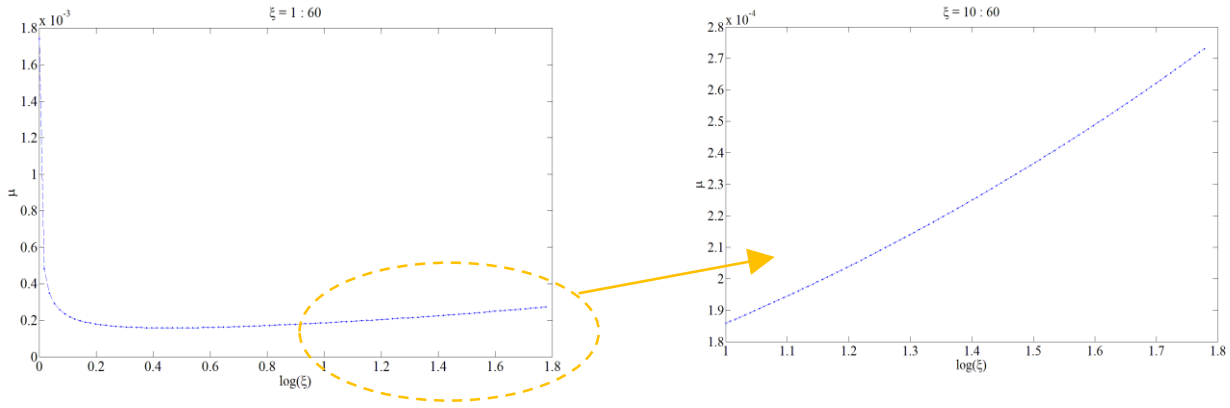

Figure 4-38. Coefficient of friction with respect to continuous logarithmic magnification for tread compound at large strain on sandpaper. The infinitesimal boundary is considered around the logarithmic wavevector values.

Within Persson's framework, friction is very sensitive to the short-distance cut-off wavevector (q_1). As discussed in the previous chapter, q_1 can be measured using a Scanning Electron Microscope. But that's not always a readily available option. q_1 can also be roughly estimated, analytically. But in most cases the result is not accurate enough. However, the contribution from the area of real contact has opposite q-dependency. Furthermore, for wet surfaces at high enough sliding speeds, the contribution from the contact area (adhesion) may be very small, but then the effect of flash heating becomes more important and reduces friction. Thus, adhesion at low velocities, and flash heating at high velocities may make friction less q_1 dependent.

4.4.3 Flash heating

4.4.3.1 TheWLF model – Horizontal shift

The WLF coefficients can be calculated for any reference temperature through frequency and temperature sweep DMA tests and computing the horizontal shift factor for a compound. As an example, in Figure 4-39 the master curves of a tread compound at reference temperatures of $T_0 = 0, 40$ and 80℃ are shifted to $T_0 = 20$℃. That leaves us with four equation and two unknowns, namely the WLF coefficients C_1 and C_2 that were be computed by the least squares method.

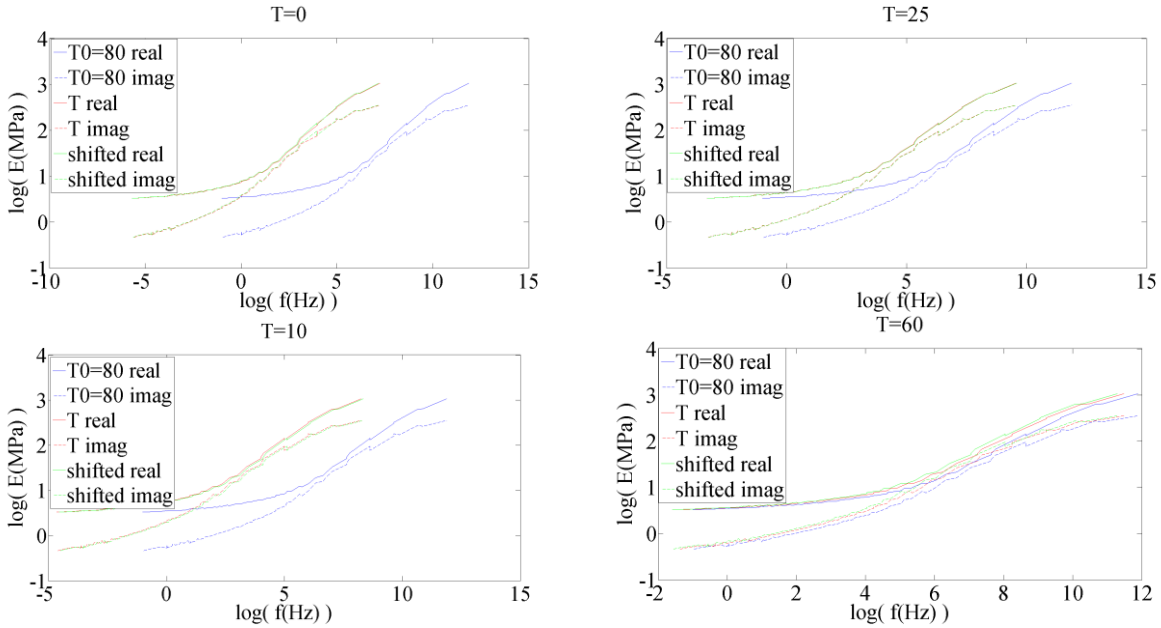

Figure 4-39. Master curves of a tread compound at reference temperatures of $T_0 = 0, 40$ and 80℃ are shifted to $T_0 = 20$℃.

4.4.3.2 Flash temperature results

Up to this point, all the simulation have been for hysteresis friction without considering the flash heating effect. In this section, first we investigate the effect of speed and temperature on friction.

For an all-season tread compound at low strain on 240-girt sandpaper, Figure 4-40 illustrates how the flash temperature increases with velocity. Changing ξ_m (see Equation (3-46)) between 2 to 5 only slightly changes the subsequent flash temperature.

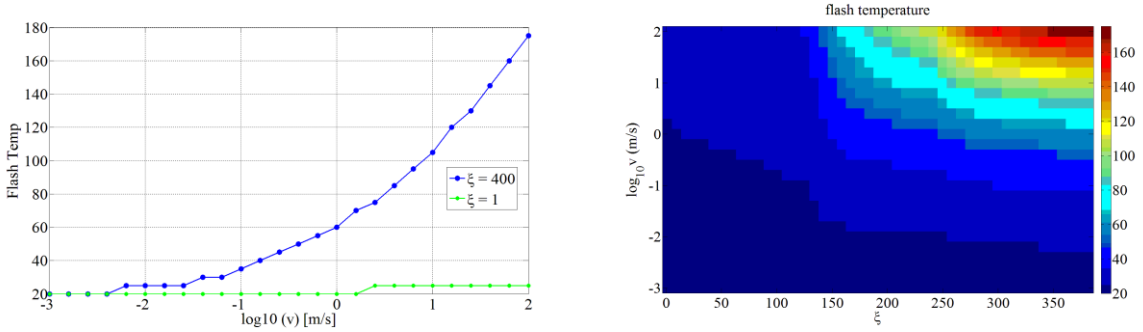

Figure 4-40. Instantaneous temperature rise in the contact of a tread compound at low strain and sandpaper; Left: Flash temperature with respect to sliding velocity for the minimum and maximum magnification values; Right: Scaled image of flash temperature with respect to sliding velocity and magnification.

In Figure 4-41, we see how friction changes with sliding velocity, with and without flash temperature. The cold and hot branches start to split at around $v = 10^{-3} - 10^{-2}\, m/s$. At slower speeds, the heat generated in the contact is diffused without increasing the temperature. In the rubbery region, the cold friction seems to always increase with velocity. However, the hot friction can either increase, decrease or stay almost unchanged, for specific ranges of velocity, depending on the rubber compound properties. Adhesion is yet to be included in the simulations.

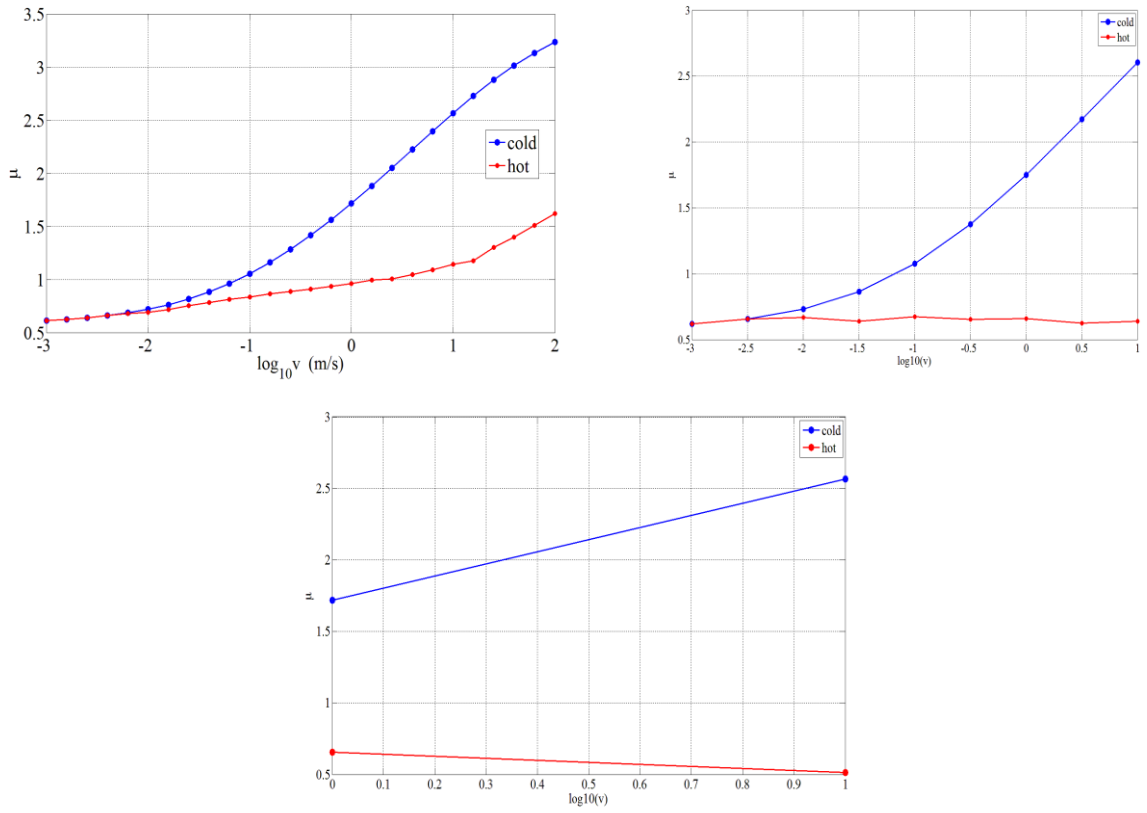

Figure 4-41. Cold and hot coefficient of friction with respect to sliding velocity for tread compound at low strain and sandpaper. From left to right, by tweaking the WLF parameters, hot friction increases, stays level, and decreases with velocity, respectively.

Next, we investigate the effect of nominal pressure on friction. Some experiments in the literature suggest that the coefficient of friction changes significantly with pressure. Nevertheless, we have not been able to replicate that in our simulations based on Persson's and Klüppel's theories. In Figure 4-42, we can see how the real contact area increases with pressure for when we do/don't consider flash heating. Yet, the simulated rate of friction reduction with pressure is not as expected (see Figure 4-43). The equation we currently used to estimate RCA is simplified to work for the conditions where pressure is of a lower order

than '$E(0) \approx 1\ MPa$'. Therefore, it might not hold for $P = 10MPa$ which is used in our simulations. Nevertheless, based on experimental results, we expected to see a notable decrease in friction with pressure, even for the practical operational range of footprint contact pressures that is of a lower order than $E(0)$. Persson has mentioned that on dry rough road surfaces in the typical pressure range in tire applications, the friction coefficient is independent of the contact pressure, assuming constant temperature [11]. But the experiments indicate otherwise. Compared to simulations, we have not augmented the effect of adhesion yet.

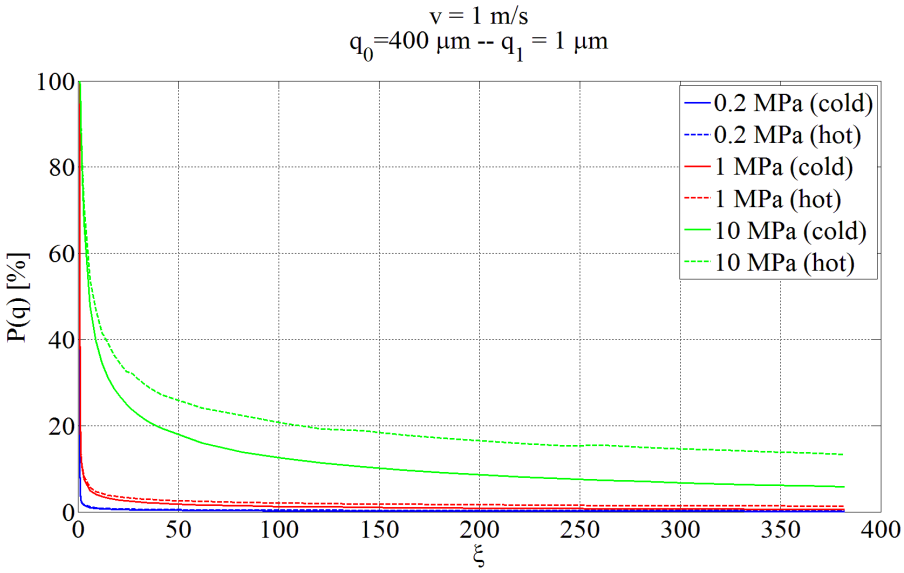

Figure 4-42. Tread compound at large strain on sandpaper; The real contact area with respect to magnification, for three nominal pressures of 0.2 (passenger tire), 1, and 10 Mpa. Results are presented for cold and hot friction.

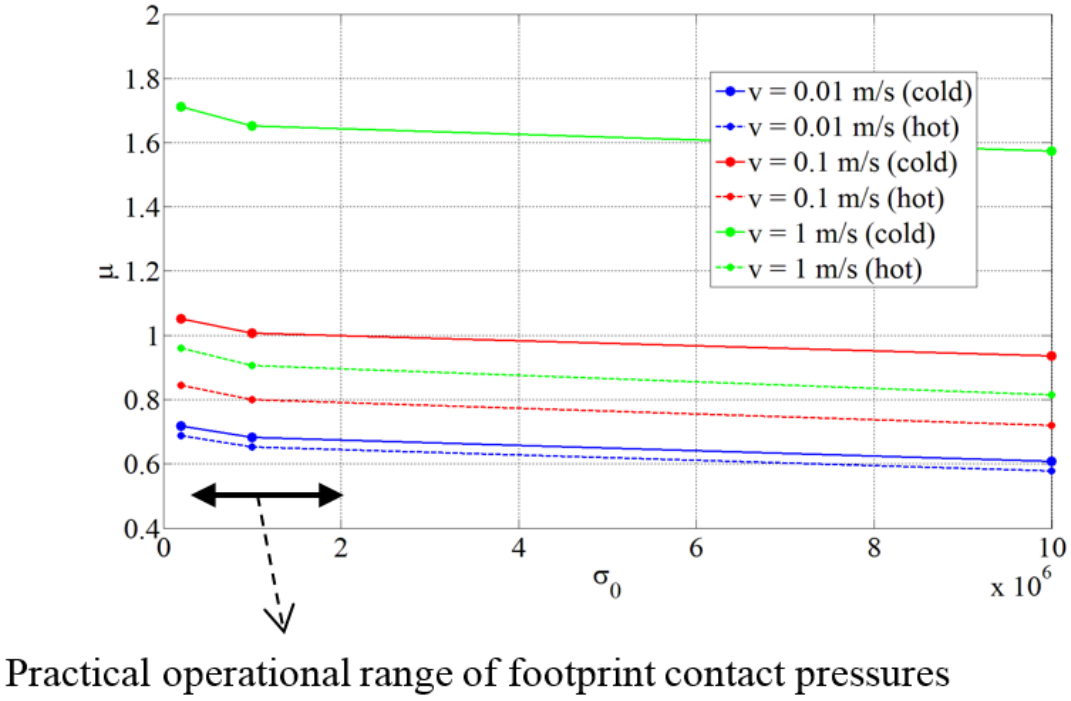

Figure 4-43. Tread compound at large strain on sandpaper; The coefficient of friction with respect to nominal pressure, for three sliding velocities of 0.01, 0.1, and 1 m/s. Results are presented for cold and hot friction. The operational range of contact patch pressure is indicated.

Figure 4-44 shows that the flash temperature only very slightly changes with pressure for different magnification levels. Experiments suggest that it is indeed not the case, and that temperature increases with pressure, which in turn decreases friction.

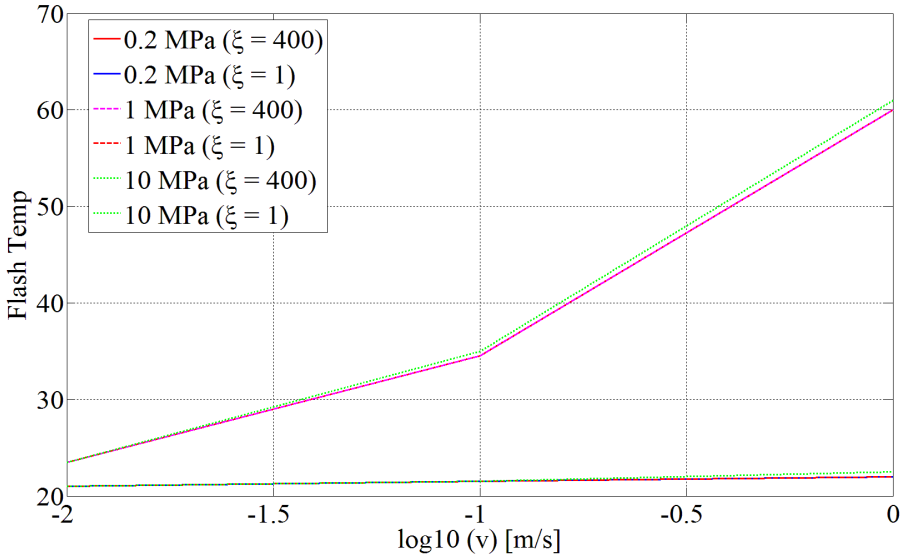

Figure 4-44. Tread compound at large strain on sandpaper; Flash temperature with respect to sliding velocity, for three nominal pressures of 0.2 (passenger tire), 1, and 10 Mpa. Results are presented for cold and hot friction, and for the minimum and maximum magnification levels.

4.4.4 Comparison of theory with outdoor experiments

The real area of contact between a tire and the road surface is typically about only 1% of the nominal contact area [12]. Therefore, the adhesion component of rubber friction is small compared to the hysteresis contribution at high slip velocities. The results presented here are for hysteresis friction only. The tread compound used is from an all-season passenger tire, and has a glass transition temperature of $T_g = -33.1℃$.

In Figure 4-9, the surface roughness power spectra for the five different highway surfaces are shown. They were calculated from the profile measurement by the OGP Digital Range Sensor System DRS-8000 with a lateral resolution of 45 μm. The power spectrum for each surface is an average over the power spectra of all the individual line scan measurements on that surface.

One can realize from the figure that for every surface, the evaluation length has been long enough to capture the roll-off region and all the wavelengths that contribute to friction. As discussed before, for road surfaces, the short-distance cut-off wavevector is usually about $1 - 10\ \mu m$. Yet, the horizontal resolution of the profile data used in this study is $45\ \mu m$, which means that the smallest wavelength that can be processed is $90\ \mu m$ (Nyquist wavelength). However, as expected for fractal surfaces, the power spectrum curve on a log-log scale demonstrates a linear behavior for wavevectors larger than the roll-off wavevector. Therefore, in order to obtain more accurate friction predictions, the spectrum is linearly extrapolated to $10\ \mu m$.

The fractal dimension can be calculated from the slope of the log-log power spectrum curve. For surfaces 14d1, 15d1, 26d1, 29d1 and 30b1, the fractal dimension is 2.34, 2.27, 2.39, 2.29 and 2.28, respectively. These values are consistent with the average fractal dimension (= 2.2 – 2.4) of road surfaces reported in the literature. A larger fractal dimension could roughly mean more microtexture in the roughness.

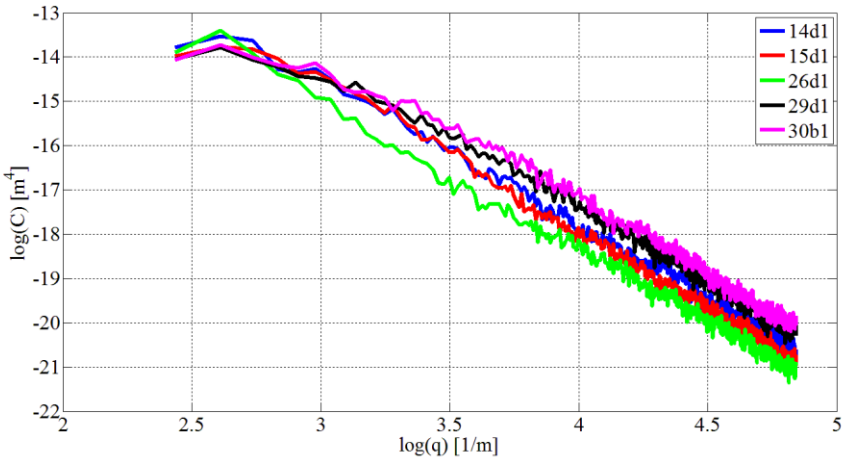

Figure 4-45. Power spectral density of surface roughness for the five fractal surfaces. The measurements were carried out using the OGP DRS-8000, with a lateral resolution of $45\ \mu m$. The power spectrum for each surface is an average over the power spectra of all the individual line scan measurements on that surface.

Figure 4-62 illustrates the coefficient of friction as a function of sliding velocity for a tread compound on the five fractal surfaces (calculated using Persson contact mechanics). The effect of flash temperature is not included. For each profile, calculations are done assuming the short-distance cut-off wavelength to be $10\ \mu m$ and the nominal pressure to be $\sigma_0 = 0.2\ MPa$. Hysteresis friction, when not accounting for the effect of flash heating, typically has a peak that corresponds to the peak of $tan\delta$ $(= Im\big(E(\omega)\big)/\ Re\big(E(\omega)\big))$. Since only the rubbery region is considered, the coefficient of friction increases with sliding velocity. Roughly speaking, the dynamic friction coefficient increases as the surface gets rougher (FN increases).

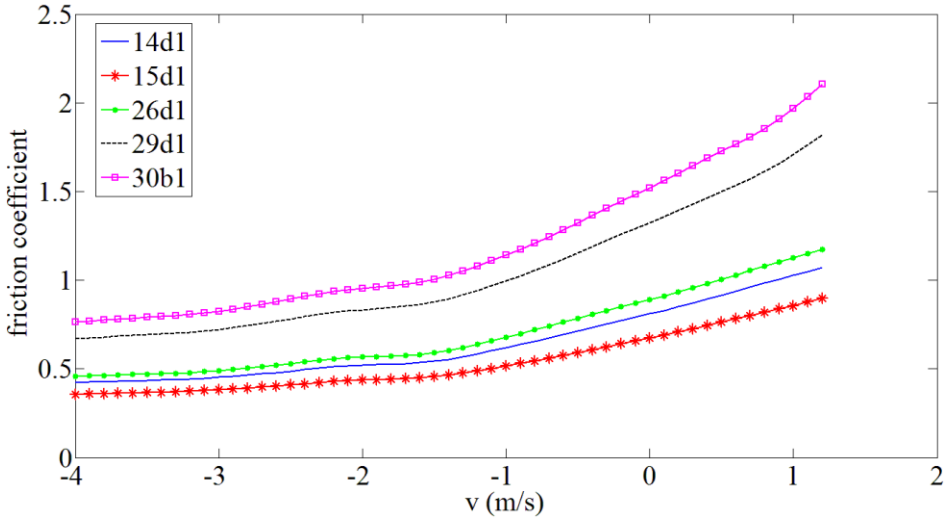

Figure 4-46. Coefficient of friction with respect to sliding velocity for a tread compound on the five fractal surfaces. For all simulations, $\lambda_1 = 10\ \mu m$ and $\sigma_0 = 0.2$ MPa.

The results presented next include the flash temperature from the hysteresis friction. The term flash temperature refers to a local and sharp temperature rise occurring in the tire–road asperity contact regions

during slip. In Figure 4-47, for the same tread compound and the five fractal surfaces under study, the cold (without flash temperature) and hot (with flash temperature) friction coefficient values at the sliding velocity of $40\,mph$ are plotted with respect to the friction numbers (FN). The cold friction coefficient values are fairly correlated with the friction measurements ($r^2 = 0.86$). A better correlation is observed for the hot friction coefficient values ($r^2 = 0.91$), which are expected to be closer to the real friction coefficients. Adding the contribution from adhesion would possibly improve the correlations.

If hot friction was calculated for a range of velocities, it could be observed that the cold and hot branches start to split at around $v = 10^{-3} - 10^{-2}\,m/s$. At slower speeds, the heat generated in the contact is diffused without increasing the temperature. In the rubbery region, the cold friction always increases with velocity. However, the hot friction can increase, decrease, or stay almost unchanged, for specific ranges of sliding velocity, depending on the rubber compound properties.

The footprint flash temperature values for the five surfaces at $40\,mph$ are presented in Figure 4-48. Typically, rougher surfaces with larger friction coefficients generate more heat and higher flash temperatures.

The rubber background temperature is $20\,℃$ for all five surfaces. For surfaces 14d1, 15d1, 26d1, 29d1 and 30b1, the flash temperature at the maximum magnification level (i.e. the temperature about 10 μm below the rubber surface) is 111, 92, 108, 135 and $152\,℃$, respectively (i.e. about $70 - 130\,℃$ above the rubber background temperature).

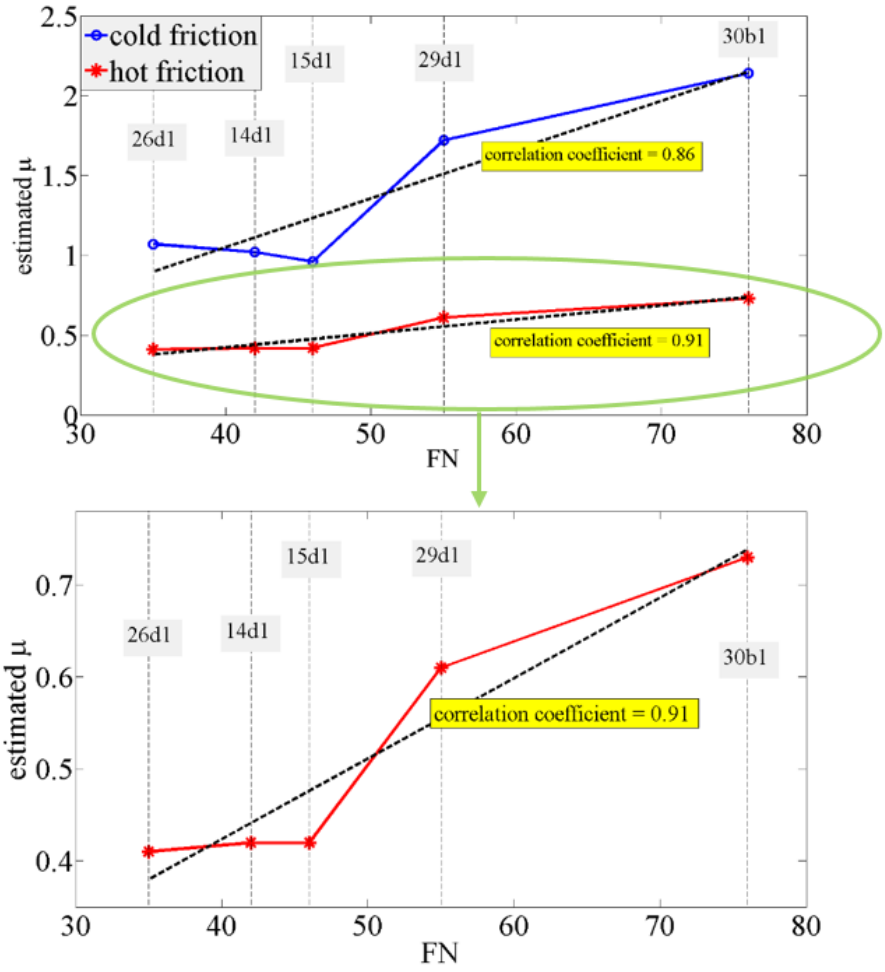

Figure 4-47. Cold (without flash temperature) and hot (with flash temperature) friction coefficient values at the sliding velocity of 40 mph with respect to the friction numbers (FN), for a tread compound and the five fractal surfaces. The correlation coefficient between cold friction and FN is $r^2 = 0.86$. The correlation coefficient for hot friction with respect to FN is $r^2 = 0.91$.

On the other hand, the temperature increase a few millimeters below the surface (corresponding to the magnification $\zeta = 1$) is just a few degrees. During steady sliding, the temperature in the whole rubber block will increase continuously with increasing time, but this effect is not included in this study, unless one allows for the background temperature T_0 to increase with time.

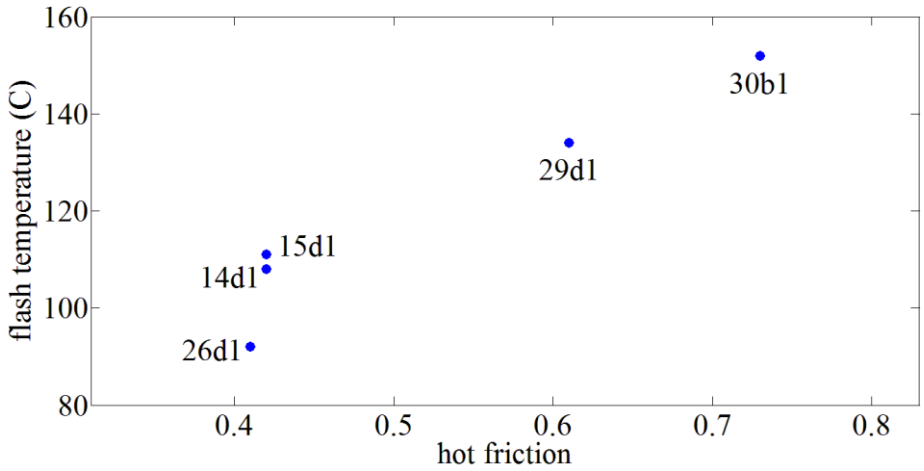

Figure 4-48. The flash temperature at the surface of rubber for the sliding velocity of 40 mph. The rubber background temperature is 20 C. The flash temperature at the maximum magnification rises, as the surface gets rougher and the sliding friction increases.

4.5 Klüppel

4.5.1 One scaling regime

For these simulations, roughness data for rough granite, and the master curves of Carbon Black filled Styrene Butadiene Rubber 5025 are used. A linear approximation of varying minimal length scale, λ_{min}, is considered. Recall that λ_{min} is velocity dependent and imposes the dominance of macro-texture at high sliding velocities. The real area of contact A_c at a length scale λ_{min} with a two-scaling ranges approach will be estimated in the future. The effect micro- and macrotexture at low and high sliding velocities was discussed in previous sections.

The master curve for carbon black filled S-SBR 5025 is shown in Figure 4-49. The green line represents the viscous modulus sweep, and black dotted line signifies the elastic modulus sweep at the minimum

temporal frequency for the velocity range in the simulation. For rough granite with a one scaling range approach, the power spectral density is shown in Figure 4-50. The simulated hysteresis friction for carbon black S-SBR 5025 on rough granite is plotted in Figure 4-51, for sliding velocities from $v = 10^{-5}$ to $10^{1}\, m/s$. As shown in Table 4-7, there is good agreement between our predictions and the results reported by Klüppel.

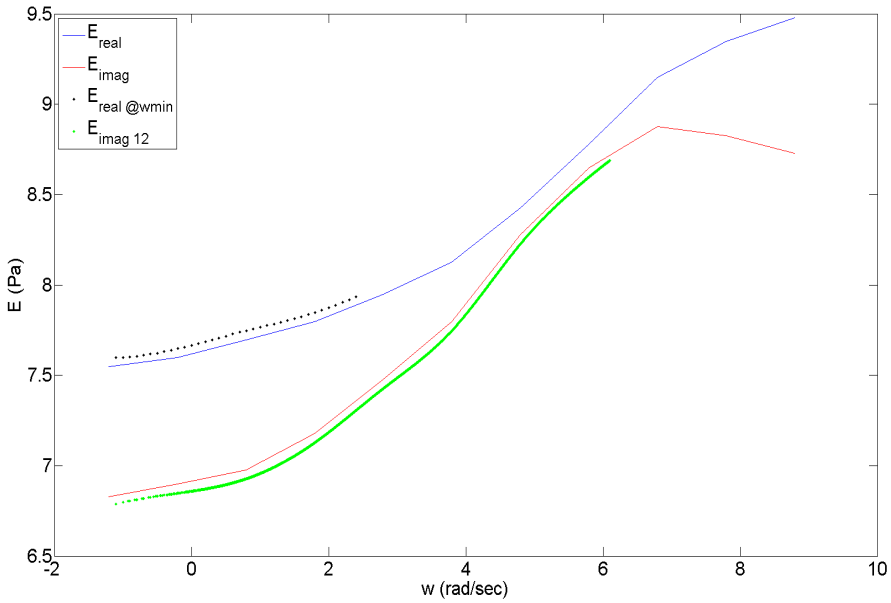

Figure 4-49. Master curve for carbon black filled S-SBR 5025 at a reference temperature $T_0 = 23°C$. Strain amplitude $\epsilon = 0.5\%$. The dotted black line is the real modulus at minimum frequency for the simulation velocity range. The offsets are for the sake of distinguishability.

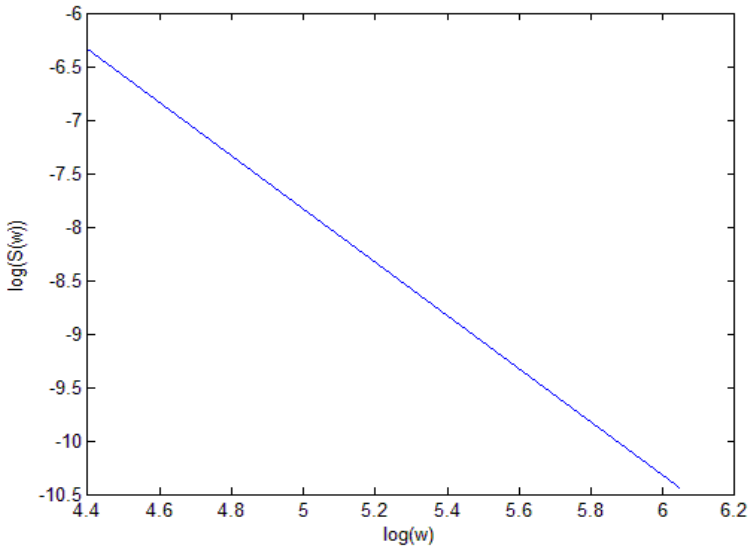

Figure 4-50. Power spectral density $S(\omega)$ for rough granite with a one scaling range approach.

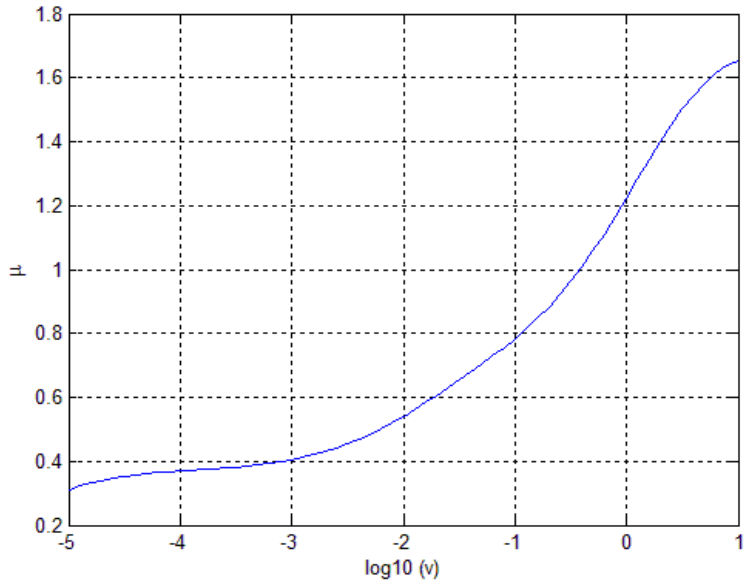

Figure 4-51. Simulated hysteresis friction for carbon black S-SBR 5025 on rough granite. Nominal normal load σ_0 = 12.3 kPa.

Velocity (m/s)	μ (Klüppel)	μ (current research)
10^{-5}	0.33	0.32
10^{-4}	0.37	0.37
10^{-3}	0.46	0.41
10^{-2}	0.64	0.55
10^{-1}	0.88	0.81

Table 4-7. Comparison between Klüppel's simulations and the coefficient of friction estimations in the current research, at different sliding velocities, for carbon black S-SBR 5025 on rough granite.

4.5.2 Two scaling regimes; constant minimum wavelength

In the two scaling regimes approach, a transition wavelength is selected that separates the macrotexture ($S_1(\omega)$) and the microtexture ($S_2(\omega)$) length scales. In Figure 4-52, the power spectral density has two different slopes and fractal dimensions for the scaling regions. Figure 4-53 shows the master curve for carbon black filled S-SBR 5025. The magenta and the yellow lines correspond the macrotexture and microtexture scaling regions respectively. λ_{min} is considered to be constant here for all sliding velocities.

In Figure 4-54, simulated hysteresis friction for carbon black S-SBR 5025 on rough granite vs. sliding velocity is shown. We didn't expect to get the same results as Klüppel, since we were holding λ_{min} constant. The next step is to use a varying λ_{min} to see how that affects the outcome.

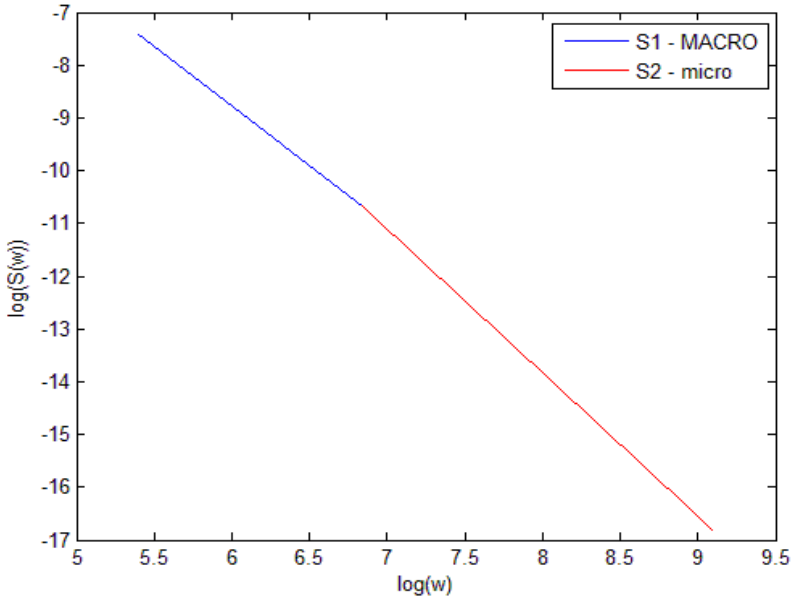

Figure 4-52. Power spectral density of rough granite. A transition wavelength is selected that separates the macrotexture ($S_1(\omega)$) and the microtexture ($S_2(\omega)$) length scales.

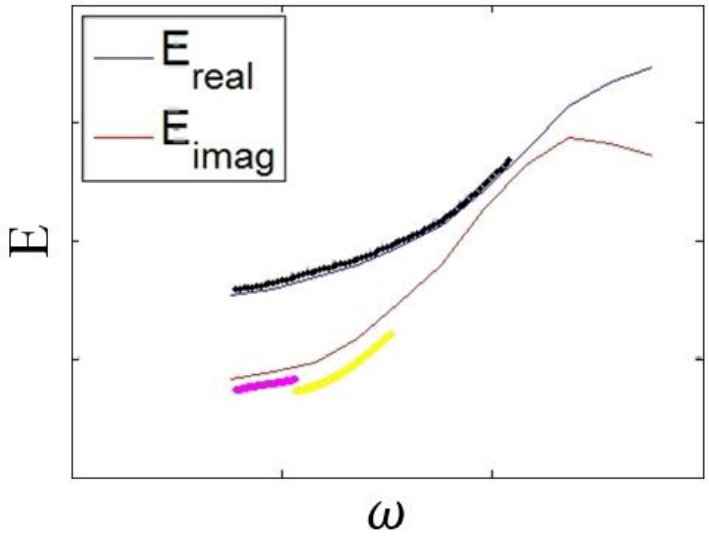

Figure 4-53. Master curve for carbon black filled S-SBR 5025 at a reference temperature $T_0 = 23°C$. Strain amplitude $\epsilon = 0.5\%$. The dotted black line is the real modulus at minimum frequency for the simulation velocity

range. The offsets are for the sake of distinguishability. The magenta and the yellow lines correspond the macrotexture and microtexture scaling regions respectively.

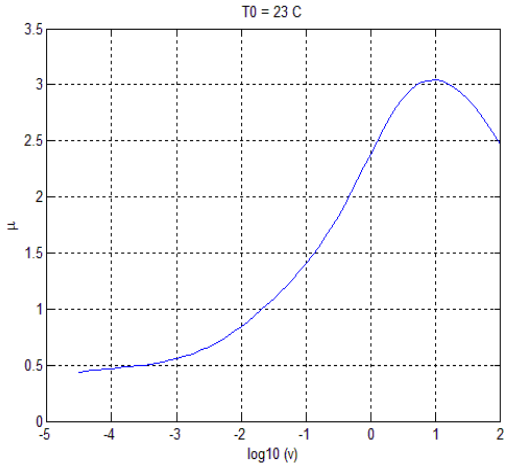

Figure 4-54. Simulated hysteresis friction for carbon black S-SBR 5025 on rough granite vs. sliding velocity. Nominal normal load σ_0 = 12.3 kPa, λ_{min} is considered to be constant, and $T_0 = 23°C$.

4.5.3 Two scaling regimes; Varying minimum wavelength

We carry out the simulations again for S-SBR 5025 on rough granite, for two scaling regimes, but this time with varying λ_{min}. Figure 4-55 shows how λ_{min} increases with sliding velocity. After some velocity, λ_{min} is larger than λ_2 (transition from microtexture length scales to macrotexture), and microtexture is practically not effective anymore. Figure 4-56 shows the master curve for carbon black filled S-SBR 5025. The magenta-green line corresponds to the macrotexture wavelengths, as velocity increases and higher frequencies are excited. The black-yellow line signifies the microtexture wavelengths and only extends to the frequency that corresponds to the velocity where the minimum wavelength surpasses the transition wavelength. In Figure 4-57, simulated hysteresis friction for carbon

black S-SBR 5025 on rough granite vs. sliding velocity is shown. The shape and the magnitude of the curve is close to Klüppel's simulation data.

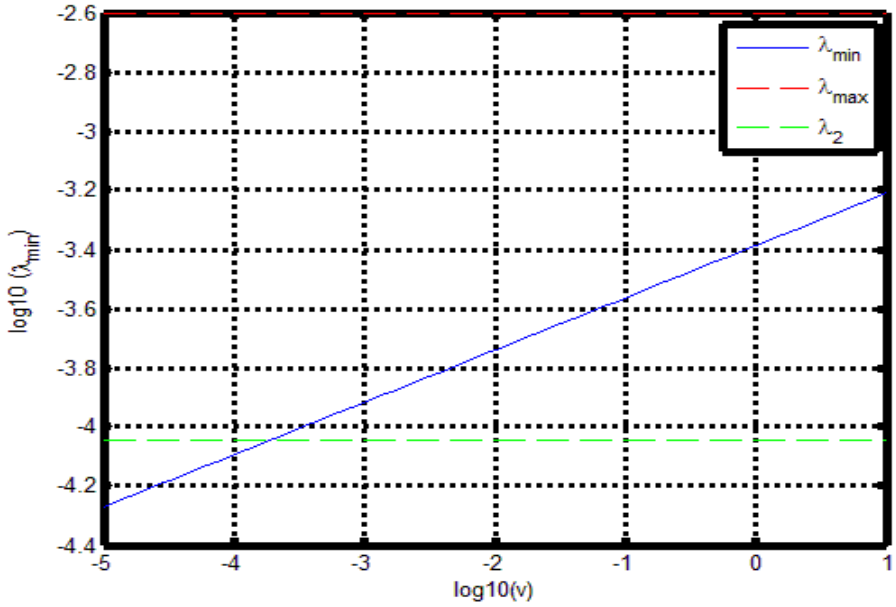

Figure 4-55. Linear approximation λ_{min} vs. sliding velocity (blue line). The green dashed line denotes the transition wavelength from microtexture to macrotexture length scales. The red dashed line is the maximum wavelength in the roughness which is the upper limit for λ_{min}.

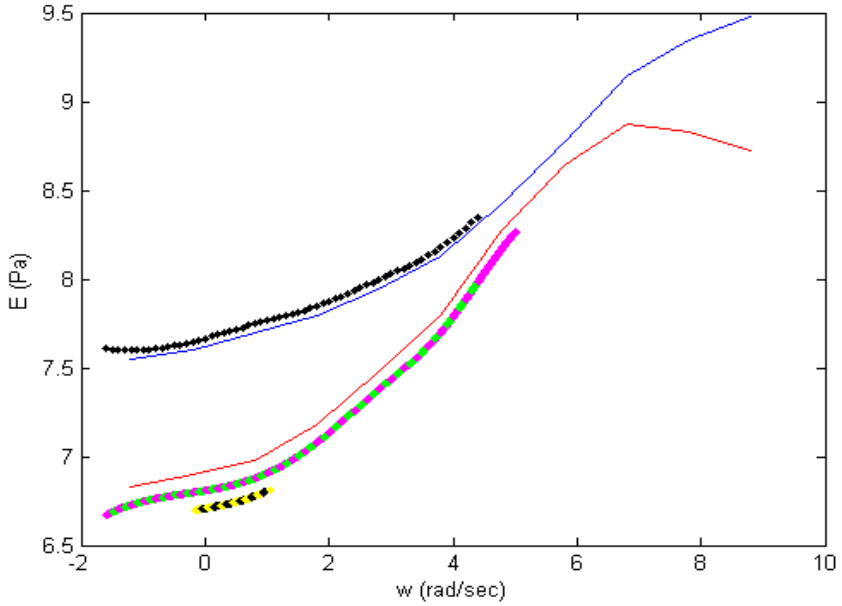

Figure 4-56. Master curve for carbon black filled S-SBR 5025. The dotted black line is the elastic modulus at the minimum frequency for each sliding velocity increment. The magenta-green line corresponds to the macrotexture wavelengths, as velocity increases and higher frequencies are excited. The black-yellow line signifies the microtexture wavelengths and only extends to the frequency that corresponds to the velocity where the minimum wavelength surpasses the transition wavelength.

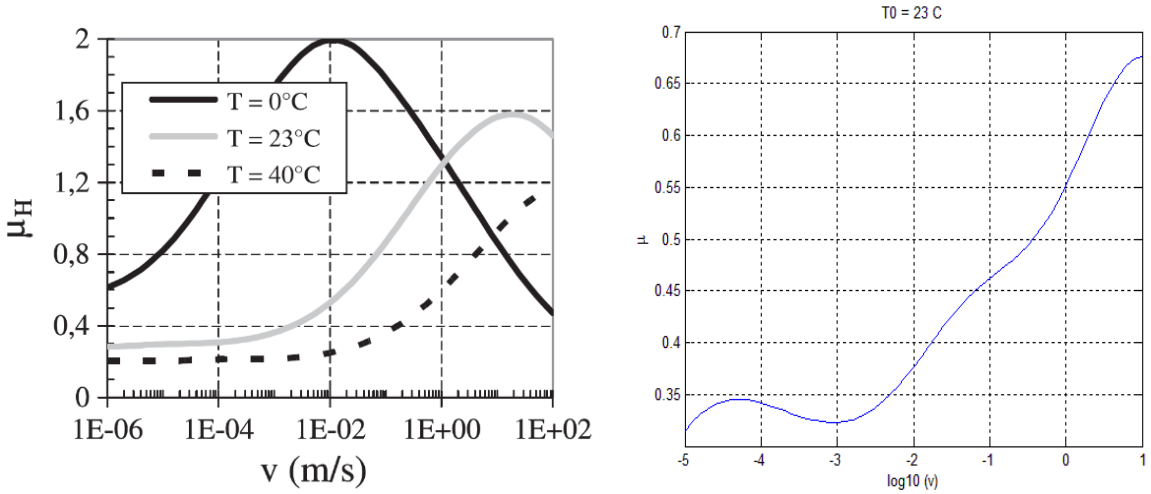

Figure 4-57. Simulated hysteresis friction for carbon black S-SBR 5025 on rough granite vs. sliding velocity. Nominal normal load σ_0 = 12.3 kPa; Left: Results reported by Klüppel; Right: Current research considering varying λ_{min}, $T_0 = 23°C$ (goal was to match the grey curve in figure 'a').

4.5.4 Mean Penetration Depth

The ratio '$excited\ layer\ thickness/mean\ penetration\ depth$' is reported to be $1.1 - 2.6$ for Carbon Black filled Styrene Butadiene Rubber on asphalt at a normal load of $12\ kPa$. This ratio can increase with pressure; for a passenger tire, typical pressure is $0.3\ MPa$, and it is $0.8\ Mpa$ for truck tire. With these values, one obtains the penetration depth as $0.03\ mm$ and $0.08\ mm$, respectively [4]. These values are below the rms roughness of typical road tracks ($0.1\ mm$), which represents an upper boundary for the penetration depth. The peak-to-peak height for typical road tracks is $1 - 2\ mm$.

We are studying two other cases here: 1) a very rough track surface; 2) a very smooth sandpaper surface. Figure 4-58 shows a very rough road surface (peak-to-peak height $\approx 8\ mm$), with the penetration depth highlighted for different sliding velocities. The surface asperities penetrate the rubber deeper at lower speeds.

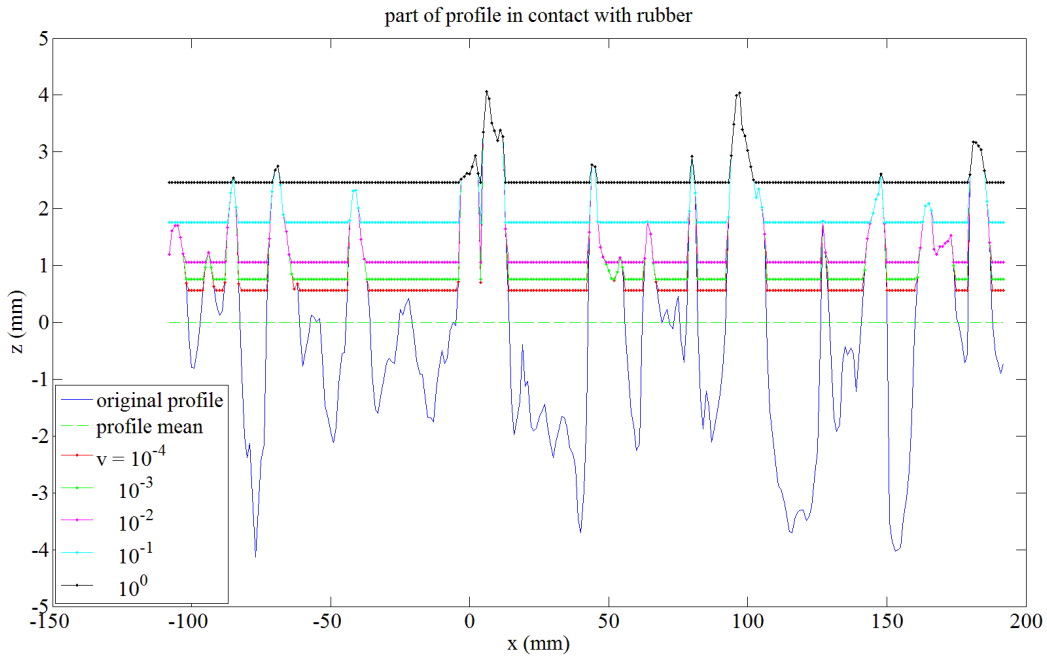

Figure 4-58. A very rough road surface, with the mean penetration depth highlighted for different sliding velocities.

For a tread compound at large strain on sandpaper, the surface is characterized using both Klüppel's and Persson's theories (see Figure 4-59). The parameters extracted from each method are in agreement.

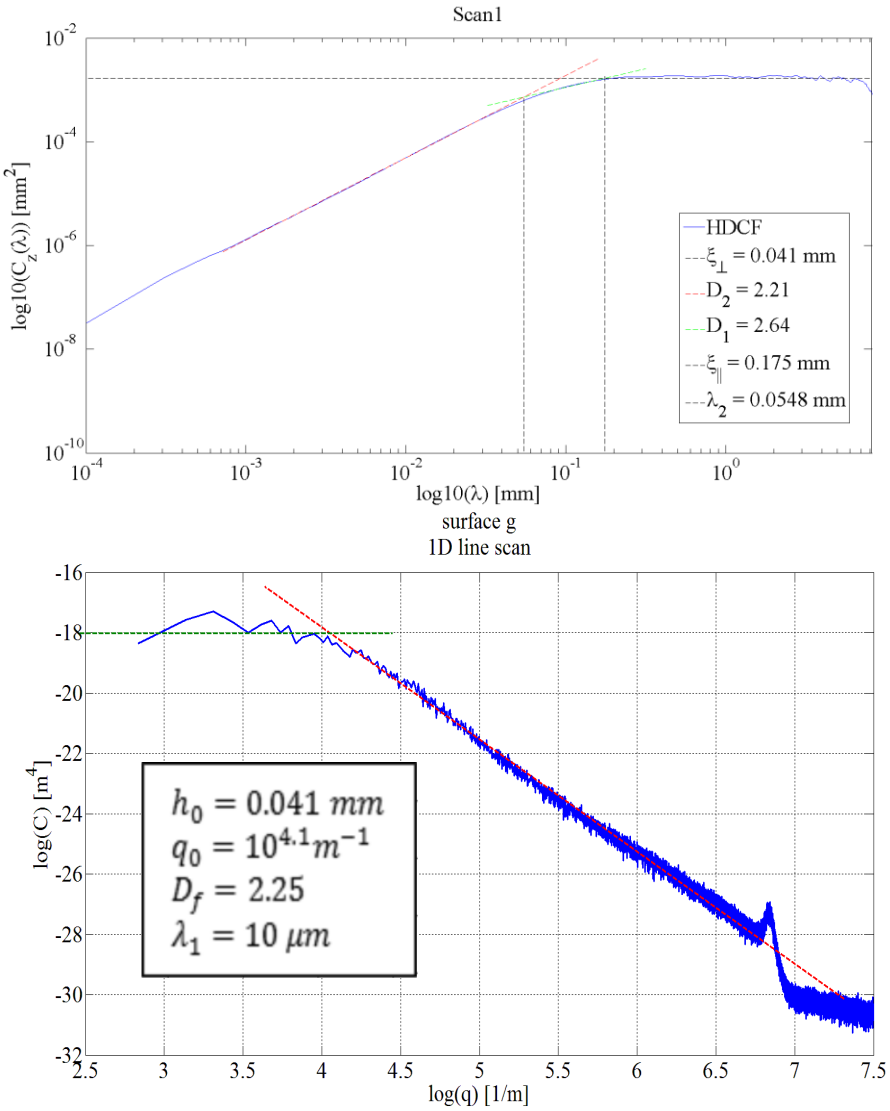

Figure 4-59. Characterization of the sandpaper profile; Top: HDCF (Klüppel). Bottom: PSD (Persson).

In Figure 4-60, hysteresis friction prediction is illustrated with respect to sliding velocity, based on Persson and Klüppel's theories. Good agreement is seen here, as well.

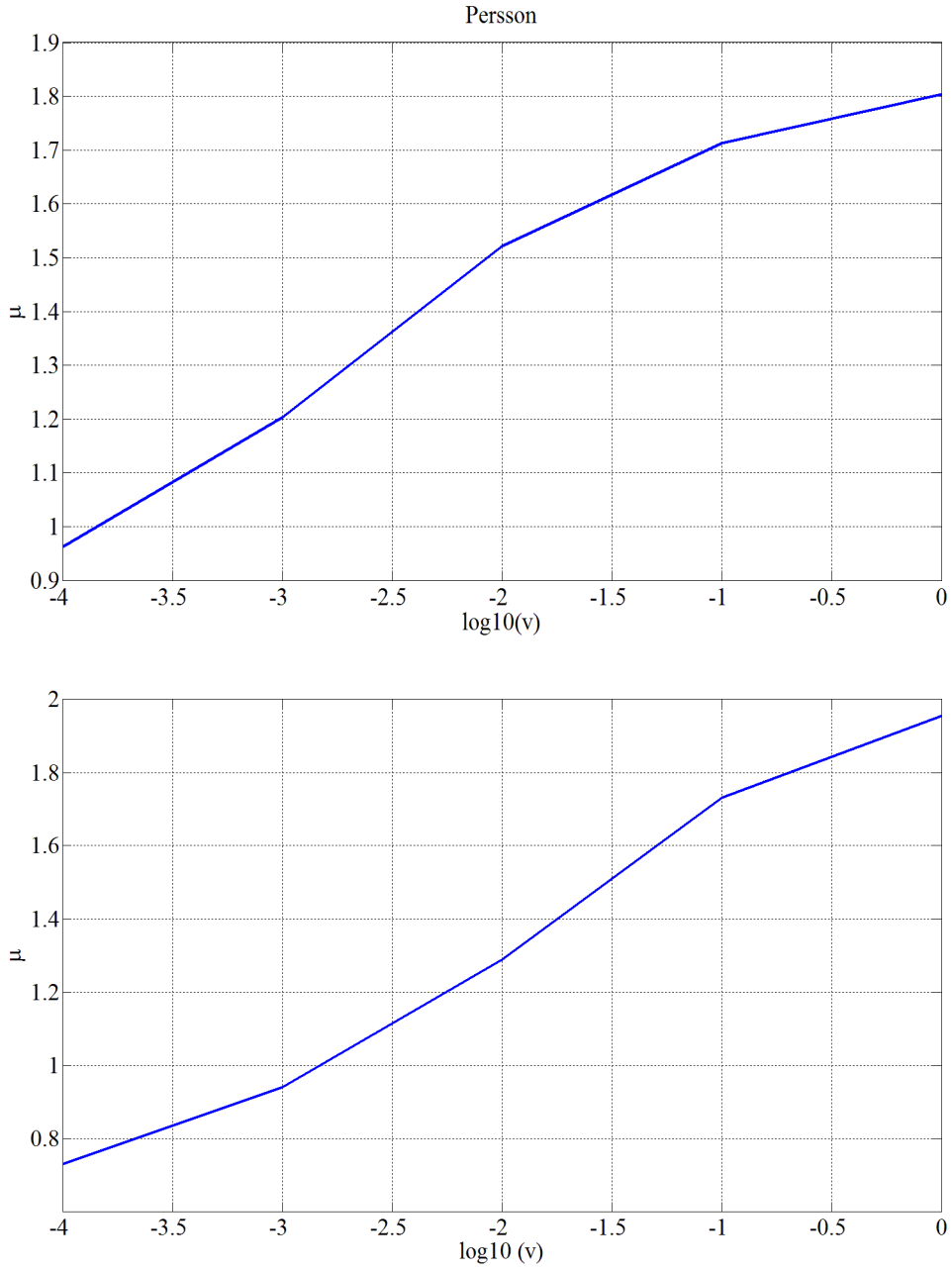

Figure 4-60. Simulated coefficient of friction with respect to sliding velocity, for a tread compound at large strain on sandpaper. Top: Persson's theory; Bottom: Klüppel theory.

Figure 4-61 illustrates the smooth sandpaper surface's profile (peak-to-peak height $\approx 0.06\,mm$), with the penetration depth highlighted for different sliding velocities. As expected, the surface roughness asperities penetrate the rubber deeper at lower sliding velocities.

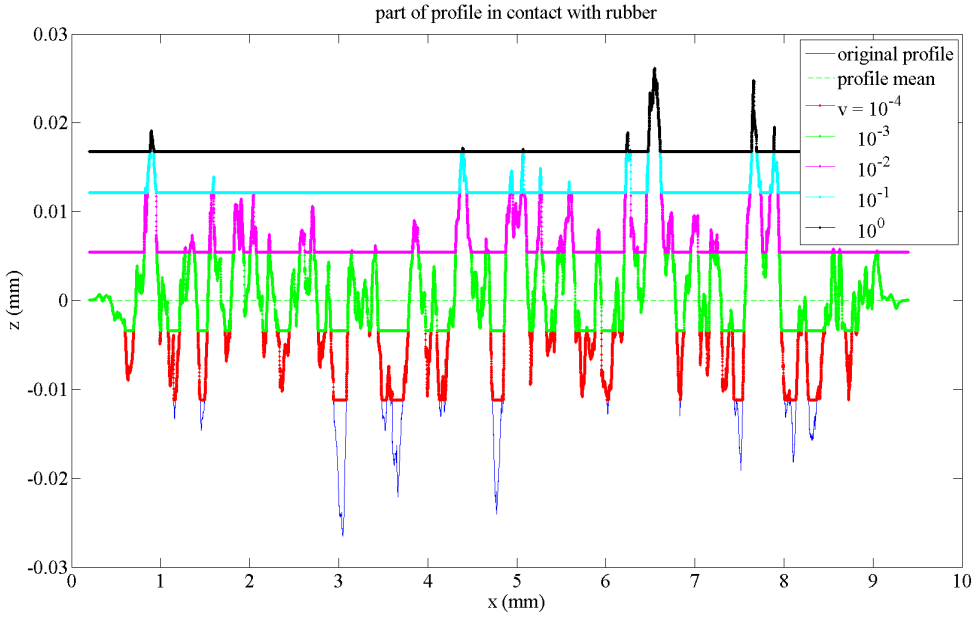

Figure 4-61. Smooth sandpaper surface's profile (peak-to-peak height $\approx 0.06\,mm$), with the penetration depth highlighted for different sliding velocities.

In current practice, the thickness of the excited layer of rubber is seemingly estimated through adaptations of theory with friction measurement data.

4.6 Inclusive friction model; comparison of simulations with indoor experiments

Figure 4-62 illustrates the simulated and experimental friction coefficient values as a function of sliding velocity for a summer tire tread compound on 120-grit sandpaper. For each profile, calculations are done assuming the nominal pressure to be $\sigma_0 = 0.4\,MPa$ (typical inflation pressure for passenger car tires), and the background temperature $T_0 = 20\,C$. In Figure 4-62-a, the cold (without flash temperature) and hot (with flash temperature) hysteresis friction coefficient values are shown with respect to sliding velocity. Also, the hot hysteresis friction coefficients for the macro- and microtexture scaling regimes, as well as the sum of hot hysteresis friction coefficients of the macro- and microtexture regions are plotted. In Figure 4-62-b, the adhesive contribution to friction coefficient in the real contact area at the magnification $\zeta = q_1/q_0$ is plotted. The total hot friction coefficients (hysteresis + adhesion) for one and two scaling regimes are shown, as well. The red dots represent the measured friction coefficients at room temperature.

The cold and hot branches of hysteresis friction start to split at around $v = 10^{-2}\,m/s$. At slower speeds, the heat generated in the contact is diffused without increasing the temperature. In the rubbery region (before $v \approx 10^{2}\,m/s$), the cold friction always increases with velocity. Adding the contribution from adhesion, the effect of flash heating, and implementing the two regimes approach, all improve the correlation with the experimental data.

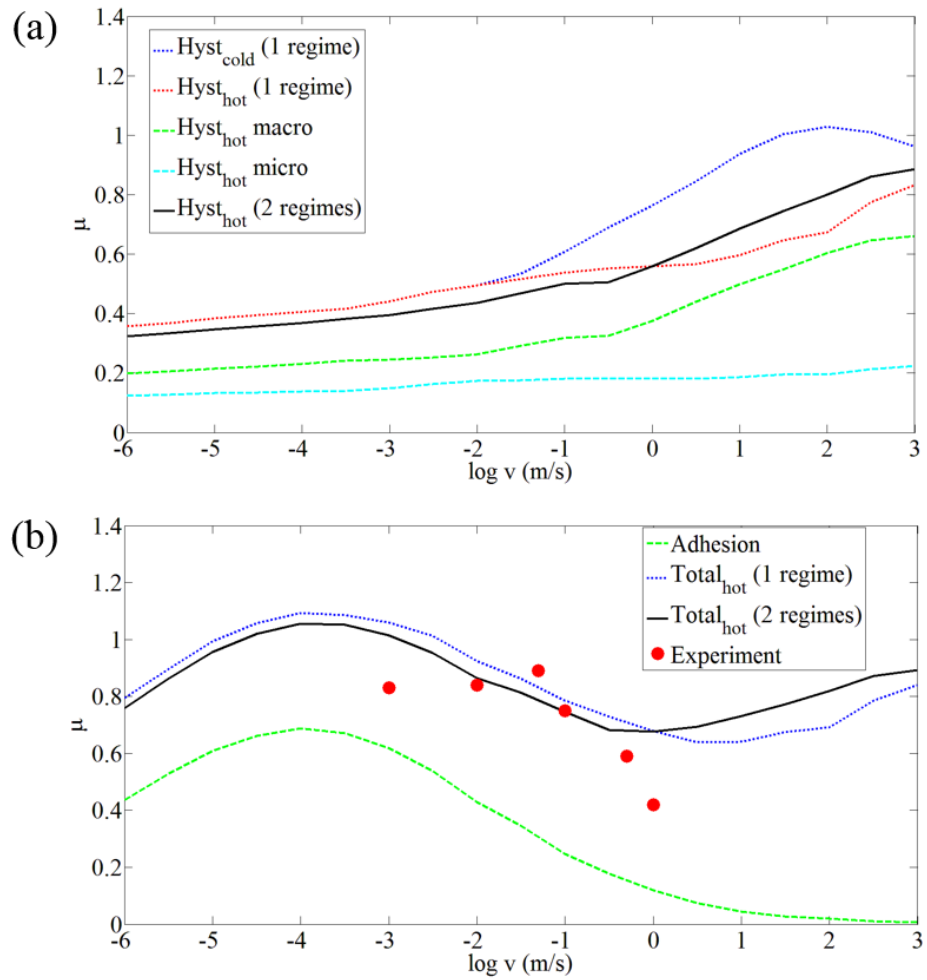

Figure 4-62. Simulated and experimental coefficient of friction with respect to sliding velocity for a summer tire tread compound on 120-grit sandpaper. For all simulations, the nominal pressure $\sigma_0 = 0.4$ MPa and the background temperature $T_0 = 20\,C$ (a): The dotted lines show the cold and hot hysteresis friction coefficient values. The dashed lines represent the hot hysteresis friction coefficients for the macro- and microtexture scaling regimes. The solid line is the sum of hot hysteresis friction coefficients of the macro- and microtexture regions; (b): The dashed line is the adhesive contribution to friction coefficient in the real contact area at maximum magnification $A(q1)$. The dotted line shows the total hot friction coefficient (hysteresis + adhesion) for one scaling regime. The solid line is the total hot friction coefficient when two scaling regions are considered. The red dots represent the measured friction coefficients at room temperature (all the other depicted curves the results of simulation).

The footprint flash temperature is presented in Figure 4-63. The rubber background temperature is $T_0 = 20\,C$. The flash temperature at maximum magnification (i.e. the temperature about $6\,\mu m$ below the rubber surface) is $\approx 70\,C$ (about $50\,C$ above the rubber background temperature). On the other hand, the temperature increase a few millimeters below the surface (corresponding to the magnification $\zeta = 1$) is just a few degrees. The effect of the temperature increase in the whole rubber block with time [107] is not included in this work.

The Real area of contact and the effective frictional shear stress as functions of sliding velocity are shown in Figure 4-64 and Figure 4-65, respectively.

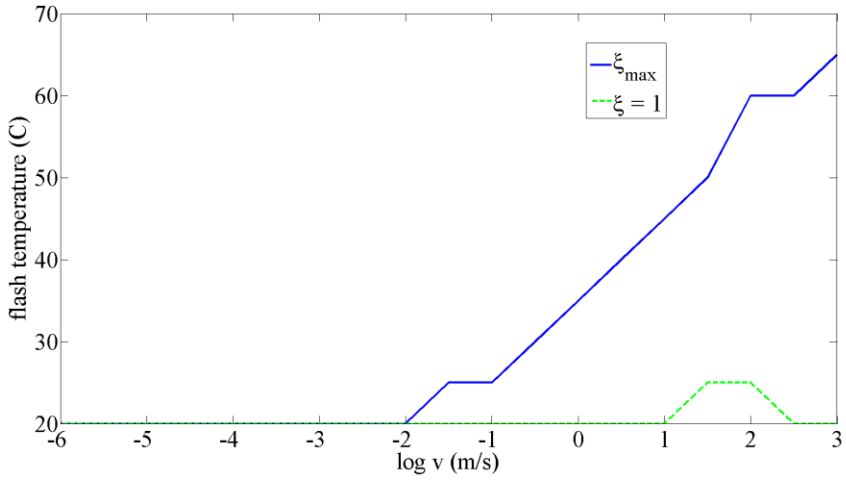

Figure 4-63. Footprint flash temperature at the surface of rubber sliding on sandpaper. The rubber background temperature is $T_0 = 20\,C$. The flash temperature at ζ_{max} is about $50\,C$ above the rubber background temperature, while at the nominal contact area ($\zeta = 1$), the change in temperature is insignificant.

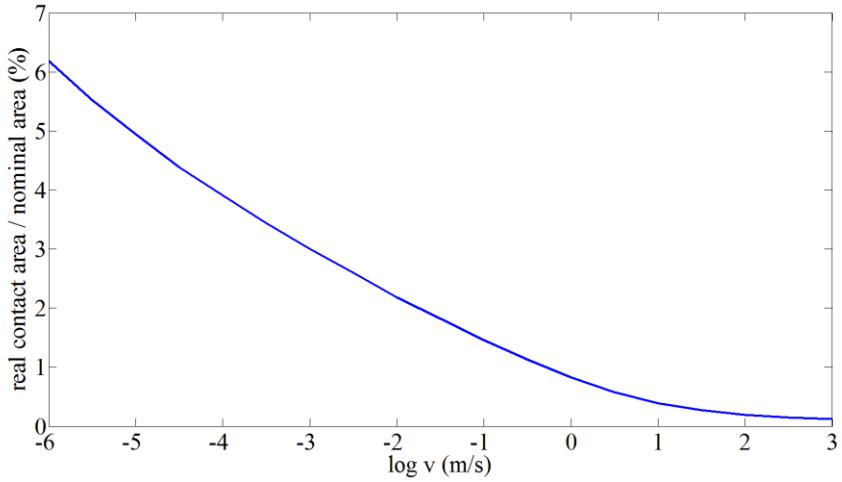

Figure 4-64. Real area of contact as a function of sliding velocity.

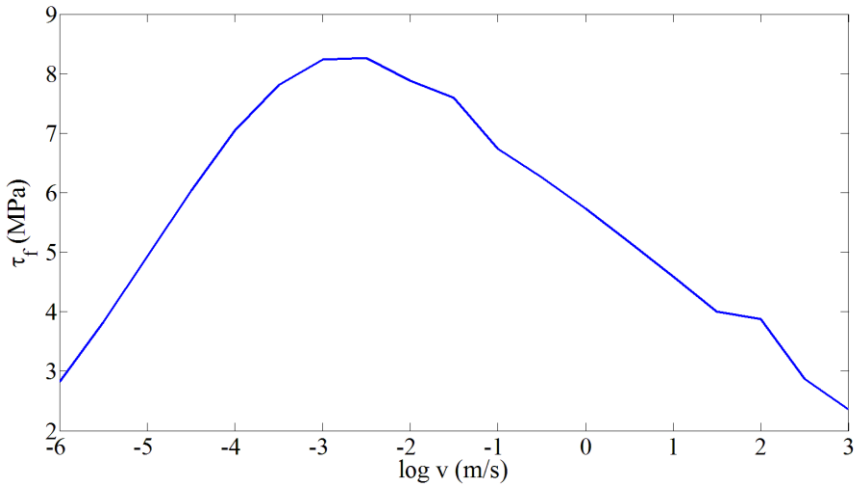

Figure 4-65. Effective frictional shear stress as a function of sliding velocity.

4.7 Dynamic Friction Tester

Since the PhD Preliminary Exam, several adjustments and fixes have been done on the friction tester. The preloading mechanism is modified to stabilize the normal load. Also, additional constraints are placed on

the preloading spring. Moreover, a module is added to the control program, and the wiring is modified, so that we can start/stop both servomotors simultaneously. Some other minor problems are resolved, as well.

We have been running tests using different tread compound samples on sandpaper, and collecting the data. Two types of curves have been of particular interest: friction vs. slip, and friction vs. speed. In Figure 4-66, the friction coefficient measured via the Dynamic Friction Tester is plotted with respect to longitudinal slip ratio for an all-season tread compound on 120-grit sandpaper. 0% and 100% slip correspond to free rolling and skidding, respectively. Friction reaches its peak at ~ 15-20% slip ratio. This is consistent with the data in the literature.

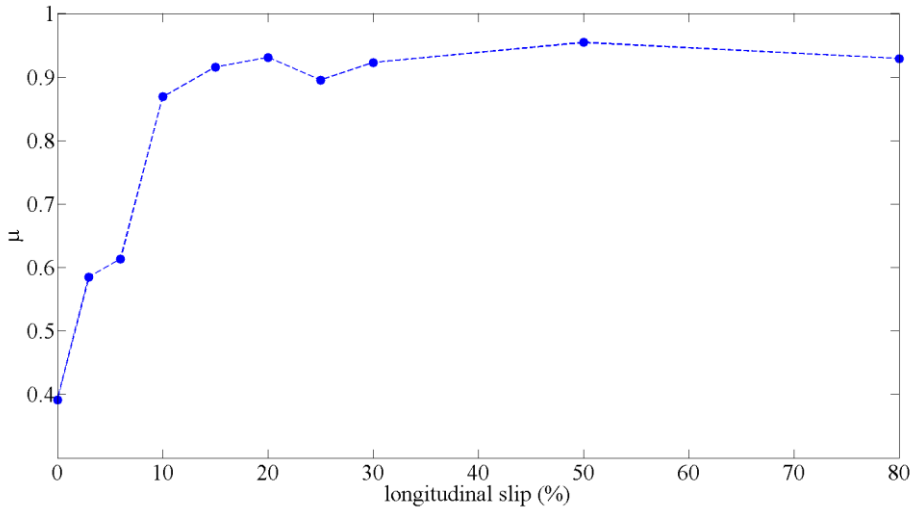

Figure 4-66. Measured (Dynamic Friction Tester) friction coefficient with respect to longitudinal slip ratio for an all-season tread compound on 120-grit sandpaper.

The tempertaure increase from the bulk of the rubber to the surface, right after a point on the surface exits the footprint, is only a few degrees. This cannot be representative of the flash temperature in the slip region of the contact patch, since temperature drops dramatically at the instant a point exits the patch.

In Figure 4-67, the friction coefficient measured via the Dynamic Friction Tester is shown as a function of sliding velocity for a summer tire tread compound on 120-grit sandpaper. For velocities greater than $\sim 10\ cm/s$, adhesion becomes less effective and therefore friction coefficient decreases with speed.

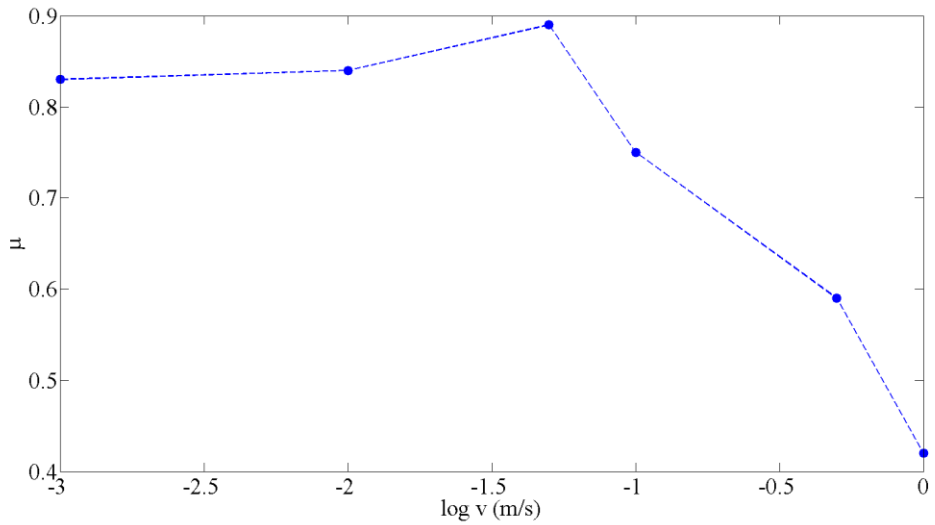

Figure 4-67. Measured (Dynamic Friction Tester) friction coefficient as a function of sliding velocity for a summer tire tread compound on 120-grit sandpaper.

5 Summary and Discussion

This research study was initiated with the goal of establishing reliable friction prediction methods based on tire tread properties and fractal properties of pavement texture. Several semi-empirical and physics-based friction prediction methods were studied, and some of them were implemented. The benefits that each method might offer under specific circumstances (e.g., wet friction, smooth surfaces, etc.) compared to other methods were evaluated. By developing several algorithms and models, measuring several rough surfaces, testing several tread compounds for their properties and running many different simulation

cases, a deep understanding of contact mechanics and the effect of the diverse factors that influence friction were gained.. The steps taken for predicting viscoelastic friction between any given tread compound and road, under different conditions, were:

- Measured the profile of road surfaces using the Nanovea JR25 optical profilometer. Compared to other measurement devices, this system is more robust, in terms of measurement of sharp angles and reflective surfaces. JR25 is also capable of measuring long profiles and large vertical distances, sufficient for a rigorous surface characterization that is essential for accurate friction prediction.
- Parameterized the profiles using only 1D measurements.
- Tested and characterized tire tread compounds, through our collaboration with Bridgestone.
- Developed a multiscale friction model, through a detailed analysis of the key variables that influence rubber-road friction. The model is all-inclusive and takes into account more factors, compared to the current approaches. This is accomplished by recognizing the strengths of each existing model and its advantages over the competitors, and integrating those into a new consolidated model.

Among the physics-based friction prediction models developed to date, an analytical incorporation of the effect of flash heating, as well as a semi-empirical formulation for the contribution from adhesion are exclusive to Persson friction theory. Also, the extension of the friction estimation formulation in the frame of a two-scaling-regimes approach is unique to Klüppel friction theory. Taking these effects into account has led to more accurate predictions [94] [77] [78] [97]. In the present study, to predict the friction coefficient between rubber and a rough surface more effectively, the aforementioned theories are used to develop an inclusive multiscale friction model, through a detailed analysis of the key variables of contact mechanics. The developed model takes into account more factors compared to the current approaches. This is accomplished by recognizing the strengths of each existing method and its advantages over the competitors, and integrating those into a new consolidated model.

Towards gaining a better insight into the rubber-road contact constituents that could be helpful for the multiscale model development, the real contact area for tire tread compounds, and the effect of using low strain and large strain viscoelastic master curves were studied. Also the sensitivity of friction to surface parameters, contributions of different length scales to friction, the mean penetration depth and the thickness of the excited layer of rubber, and the effect of the short-distance cut-off wavevector were investigated. The learning from these efforts can equip researchers with a better intuition when designing tribometers, deciding on a profile measurement device and adjusting the parameters, scheming friction and wear prediction experiments, as well as friction and wear estimation algorithms, and designing tread compounds.

A Digital Range Sensor System was used by Michigan Tech Transportation Institute to record the pavement profile heights with an accuracy of $45\ \mu m$, ensuring that the measured profile data incorporates both microtexture and macrotexture properties of the pavement surfaces. The FFT technique was used for the construction of the PSD plots. The surface roughness power spectrum includes valuable information concerning the characterization of road surfaces on different length scales. It is a suitable tool used in physics-based friction prediction methods. Perfect correlations were obtained between the tire-pavement friction and the mean square roughness (equal to the area under the PSD plots) of profiles of five road surfaces. Moreover, an angular parameter describing the road surface texture was presented. The angular parameter characterizes relative positions of profile peaks, i.e., the profile relief. The relevance of this parameter in relation to friction was demonstrated through correlation with Friction Number (FN) values. Fractal behavior in the road profiles under study was proven, by assessing the evolution of the energy in the signals with respect to scale. It was shown that Correlation Exponent and Regularization Dimension, which are global fractal quantities, are not able to classify a given class of profiles. Nonetheless, characterization using the pointwise Hölder exponent as a local fractal parameter was quite successful. The Hölder exponent of roughness has an influence on parameters of elastic contact, such as pressure,

displacement, and real contact area. Therefore, Hölder exponent could be used as an input data in contact mechanics modeling.

The hysteresis friction coefficient was calculated for an all-season passenger tire tread compound on the five road surfaces. The results presented the friction coefficient as a function of sliding velocity, with and without flash temperature. Good correlations were obtained between the friction measurement data and the simulation results. The correlation was improved, when flash temperature was taken into account. The computed local temperatures at the short-distance cut-off length scale were between $70 - 130$ ℃ above the rubber background temperature.

It has to be noted that no information regarding the tread compound properties of the genuine tire used on the friction trailer was available, and the data for a random tread compound was used. Using the properties of the actual compound from the measurements could possibly result in more accurate estimations and better correlations between theory and experiment.

A Dynamic Friction Test apparatus was designed and built. The system is composed of a fake road disk with an arbitrary surface, and the tire tread sample embedded in the measuring arm and in contact with the disk. The measuring arm holds the load cell that measures the vertical load and is constrained in longitudinal and axial directions by the longitudinal force measurement mechanism. This test rig is exceptional, as the road disk can be replaced easily. Furthermore, by controlling the speed of the rubber sample and the rotating disk at the same time, this equipment makes friction measurements at different slip ratios possible. 'Friction coefficient vs. slip ratio' data is particularly valuable for ABS-braking studies, where it is desired to maintain the slip ratio around the point where friction reaches its peak value.

To verify the friction prediction algorithm against indoor experiments, the friction coefficient is calculated and also measured (via the Dynamic Friction Tester) for a summer tire tread compound on sandpaper. The Nanovea JR25 was used to record the height profile of a sandpaper surface with an accuracy of $7\ \mu m$, ensuring the measured profile data incorporates both microtexture and macrotexture.

The fractal parameters used for friction estimation are extracted from the surface roughness power spectrum. The tire tread compound is characterized via Dynamic Mechanical Analysis. The simulation results presented the hysteresis and adhesive friction coefficients as a function of sliding velocity, with and without flash temperature, and with one and two scaling regimes. A fairly good correlation was obtained between the friction measurement data and the simulation results of the inclusive friction model. However, the correlation is still not perfect. This can be due to several factors. First, it has to be noted that friction is a very complex phenomenon and not all the mechanisms that might contribute to the friction between an elastomer and a rough surface could be identified and accounted for in the theory. Moreover, the friction tester's accuracy is not absolutely validated yet. Also, the formulation used for adhesion is not explicitly tuned for the specific tread compound used here. In addition, the concept of the minimum relevant wavelength [4] is not considered in this work. The minimum relevant wavelength can be estimated iteratively, within the two scaling regimes framework. It is a function of viscoelastic properties and roughness characteristics. A variable minimum relevant wavelength administers the diminishing contribution of microtexture as the sliding velocity increases. That could explain the decrease in the experimental friction coefficient at higher sliding velocities which is not observed in the simulation results (see Figure 4-62-b).

6 Future Work

The following recommendations are given for future work pertaining to this study:

- Bridgestone have provided us with samples of four tread compounds. We have currently the DMA results for only one of them. Tests need to be carried out for the remaining compounds. That data can be used to generate rubber viscoelastic master curves that are required for the estimation of friction between the respective compound and a rough substrate.
- For friction prediction, the effect of the minimum relevant wavelength can be studied in more detail. That should help enhance our friction estimations for a better correlation with the experimental results.
- By adding a climate control chamber to the Dynamic Friction Tester, we'll have the capability of simulating dry road conditions at specified temperatures and humidity levels, wet roads with certain water depth, and icy roads (see Figure 6-1). A standard Refrigeration and Humidity Control System can control the temperature between -20 to $150\,F$ (-29 to $65\,C$) and the humidity range between $10-98$ %.
- The effect of contact pressure on friction can be further studied. The physics-based contact theories suggest that in the typical pressure range in tire applications, the friction coefficient is independent of the contact pressure. However, some experiments in the literature have shown that the coefficient of friction changes significantly with pressure. We have not been able to replicate that in our simulations yet.
- In the literature, for wear prediction, either a constant friction coefficient or empirical friction models (with known deficiencies) are used with tire models. Also, in the works up to date, the road surface profile is usually not taken into account. The proficient multi-scale rubber friction model that is developed in the current project will be used in a new project that is accepted by CenTiRe's Industry Advisory Board, where the objective is to estimate tire wear analytically. Wear models, such

as Archard, Reye and Holm, can be used to describe sliding wear and are based on the theory of asperity contact. These models are used to calculate the volume of the removed debris due to wear, using the work done by friction forces. Other models, such as Bryant, relate friction and wear rate through laws of thermodynamics. These wear laws will be used in combination with the physics-based friction model, and also a tire model (rigid ring model + 2D brush model) to add the influence from vehicle dynamics and ABS braking to tire wear.

- Some length scales might be more effective than others. One potential future plan is to use the rubber friction tester and do friction measurements for dominant wavelengths that are obtained via spectral analysis and fabricated onto the road disk. An algorithm can be developed to investigate the contributions of macro- and micro-texture constituents to rubber-road friction. This algorithm can determine which scales are dominant in the buildup of friction. The correlation between the theoretical and the experimental results can be assessed.

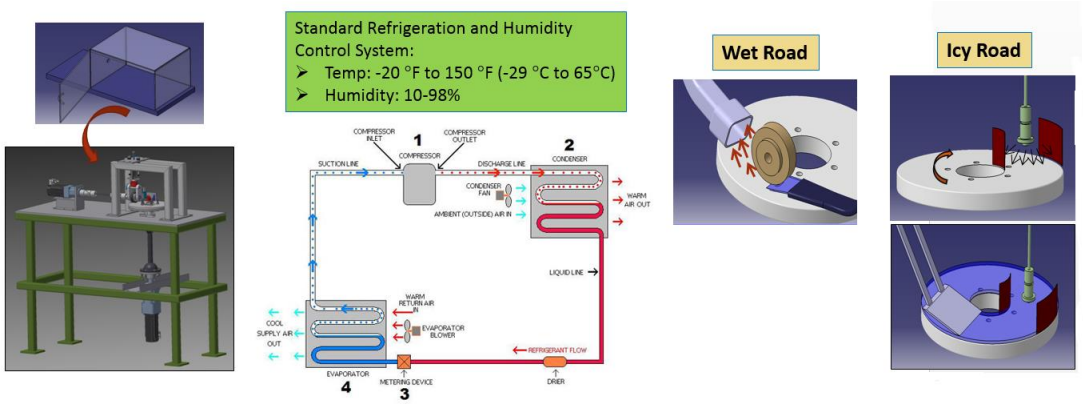

Figure 6-1. Climate control chamber with a refrigeration and humidity control system for the Dynamic Friction Tester.

References

1. Radó, Z., *A study of road surface texture and its relationship to friction*. 1994, Ph.D. Thesis, Pennsylvania State University.

2. Heinrich, G., *Hysteresis friction of sliding rubbers on rough and fractal surfaces.* Rubber chemistry and technology, 1997. 70(1): p. 1-14.

3. Guglielmi, M. and J. Levy-Vehel. *Analysis and simulation of road profile by means of fractal model*. in *Conference on Advances in Vehicle Control and Safety (AVCS 98), Amiens*. 1998.

4. Klüppel, M. and G. Heinrich, *Rubber friction on self-affine road tracks.* Rubber chemistry and technology, 2000. 73(4): p. 578-606.

5. Legrand, P., *Débruitage et interpolation par analyse de la régularité Hölderienne. Application à la modélisation du frottement pneumatique-chaussée*. 2004, Ecole centrale de nantes-ECN.

6. Van den Oetelaar, R. and C. Flipse, *Atomic-scale friction on diamond (111) studied by ultra-high vacuum atomic force microscopy.* Surface science, 1997. 384(1): p. L828-L835.

7. Moore, D., *The friction and lubrication of elastomers, 1972*. Pergamon Press, Oxford.

8. Persson, B.N., *On the theory of rubber friction.* Surface Science, 1998. 401(3): p. 445-454.

9. Persson, B., *Adhesion between an elastic body and a randomly rough hard surface.* The European Physical Journal E: Soft Matter and Biological Physics, 2002. 8(4): p. 385-401.

10. Galliano, A., S. Bistac, and J. Schultz, *Adhesion and friction of PDMS networks: molecular weight effects.* Journal of colloid and interface science, 2003. 265(2): p. 372-379.

11. Persson, B.N., *Theory of rubber friction and contact mechanics.* The Journal of Chemical Physics, 2001. 115(8): p. 3840-3861.

12. Persson, B.N. and A. Volokitin, *Theory of rubber friction: Nonstationary sliding.* Physical Review B, 2002. 65(13): p. 134106.

13. Meyer, W.E. and J.D. Walter, *Frictional Interaction of Tire and Pavement*. Vol. 793. 1983: ASTM International.

14. Persson, B., et al., *Sealing is at the origin of rubber slipping on wet roads.* Nature materials, 2004. 3(12): p. 882-885.

15. Do, M.-T., et al., *Modeling of the connection road surface microtexture/water depth/friction.* Wear, 2013. 302(1): p. 1426-1435.

16. Mandelbrot, B.B., *The fractal geometry of nature*. Vol. 173. 1983: Macmillan.

17. Mandelbrot, B., *Fractals and chaos: the Mandelbrot set and beyond*. Vol. 3. 2004: Springer.

18. Kenneth, F., *Fractal geometry*. UK: WILEY, 2003. 337.

19. Sagan, H., *Space-filling curves*. Vol. 18. 1994: Springer-Verlag New York.

20. Vicsek, T., *Fractal growth phenomena*. Vol. 4. 1989: World Scientific.

21. Mandelbrot, B.B., *How long is the coast of Britain.* Science, 1967. 156(3775): p. 636-638.

22. Iannaccone, P.M. and M. Khokha, *Fractal geometry in biological systems: an analytical approach*. 1996: CRC Press.

23. Abry, P., P. Goncalves, and J.L. Véhel, *Scaling, fractals and wavelets*. 2013: John Wiley & Sons.

24. Falconer, K.J. *The Hausdorff dimension of self-affine fractals*. in *Math. Proc. Camb. Phil. Soc*. 1988. Cambridge Univ Press.

25. Roueff, F. and J.L. Véhel, *A regularization approach to fractional dimension estimation.* Proc. of Fractals, 1998. 98.

26. Falconer, K.J. and J.L. Véhel, *Horizons of fractional Brownian surfaces.* Proceedings of the Royal Society of London. Series A: Mathematical, Physical and Engineering Sciences, 2000. 456(2001): p. 2153-2178.

27. Li, J. and F. Nekka, *The Hausdorff measure functions: A new way to characterize fractal sets.* Pattern recognition letters, 2003. 24(15): p. 2723-2730.

28. Feng, Z., M.J. Zuo, and F. Chu, *Application of regularization dimension to gear damage assessment.* Mechanical Systems and Signal Processing, 2010. 24(4): p. 1081-1098.

29. Doble, M. and S.K. Narayan, *Mathematical analysis of EEG of patients with non-fatal nonspecific diffuse encephalitis.* International Journal of Biological and Medical Sciences, 2008. 3(4).

30. Torrecilla, J.S., et al., *Chaotic parameters and their role in quantifying noise in the output signals from UV, TGA and DSC apparatus.* Talanta, 2009. 79(3): p. 665-668.

31. Do, M.-T., H. Zahouani, and R. Vargiolu, *Angular parameter for characterizing road surface microtexture.* Transportation Research Record: Journal of the Transportation Research Board, 2000. 1723(1): p. 66-72.

32. Beran, J., *Statistics for long-memory processes*. Vol. 61. 1994: CRC Press.

33. Mezghani, S., et al., *The scale effect of roughness in contact problems.* High Performance Structures and Materials III Transaction, 2006: p. 369-378.

34. Más, J., et al., *Dynamic mechanical properties of polycarbonate and acrylonitrile–butadiene–styrene copolymer blends.* Journal of applied polymer science, 2002. 83(7): p. 1507-1516.

35. Young, R.J. and P.A. Lovell, *Introduction to polymers*. Vol. 2. 1991: Chapman & Hall London.

36. Menard, K.P., *Dynamic mechanical analysis: a practical introduction*. 2008: CRC press.

37. Erukulla, S., *Refining a Laboratory Procedure to Characterize Change in Hot-Mix Asphalt Surface Friction*. 2010, Auburn University.

38. Saito, K., et al., *Development of portable tester for measuring skid resistance and its speed dependency on pavement surfaces.* Transportation Research Record: Journal of the Transportation Research Board, 1996. 1536(1): p. 45-51.

39. Materials, A.S.f.T.a., *Measuring Surface Friction Properties Using the British Pendulum Tester, ASTM Standard Test Method E- 303-93.* Book of ASTM Standards, 2003. 04.03(Philadelphia, PA).

40. Bredell, L., L. Johnson Jr, and D. Kuhlmann-Wilsdorf, *Teaming measurements of the coefficient of friction and of contact resistance as a tool for the investigation of sliding interfaces.* Wear, 1987. 120(2): p. 161-173.

41. Materials, A.S.f.T.a., *Measuring Pavement Surface Frictional Properties Using the Dynamic Friction Tester*, in *ASTM Standard Test Method E 1911-98*. 2002, Book of ASTM Standards: Volume 04.03, Philadelphia, PA.

42. Vollor, T.W. and D.I. Hanson, *Development of Laboratory Procedure for Measuring Friction of HMA Mixtures–Phase I.* NCAT Report 06, 2006. 6.

43. Berres, R. *High-speed linear friction testing*. in *Tire Technology International*. 2011.

44. Berritta, R., et al. *Identification of motorcycle tire properties by means of a testing machine*. in *Proc. 2002 SEM Annual Conference and Exposition on Experimental and Applied Mechanics*. 2002.

45. Dewey, G.R., Robords, A. C., Armour, B. T., and Muethel, R. *Aggregate Wear and Pavement Friction*. in *Transportation Research Board, Annual Meeting CD-ROM*. 2001.

46. Materials, A.S.f.T.a., *Standard Practice for Accelerated Polishing of Aggregates or Pavement Surfaces Using a Small-Wheel, Circular Track Polishing Machine*, in *ASTM Standard Test Method E 660-90, Book of ASTM Standards, Volume 04.03*. 2005: Philadelphia, PA.

47. Nitta, N., K. Saito, and S. Isozaki, *Evaluating the polishing properties of aggregates and bituminous pavement surfaces by means of the Penn State Reciprocating Polishing Machine.* Surface Characteristics of Roadways: International Research and Technologies, ASTM STP, 1990. 1031: p. 113-126.

48. Materials, A.S.f.T.a., *Skid Resistant of Paved Surfaces Using a Full-Scale Tire*, in *ASTM Standard Test Method E 274-97, Book of ASTM Standards, Volume 04.03*. 2005: Philadelphia, PA.

49. Henry, J.J., *Evaluation of pavement friction characteristics*. Vol. 291. 2000: Transportation Research Board.

50. Davis, R.M., *Comparison of surface characteristics of hot-mix asphalt pavement surfaces at the Virginia Smart Road*. 2001, Virginia Polytechnic Institute and State University.

51. Li, S., et al., *Identifying friction variations with the standard smooth tire for network pavement inventory friction testing.* Transportation Research Record: Journal of the Transportation Research Board, 2005. 1905(1): p. 157-165.

52. Materials, A.S.f.T.a., *Standard Specification for Standard Rib Tire for Pavement Skid-Resistance Tests*, in *ASTM Standard Test Method E 501- 94, Book of ASTM Standards, Volume 04.03*. 2005: Philadelphia, PA.

53. Materials, A.S.f.T.a., *Standard Specification for Standard Smooth Tire for Pavement Skid-Resistance Tests,* in *ASTM Standard Test Method E 524-88, Book of ASTM Standards, Volume 04.03*. 2005: Philadelphia, PA.

54. Rajapakshe, M.P.N., *Physically Meaningful Harmonization of Tire/Pavement Friction Measurement Devices*. 2011, University of South Florida.

55. Do, N.B., *Modeling of frictional contact conditions in structures.* 2005.

56. Grosch, K., *The relation between the friction and visco-elastic properties of rubber.* Proceedings of the Royal Society of London. Series A. Mathematical and Physical Sciences, 1963. 274(1356): p. 21-39.

57. Hassner, M. and J. Sklansky, *The use of Markov random fields as models of texture.* Computer Graphics and Image Processing, 1980. 12(4): p. 357-370.

58. Majumdar, A., *Fractal surfaces and their applications to surface phenomena*. 1989, University of California, Berkeley.

59. Johnson, K., *Contact mechanics, 1985.* Cam-bridge University Press, Cambridge, 1974.

60. Greenwood, J. and J. Williamson, *Contact of nominally flat surfaces.* Proceedings of the Royal Society of London. Series A. Mathematical and Physical Sciences, 1966. 295(1442): p. 300-319.

61. Mikić, B., *Thermal contact conductance; theoretical considerations.* International Journal of Heat and Mass Transfer, 1974. 17(2): p. 205-214.

62. Do, M.T. and H. Zahouani, *Frottement pneumatique/chaussée–Influence de la microtexture des surfaces de chaussée.* JFT (Journées Internationales Francophones de Tribologie), 2001.

63. Taneerananon, P. and W. Yandell, *Microtexture roughness effect on predicted road-tyre friction in wet conditions.* Wear, 1981. 69(3): p. 321-337.

64. Greenwood, J. and D. Tabor, *The friction of hard sliders on lubricated rubber: the importance of deformation losses.* Proceedings of the Physical Society, 1958. 71(6): p. 989.

65. Darafon, A., A. Warkentin, and R. Bauer, *Characterization of grinding wheel topography using a white chromatic sensor*. International Journal of Machine Tools and Manufacture, 2013. 70: p. 22-31.

66. Leach, R., *Optical measurement of surface topography*. 2011: Springer.

67. Leach, R., et al., *Measurement Good Practice Guide No. 108 "Guide to the Measurement of Smooth Surface Topography using Coherence Scanning Interferometry".* Teddington, UK, 2008.

68. Petzing, J.N., J.M. Coupland, and R.K. Leach, *The measurement of rough surface topography using coherence scanning interferometry.* 2010.

69. (BSi), B.S., *Characterization of Pavement Texture by Use of Surface Profiles, Part 4: Spectral Analysis of Surface Profiles*. 2008, DD ISO/TS.

70. Grandke, T., *Interpolation algorithms for discrete Fourier transforms of weighted signals.* Instrumentation and Measurement, IEEE Transactions on, 1983. 32(2): p. 350-355.

71. Persson, B., et al., *On the nature of surface roughness with application to contact mechanics, sealing, rubber friction and adhesion.* Journal of Physics: Condensed Matter, 2005. 17(1): p. R1.

72. Heath, A., *Application of the isotropic road roughness assumption.* Journal of sound and vibration, 1987. 115(1): p. 131-144.

73. Scaraggi, M., C. Putignano, and G. Carbone, *Elastic contact of rough surfaces: A simple criterion to make 2D isotropic roughness equivalent to 1D one.* Wear, 2013. 297(1): p. 811-817.

74. Carbone, G., et al., *Contact mechanics and rubber friction for randomly rough surfaces with anisotropic statistical properties.* The European Physical Journal E: Soft Matter and Biological Physics, 2009. 29(3): p. 275-284.

75. Vicharelli, P.A. and W.P. Lapatovich, *Iterative method for computing the inverse Abel transform.* Applied physics letters, 1987. 50(10): p. 557-559.

76. Bracewell, R.N. and R. Bracewell, *The Fourier transform and its applications*. Vol. 31999. 1986: McGraw-Hill New York.

77. Persson, B.N., *Rubber friction: role of the flash temperature.* Journal of Physics: Condensed Matter, 2006. 18(32): p. 7789.

78. Lorenz, B., et al., *Rubber friction on road surfaces: Experiment and theory for low sliding speeds.* The Journal of chemical physics, 2015. 142(19): p. 194701.

79. Bunde, A. and S. Havlin, *Fractals and disordered systems*. 1991: Springer-Verlag New York, Inc.

80. Bunde, A. and S. Havlin, *Fractals in science*. 1995: Springer-Verlag New York, Inc.

81. Le Gal, A., X. Yang, and M. Klüppel, *Evaluation of sliding friction and contact mechanics of elastomers based on dynamic-mechanical analysis.* The Journal of chemical physics, 2005. 123(1): p. 014704.

82. Pathria, R.K., *Statistical mechanics.* 1996.

83. Huang, C. and S. Mei, *Investigation of Road Surface Texture Wavelengths.*

84. Elson, J.M. and J.M. Bennett, *Calculation of the power spectral density from surface profile data.* Applied Optics, 1995. 34(1): p. 201-208.

85. Himeno, K., et al. *Skid resistance of asphalt pavement surfaces related to their microtexture*. in *International symposium on pavement surface characteristics of roads and airfields*. 2000.

86. Gunaratne, M., et al., *Correlation of tire wear and friction to texture of concrete pavements.* Journal of materials in civil engineering, 2000. 12(1): p. 46-54.

87. Khan, G.S., et al., *Characterization of nanoscale roughness in single point diamond turned optical surfaces using power spectral density analysis.* Indian Journal of Engineering and Materials Science, 2004. 11(1): p. 25-30.

88. Yandell, W., *A new theory of hysteretic sliding friction.* Wear, 1971. 17(4): p. 229-244.

89. Christensen, R., *Theory of viscoelasticity: an introduction*. 1982: Elsevier.

90. Ferry, J.D., *Viscoelastic properties of polymers*. 1980: John Wiley & Sons.

91. van Gurp, M. and J. Palmen, *Time-temperature superposition for polymeric blends.* Rheol. Bull, 1998. 67(1): p. 5-8.

92. Takeuchi, H. and R.J. Roe, *Molecular dynamics simulation of local chain motion in bulk amorphous polymers. II. Dynamics at glass transition.* The Journal of chemical physics, 1991. 94(11): p. 7458-7465.

93. Mark, J.E., B. Erman, and M. Roland, *The science and technology of rubber*. 2013: Academic Press.

94. Le Gal, A. and M. Klüppel, *Investigation and modelling of rubber stationary friction on rough surfaces.* Journal of Physics: Condensed Matter, 2008. 20(1): p. 015007.

95. Handzel-Powierza, Z., T. Klimczak, and A. Polijaniuk, *On the experimental verification of the Greenwood-Williamson model for the contact of rough surfaces.* Wear, 1992. 154(1): p. 115-124.

96. Hertz, H., *Miscellaneous papers*. 1896: Macmillan.

97. Le Gal, A., et al., *Modelling of sliding friction for carbon black and silica filled elastomers on road tracks.* Wear, 2008. 264(7): p. 606-615.

98. Westermann, S., et al., *Experimental investigations into the predictive capabilities of current physical rubber friction theories.* Kautschuk Gummi Kunststoffe, 2004. 57(12): p. 645-650.

99. Lorenz, B., et al., *Rubber friction for tire tread compound on road surfaces.* Journal of Physics: Condensed Matter, 2013. 25(9): p. 095007.

100. Krick, B.A., et al., *Optical in situ micro tribometer for analysis of real contact area for contact mechanics, adhesion, and sliding experiments.* Tribology Letters, 2012. 45(1): p. 185-194.

101. Persson, B. and A. Volokitin, *Rubber friction on smooth surfaces.* The European Physical Journal E, 2006. 21(1): p. 69-80.

102. Schallamach, A., *A theory of dynamic rubber friction.* Wear, 1963. 6(5): p. 375-382.

103. Lorenz, B., W. Pyckhout-Hintzen, and B. Persson, *Master curve of viscoelastic solid: using causality to determine the optimal shifting procedure, and to test the accuracy of measured data.* Polymer, 2014. 55(2): p. 565-571.

104. Naya, S., et al., *New method for estimating shift factors in time–temperature superposition models.* Journal of thermal analysis and calorimetry, 2013. 113(2): p. 453-460.

105. Wei, L., T. Fwa, and Z. Zhe. *Pavement roughness analysis using wavelet theory*. in *In Proceedings from the 6th International Conference on Managing Pavements. Queensland, Australia*. 2002.

106. Legrand, P., J.L. Véhel, and D.M. Tan. *Fractal properties and characterization of road profiles*. in *FRACTAL04, Complexity and Fractals in Nature, 8th International Multidisciplinary Conference*. 2004.

107. Fortunato, G., et al., *General theory of frictional heating with application to rubber friction.* Journal of Physics: Condensed Matter, 2015. 27(17): p. 175008.